Bayesian Damage Detection for Vibration Based Bridge Health Monitoring

Yoshinao GOI

2018

Abstract

Nowadays, maintaining and improving bridge structures have become keen technical issues, since any light structural damage or defects in a bridge can potentially result in fatal accidents. Preventive maintenance is also essential to increase the life spans of the bridges and to avoid long-term traffic interruption. Vibration based structural health monitoring provides a research field for nondestructive evaluation based on physical measurements and computer analyses to complement existing visual inspection methods. Especially for short and middle span bridges, the traffic loading excites the bridges continuously, and thus vibration monitoring is available without interrupting the traffic. Most of the existing studies examined modal properties such as natural frequencies, damping ratios and mode shapes to assess the bridge condition. Several other studies examined damage indicators that are promptly generated from the measured data without identifying the modal properties. Although great number of studies showed validity of vibration based structural health monitoring for the bridges, the following two obstructions remain to be solved: Firstly, precise modal identification requires experience on data processing, and thus more concise decision rule is required to realize screening method for the numerous existing bridges. Secondly, the existing damage indicators dismiss most of information included in the original data to generate simple indicators, and thus they are less reliable than the modal properties.

Aiming at efficient inspection based on the vibration monitoring, this thesis proposes a damage indicator by unsupervised machine learning. That is, the healthy condition of a bridge is learned at first from the vibration actually monitored on the healthy bridge. Bayesian statistics enables the machine learning with a suitable stochastic model to represent random bridge vibration. The stochastic model is formulated as a parametric model based on the dynamical equation of motion of the bridges. The parametric models are investigated through the operational modal analysis theory. To quantify the uncertainty involved in the decision-making for bridge management, the validity of the Bayesian statics for modal analysis is examined. To distinguish damage from huge amount of data, damage sensitive features are investigated based on the modal analysis theory. The Bayesian inference and the Bayesian hypothesis testing provides reliable and concise damage indicators to detect changes in modal properties. Each step of the above investigation is verified by considering a field experiment on an actual steel truss bridge whose truss members were artificially severed. The validity of the proposed damage indicator is also examined through one-year monitoring and damage test on a steel plate girder bridge.

Acknowledgements

The present research was performed through PhD educational course at the International Management of Civil Infrastructure Laboratory in the Department of Civil and Earth resources Engineering at Kyoto University. I have been fortunate to have the great support and attention from teachers, friends and family. It is a pleasure to express my gratitude to all these people.

Primarily, I would like to express my profound gratitude and appreciation to my supervisor, Professor Chul-Woo Kim, for his invaluable advice and encouragement throughout my PhD study. His instruction based on deep insight widely opened the view of this research field. Without his continuous and generous support, this research could not have been possible.

I would like to show my deep appreciation to Professor Kunitomo Sugiura, for his great support continuing from my master course. His thoughtful guidance and suggestion always let me remember what engineers should be. I admire inexhaustible energy driving his enthusiasm.

I also would like to show my appreciation to Professor Tomomi Yagi for his exertion as the member of dissertation committee. His considerate advices vigorously encouraged me. I also would like to express my gratitude to his critical questions.

I am deeply indebted to Professor Tomoaki Utsunomiya in Kyushu University, for the first instruction to be an engineer. His unceasing guidance over two years cultivated my basic attitude toward engineering researches.

I would like to show my gratitude to Dr. Kai-Chun Chang, lecturer in Kyoto University, for his valuable suggestion and advice. I also appreciate his continuous effort at facilitating the laboratory management to maintain favorable environment.

I also would like to show my gratitude to Gen Hayashi, PhD candidates in Kyoto University in the same research field. Thanks to his cooperation, the one-year monitoring was successfully operated. I owe him to his abundant experience especially in the field experiments.

I would like to expand my appreciation to my laboratory members. I gratefully thanks to Ms. Kazuko Oobayashi, secretary of the laboratory. She has been so kind in assisting daily matters in the laboratory. I would like to show my gratitude to Mr. Soutaro Kitauchi, Tomoaki Morita, Shinichi Inoue, Wang Zhiran, Daigou Kawabe, former students from my research group. They contributed to investigate feasibility of traffic-induced vibration based bridge health monitoring. Mr. Takuya Mimasu and Xinda Ma, master course students, have supported my study with stimulating discussions.

The present research is partly sponsored by a Japanese Society for Promotion of Science (JSPS) Grant-in-Aid for Scientific Research (B) under Project No. 16H04398 and for JSPS fellows project under Project No. 17J09033. I would like to express my gratitude to their financial support.

Lastly, I would like to express gratitude to my family, Ryoichi, Keiko, my brother Kento, my sister Rina, and my dear dog Meloo, for their emotional encouragement at any time. Their kind supports reassuringly made me manage to finish this tough work.

Contents

CHAPTER 1 INTRODUCTION 1

1.1 Backgrounds 1

1.1.1 Motivation 1

1.1.2 Overview of existing studies 2

1.2 Objectives 3

1.3 Outline of the Thesis 5

1.4 Target Bridge 6

CHAPTER 2 MATHEMATICAL DESCRIPTION 11

2.1 Introduction 11

2.2 Probability Theory 12

2.2.1 Basic properties 12

2.2.2 Frequentist and Bayesian statistics for modal analysis 15

2.2.3 Linear regressive models 17

2.3 Models of Vibrating Structures 21

2.3.1 General description 21

2.3.2 State space model 23

2.3.3 Autoregressive models 25

CHAPTER 3 OPERATIONAL MODAL ANALYSIS 28

3.1 Introduction 28

3.2 Methodologies 29

3.2.1 Yule-Walker method 29

3.2.2 Stochastic subspace identification 31

3.2.3 Bayesian operational modal analysis 33

3.3 Case Studies 36

3.3.1 Model selection 36

3.3.2 Feature extraction 39

3.4 Summary 44

CHAPTER 4 MODAL ANALYSIS OF A CABLE-STAYED BRIDGE 46

4.1 Introduction 46

4.2 Target Bridge and Benchmark Data 46

4.3 Preliminary Analysis 48

4.3.1 Stochastic subspace identification 48

4.3.2 Bayesian operational modal analysis 49

4.4 Identified Modal Properties 52

4.5 Investigation of the Uncertainty 54

4.6 Summary 58

CHAPTER 5 DAMAGE SENSITIVE FEATURES 60

5.1 Introduction 60

5.2 Damage Indicator from Multivariate Linear System 61

5.2.1 Damage detection flow 61

5.2.2 Feature extraction 62

5.2.3 Damage indicator and hypothesis testing 64

5.3 Case Studies 66

5.3.1 Preliminary investigation 66

5.3.2 Hypothesis testing 67

5.3.3 Comparison with existing studies 69

5.4 Summary 71

CHAPTER 6 BAYES FACTORS 72

6.1 Introduction 72

6.2 Methodology 73

6.2.1 Bayesian inference 73

6.2.2 Hypothesis testing 75

6.2.3 Computational strategies 79
6.3 Relationship with Existing Methodologies 81
6.4 Case Studies 82
6.4.1 Preliminary investigation 83
6.4.2 Damage detection 86
6.4.3 Comparison to the previous damage indicator 92
6.5 Summary 93
CHAPTER 7 APPLICATION TO A STEEL PLATE GIRDER BRIDGE 95
7.1 Introduction 95
7.2 Target Bridge and Finite Element Model 96
7.2.1 Target bridge 96
7.2.2 Finite element model 98
7.3 One Year Monitoring 100
7.3.1 Vibration monitoring 100
7.3.2 Seasonal fluctuation of boundary condition 105
7.4 Damage Experiment 107
7.4.1 Bayes factors 107
7.4.2 Natural frequencies 108
7.5 Summary 110
CHAPTER 8 CONCLUSION AND OPEN PROBLEMS 111
8.1 Conclusions 111
8.2 Open Problems 114
REFERENCES 116
APPENDIX 123

List of Figures

Figure 1.1 Photographs of the ruptured member on Kisogawa Bridge. 1

Figure 1.2 Organization of the thesis. 5

Figure 1.3 The target bridge: a) photograph; b) approximate size; c) sensor deployment. 7

Figure 1.4 Artificial damages: a) Photographs; b) Schematic diagram 8

Figure 1.5 Examples of acquired time series at A3 sensor and their PSD curves: a) For INT40; b) For DMG1; c) For DMG2 9

Figure 3.1 Information criteria for the AR models with respect to the model orders: a) for WV data; b) for FV data 37

Figure 3.2 Information criteria for the ARMA models with respect to the model orders: a) for WV data; b) for FV data. 38

Figure 3.3 Exsample of stabilization diagram for the AR models: a) For WV data; b) For FV data 41

Figure 3.4 Stabilization diagram for the SSI with respect to the singular value orders: a) For WV data; b) For FV data 42

Figure 3.5 Mode shapes identified from SSI: a) 1st; b) 2nd; c) 3rd; d) 4th; e) 5th 43

Figure 4.1 Deployment of Accelerometers and Anemometers on Ting Kau Bridge. 47

Figure 4.2 Geometry configuration of accelerometers on the bridge deck. 47

Figure 4.3 AIC with respect to size of the block Hankel matrix. 49

Figure 4.4 Averaged SVS and the frequency bands for identification 49

Figure 4.5 Example of identified mode shapes under weak wind (Sample 1) 52

Figure 4.6 Example of identified mode shapes under typhoon (Sample7) 53

Figure 4.7 Stabilization diagrams under the weak wind conditions: a) Sample 1; b) Sample 2; c) Sample 3; d) Sample 4; e) Sample 5; f) Sample 6. 54

Figure 4.8 Stabilization diagrams under the typhoon conditions: a) Sample 7; b) Sample 8; c) Sample 9; d) Sample 10 55

Figure 4.9 Mean value of the lateral acceleration PSD 55

Figure 4.10 Cumulative contribution ratios of singular values calculated in SSI. 56

Figure 4.11 Coefficient of variance (%): a) For natural frequencies; b) For damping ratios. 57

Figure 4.12 Signal to noise ratios of the modal responses. 57

Figure 5.1 Flow of damage detection utilizing the proposed damage indicator 61

Figure 5.2 Sample means of MD with respect to AR orders: a) For WV data; b) For FV data. 67

Figure 5.3 The T 2 statistics: a) From WV data; b) From FV data. 68

Figure 5.4 The obtained principal components: a) From WV data; b) From FV data. 68

Figure 5.5 Mean values of MDs for WV data: a) INT, DMG1, and DMG2; b) RCV and DMG3.................. 70

Figure 5.6 Mean values of MDs for FV data: a) INT, DMG1, and DMG2; b) RCV and DMG3. 70

Figure 6.1 Flow of the Bayesian damage detection 73

Figure 6.2 The Schwarz criteria with respect to the AR orders. 83

Figure 6.3 Stabilization diagrams with respect to the *q* order: a) for low order AR model (*p*=20); b) for higher order AR model (*p*=150). 85

Figure 6.4 Global Bayes factors for BF ver.1: a) for Case1; b) for Case 2 87

Figure 6.5 Global Bayes factors for BF ver.2: a) for Case1; b) for Case 2 88

Figure 6.6 Local Bayes factors for BF ver.1 (P=20): a) for Case1; b) for Case 2... 90

Figure 6.7 Local Bayes factors for BF ver.2 (P=150): a) for Case1; b) for Case 2... 91

Figure 6.8 Previously investigated damage indicators: a) for Case1; b) for Case2. 92

Figure 7.1 The target bridge: a) photograph; b) sensor deployment. 96

Figure 7.2 Photographs of the supports: a) on Ab1 abutment; b) on Ab2 abutment. 96

Figure 7.3 Artificial damages on the G1 girder near the base plate of Ab1: a) Schematic diagram; b) photographs. 97

Figure 7.4 FE model of the bridge and pseudo cracks on plate girder. 98

Figure 7.5 Modal deformations identified in FE model for the INT scenario: a) 1st bending (3.08 Hz); b) 1st torsional (5.08 Hz); c) 2nd bending (9.36 Hz); d) 2nd torsional (10.84 Hz); e) Asymmetric bending (15.49 Hz); f) 3rd bending (21.57 Hz). 99

Figure 7.6 Time series before pre-processing: a) Averaged strain; b) Acceleration..................................... 101

Figure 7.7 Example of time series of acceleration extracted from long-term monitoring data..................... 101

Figure 7.8 The Schwarz criteria with respect to the AR orders. 102

Figure 7.9 Stabilization diagram for the feature extraction process. 103

Figure 7.10 Mode shapes relevant to the damage sensitive feature: 103

Figure 7.11 Observed global Bayes factors measured in one day: a) On September; b) On January. 104

Figure 7.12 Global Bayes factors monitored through a year (Sep 2016- Aug 2017). 104

Figure 7.13 Local Bayes factors monitored before the traffic limitation (Sep 2016-Mar 2017)................... 105

Figure 7.14 Deformation of the supports: a) Time series (Sep 2016-Aug 2017); b) Scatter diagram with respect to the temperature. 106

Figure 7.15 Bayes factors for the damage experiment: a) Global Bayes factor; b) Local Bayes factor......... 107

Figure 7.16 Histograms of the identified natural frequencies of the bending modes (Hz). 109

List of Tables

Table 1.1 Scenarios considered in the field experiment. 8

Table 3.1 Numbers of the correctly extracted poles. 43

Table 4.1 Benchmark data. 48

Table 4.2 Identified natural frequencies (Hz) and coefficient of variance (%) 50

Table 4.3 Identified damping ratios (%) and coefficient of variance (%) 51

Table 5.1 Sensor groups to calculate MD. 69

Table 6.1 Cases considered for the damage detection. 87

Table 6.2 The ratios of correct answers for the global Bayes factors (%). 89

Table 7.1 Natural frequencies identified in the FE model (Hz). 100

List of Notations and Abbreviations

$\lVert\cdot\rVert$	Euclidean norm of a vector
$\lvert\cdot\rvert$	Determinant of a matrix
$(\cdot)^{\dagger}$	Moor-Penrose pseudo-inverse of a matrix
$\mathbf{0}$	Zero vector
$\boldsymbol{O}$	Zero matrix
$\Gamma(\cdot)$	Gamma function
$\mathrm{abs}(\cdot)$	Absolute value
$\mathrm{Cov}[\cdot]$	Covariance matrix
$\mathcal{D}$	Observed dataset
$\mathrm{diag}[\cdot]$	Diagonal matrix
$E(\cdot)$	Sum-of-squares error function for linear regressive models
$\mathbb{E}[\cdot]$	Expectation
$\exp[\cdot]$	Natural exponential function
$Gam(\cdot)$	Probability density function of the gamma distribution
$\boldsymbol{I}$	Unit matrix
$\jmath$	Imaginary unit
$\ln$	Natural logarithm function
$\mathcal{N}(\cdot)$	Probability density function of the Gaussian distribution
$p(\cdot)$	Probability density function
$\Pr[\cdot]$	Probability
$\boldsymbol{R}(\cdot)$	Autocorrelation matrix

AIC	Akaike Information Criterion
AR	AutoRegressive
ARMA	AutoRegressive Moving Average
BAYOMA	BAYesian Operational Modal Analysis
BIC	Bayesian Information Criterion
CCR	Cumulative Contribution Ratio
CV	Cross Validation
c.o.v.	Coefficient Of Variance
DI	Damage Indicator
DOF	Degree Of Freedom
EOM	Equation Of Motion
FE	Finite Element

FFT	Fast Fourier Transform
iid	Independent and Identically Distributed
MAC	Modal Assurance Criterion
MD	Mahalanobis Distance
NDSF	Nair's Damage Sensitive Feature
PCA	Principal Component Analysis
PDF	Probability Density Function
PSD	Power Spectral Density
SHM	Structural Health monitoring
SSI	Stochastic Subspace Identification
SVD	Singular Value Decomposition
SVS	Singular Value Spectrum
YW	Yule-Walker

Chapter 1

Introduction

1.1 Backgrounds

1.1.1 Motivation

Management of aging infrastructures is a crucially important issue confronting civil engineering professionals. Aging bridges have revealed deterioration leading to serious accidents. The collapse of the I-35W Mississippi River Bridge in Minneapolis, Minnesota, USA on August 1, 2007, was an unprecedented shock to the civil engineering community. National Transportation Safety Board [1] reported that the accident was caused by a design error in the loading capacity of its gusset plates. Although several structural deficiencies were discovered by inspection in advance to the collapse, the retrofit project was delayed while evaluating reinforcement plans. Severe damages of bridges in service were also discovered in Japan. Figure 1.1 shows the pictures of the ruptured diagonal truss member on Kisogawa Bridge for instance [2]. The lack of anti-corrosion performance on the member caused severe corrosion leading to the rupture. The urgent restoration required traffic control for 115 days.

Nowadays, maintaining and improving bridge structures have become keen technical issues, since any light structural damage or defects in a bridge can potentially result in fatal accidents. Preventive maintenance is also essential to increase the life spans of the bridges and to avoid long-term traffic

Figure 1.1 Photographs of the ruptured member on Kisogawa Bridge [2]

interruptions. In Japan, more than 720 thousand highway bridges are in service, and most of the bridges were intensively constructed in 1960s and 1970s, when the high economic growth were raised [3]. Thus, over 50 % of the bridges will get older than 50 years old until 2020s. Road Bureau of MLIT (Ministry of Land, Infrastructure, Transport and Tourism in Japan) therefore provided guideline for inspection of the highway bridges, where visual inspections once in 5 years are required for each of the bridges. The recent annual report provided by MLIT [4] shows that effort made by the bridge owners has provided steady improvement in those management tasks. However, there is still concern with financial problems and limitation of human resources for sustainable management of the bridges [5]. Furthermore, the rapid economic growth arising in the developing countries will possibly engender further issue to maintain their bridges in several decades. Damage detection for screening the structural health condition is therefore a challenging task to realize effective management of the bridges.

Structural health monitoring (SHM) provides a research field for nondestructive evaluation based on physical measurements and computer analyses to complement existing visual inspection methods. Local deteriorations of structures can be detected or evaluated by nondestructive testing measuring strain, displacements, acoustics, electric currents, hardness, magnetic fields, X-rays, and so on [6]. Those local testing methods enable detailed inspection on a specific part of the structures. For assessment of the whole structure, however, the local methods require cautiously planned inspection to avoid risk of overlooking failures. In order to realize a convenient screening method in practice, it is desirable to develop a technique to find the integrity of the whole bridge through its global mechanical properties. Techniques of SHM based on vibration measurements have been attracting bridge owners because of their potential feasibility for effective inspection. The main advantage of the vibration based SHM is that measurements at one or several locations are sufficient to assess the condition of the whole structure. In practice, however, decision-making for bridge maintenance involves difficulty caused by the uncertainty of natural phenomena. This study therefore aims to investigate methodologies to handle the uncertainty and to propose strategy how to utilize SHM to bridge maintenance in practice.

1.1.2 Overview of existing studies

The vibration based SHM relies upon the fact that a local stiffness change affects the global dynamic characteristic of the structure [7]–[9]. That is, changes in structural integrity of bridges engender changes in their modal properties such as natural frequencies, damping ratios and mode shapes. Analytical researches showed relationships between local stiffness and the global dynamic characteristic of the structure [10]–[12]. Numerical and experimental investigations have made to justify the feasibility of the vibration based SHM for various structures [13]–[21]. Los Alamos National Laboratory [7] summarized fundamental researches that have made up to 1990s. Consequently, vibration-based SHM is a useful technique to detect stiffness changes in structures if they can be excited easily. Recent studies adopt statistical approaches to vibration-based SHM aiming at reasonable decision-making [22]–[26].

Especially, improvement in computational performance in these days has developed a novel research area adopting Bayesian statistics. Pattern recognition and machine learning based on the Bayesian theory have produced innovative studies for the statistical SHM [25]–[32].

The modal properties of structures are estimated from vibration responses of the structures by means of numerical inverse problem [7], [33]–[36]. Two commonly used means are forced vibration tests and ambient vibration tests [35]. In the forced vibration test, by a shaker, impact hammer or other means are required to excite the bridges. In the ambient vibration test, the bridges are excited using various natural sources such as wind and ground motion. The ambient vibration based SHM enables monitoring without interrupting traffics on the bridges. Especially for short and medium span bridges, the traffics can be source of ambient vibration. Thus, for SHM of those bridges, ambient vibration tests using the traffic-induced vibration can be a more convenient method than the forced vibration test. The ambient vibration based modal identification are called operational modal analysis or output-only modal analysis since it enables to identify modal properties of the mechanical system under operation only from the measurable outputs of the system. Studies given in recent decades [36]–[48] enabled more reliable operational modal analysis methods.

Aiming to maintain structural safety of actual bridges in field, a lot of studies have adopted the operational modal analyses [22], [24], [46], [49]–[53]. For instance, Zhang [22] showed statistical feasibility of vibration based SHM by numerical model-based analysis. Chang et al. [50] showed that stochastic changes of modal properties caused by the damages on bridges can be detected using traffic induced vibration considering field experiments on actual bridges with artificially severed members. Long-term monitoring on actual bridges in service is operated in [24], [52], [53] for practical decision making. Most of those precedent studies specifically examine the change in modal parameters of structures.

In ambient vibration tests conducted on actual bridges, however, existing operational modal analysis methods require experience to identify the modal parameters since random natural phenomena involves unexpected effect onto measured data (for instance, see [9], [54]). To avoid the uncertainty on the modal identification, several existing studies have developed damage indicators directly extracted from the acquired time series of bridge vibration [51], [55], [56]. Although those damage indicators enabled prompt feature extraction, a reasonable standard for damage detection is not established yet. A reliable damage indicator with concise decision rule is therefore desirable to realize ambient vibration based SHM for bridges in practice.

1.2 Objectives

The following four levels of damage identification are usually discriminated [9] among the numerous existing studies.

Level 1 – *detection*: Is the structure damaged or not?
Level 2 – *localization*: Where is the damaged area located?
Level 3 – *quantification*: What is the extent of damage?
Level 4 – *prediction*: What is the remaining service life of the structure?

Several studies have reported successful results not only detection but also localization and quantification, if the modal properties are properly identified (e.g., [24], [50]). However, ambient vibration-based SHM of bridges still involves the following two obstructions in the damage detection: Firstly, precise modal identification requires experience on data processing, and thus more concise decision rule is required to realize screening method for the numerous existing bridges. Secondly, existing damage indicator [55] dismisses most of information included in the original data to generate a simple indicator, and thus it is less reliable than the modal properties. In practice, the reliability and the simplicity should be compatible for effective bridge management. Here, a room for improvement is remained in the statistical decision making procedure. For instance, Bayesian statistics provides convincing inference method for uncertain parametric models, and well-organized hypothesis testing enables reliable decision-making.

This thesis merely focuses on damage detection using vehicle-induced acceleration data measured on bridges. To provide a practical scale for prompt decision-making, the following features are required for the damage indicator:

Simplicity: The damage indicator directly derives from acceleration time series, and does not require troublesome procedure for identification.
Sensitivity: The damage indicator is sensitive to damage as well as the modal properties.
Objectivity: The damage has objective decision rule based on stochastic hypothesis testing.

This thesis proposes damage detection based on unsupervised machine learning [57]. That is, the healthy condition of a bridge is learned at first from vibration actually monitored on the healthy bridge. The procedure of the proposed damage detection method comprises following two steps:

Step 1 Acquire time series of acceleration from a vibrating bridge under healthy condition and describe its features by a mathematical model.
Step 2 Acquire new time series from bridge as well as Step 1 and examine statistical changes in the modal properties through the mathematical model.

To enable this 2-step damage detection, this thesis involves following contents: For Step 1, how to describe bridge vibration and its uncertainty are investigated through modal analysis theory. A parametric model describing bridge vibration is formulated as a stochastic regressive model. For Step 2, how to find statistical change is investigated through probability theory. Feature extraction method on the parametric space is investigated, instead of the modal identification in the conventional SHM. Especially, Bayesian statistics provides simple and reliable framework to make decision about bridge management. Each of the investigations is validated by a case study on bridges in field.

1.3 Outline of the Thesis

This thesis consists of 8 chapters including Chapter 1 for the introduction and Chapter 8 for the conclusion. Chapter 2 introduces the theoretical background of this thesis. Chapter 3 and Chapter 4 provide discussion about modal identification methods aiming at application to the bridges in field. In Chapter 5 and Chapter 6, novel damage indicators are investigated. In Chapter 7, feasibility analysis for the proposed method is discussed using one-year monitoring data.

Figure 1.2 describes the organization of the thesis. The contents in Chapter 2 to Chapter 7 are summarized as follows:

Chapter 2 Mathematical tools to investigate damage detection method are introduced. The probability theory is provided to describe random phenomena. The equation of motion representing vibrating bridges is transformed into linear parametric models such as a state space model and an autoregressive (AR) model.

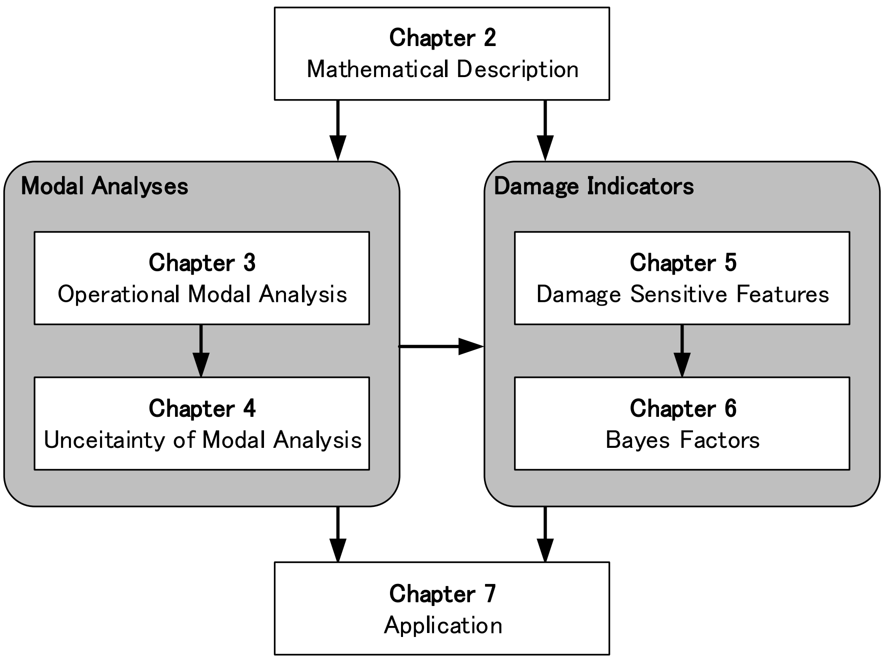

Figure 1.2 Organization of the thesis.

Chapter 3 Three existing modal analysis methods, namely, Yule-Walker (YW) method, stochastic subspace identification (SSI), and Bayesian operational modal analysis (BAYOMA) are reviewed. Brief case study for the YW method and SSI is given using traffic induced vibration of a truss bridge.

Chapter 4 Further investigation on the uncertainty involved in the modal identification is also provided for application of the modal analysis methods. SSI and BAYOMA are adopted to analyze experimental data on a long span cable-stayed bridge, where its modal properties vary with the wind speed blowing upon the bridge. The uncertainty of the identified modes is investigated by inspecting the modal analysis results.

Chapter 5 This chapter mainly aims to improve existing damage sensitive features in their sensitivity and reliability. To overcome disadvantages of a previously investigated damage indicator based on a univariate AR model, a novel damage indicator based on a multivariate AR model is proposed. Hypothesis testing is formulate to distinguish changes in the proposed damage sensitive features and to support decision-making.

Chapter 6 Based on the observation given in the previous chapters, the Bayesian statistics gives advanced damage indicator. The damage detection method presented in Chapter 5 is expanded and generalized. A probability distribution function for parameters of the AR models are investigated. Feature extraction method based on the distribution is presented for damage detection. Hypothesis testing for decision-making is simplified using a generalized likelihood ratio.

Chapter 7 The discussion given in above chapters are verified through a case study on an one-year long term monitoring. The proposed damage indicator is adopted to the monitored data to track changes in modal properties during the monitoring. Feasibility of the damage detection method is also investigated through vehicle loading tests introducing artificial damage imitating a fatigue crack to the bridge girder.

1.4 Target Bridge

This thesis provides case studies on a specific bridge throughout Chapter 3, Chapter 5 and Chapter 6 to investigate the modal analysis and the damage indicators. For convenience, this section provides a brief introduction of the field experiment in advance to those case studies.

The field experiments were conducted with a moving vehicle on an actual bridge. The target bridge for the experiment is a single lane simply supported through-type steel Warren truss bridge as presented in

Figure 1.3. The bridge has 59.2 m span length, 8 m maximum height, and 3.6 m width. The vehicle used for the experiment is a two-axle recreation vehicle (Serena; Nissan Motor Co. Ltd.) with total weight of about 21 kN. During the experiment, all traffic except the loading vehicle was prohibited. Two photoelectric switches were installed at the respective ends of the bridge to detect the vehicle entrance and exit. Eight uniaxial accelerometers were installed on the deck of the bridge to measure vertical vibrations as presented in Figure 1.3c. The sampling rate of each sensor was set as 200 Hz. The data is pre-processed with an antialiasing low-pass filter at cutoff frequency as 100 Hz before the sampling. Each of the sampled time series are de-trended, namely, the mean values and the linear trends of the acquired time series are removed in advance.

Five scenarios were considered in this study as shown in Figure 1.4. Initially, The INT scenario represents the intact bridge without damage. For the DMG1 scenario, a half cut damage was applied to the vertical truss member at the mid-span (see Figure 1.3c), and for the DMG2 scenario, a full cut damage was applied to the same member. After examining DMG2, the damaged member was repaired, which is

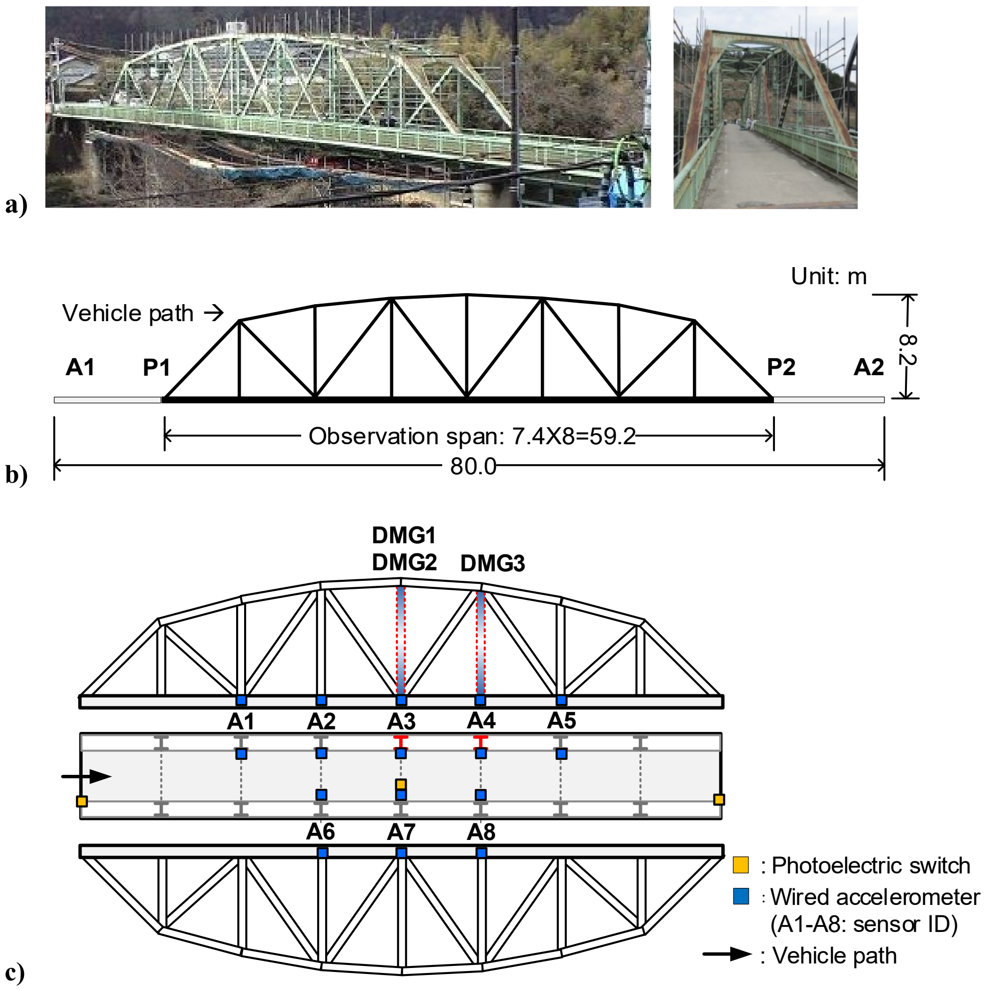

Figure 1.3 The target bridge: a) photograph; b) approximate size; c) sensor deployment.

denoted as the RCV scenario. Finally, for the DMG3 scenario, full cut was applied in a vertical member at 5/8th-span (see Figure 1.3c) after examining the RCV scenario. For the INT scenario, the vehicle was passed over at three different speeds; 30km/h, 40km/h, and 50km/h. Let INT30, INT40, and INT50

Table 1.1 Scenarios considered in the field experiment.

	Description	Vehicle Speed (km/h)	Number of Samples
INT30	Intact bridge	30	11
INT40	Intact bridge	40	10
INT50	Intact bridge	50	5
DMG1	Half cut in vertical member at mid-span	40	12
DMG2	Full cut in vertical member at mid-span	40	10
RCV	Recovery of the member at mid-span	40	10
DMG3	Full cut in vertical member at 5/8th-span	40	10

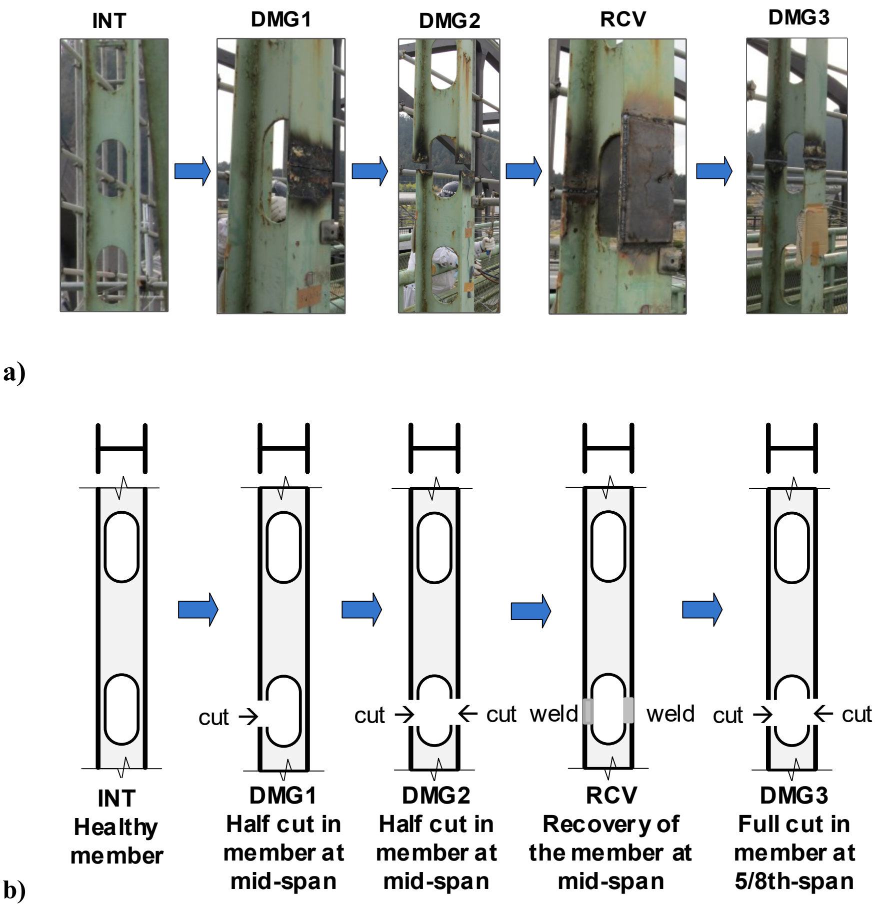

Figure 1.4 Artificial damages: a) Photographs; b) Schematic diagram

respectively represent the scenarios at the three kinds of vehicle speed. For the other scenarios, the vehicle was only passed at 40km/h. Table 1.1 summarizes the vehicle loading scenarios. Note that the sample numbers of the scenarios are deferent each other because of experimental limitation.

Figure 1.5 presents the time series and power spectral density (PSD) curves of the acquired acceleration at sensor A3 for the INT, DMG1 and DMG2 scenarios. Here the PSD curve is estimated as Welch's overlapped segment averaging estimator [58]. That is, the time series are divided into 8 segments with 50% overlap, each segment is windowed with a Hamming window, and the modified periodograms obtained by the fast Fourier transform are averaged to estimate the PSDs. The moments at the vehicle entrance and exit monitored by the photoelectric switches are depicted as vertical dashed lines in

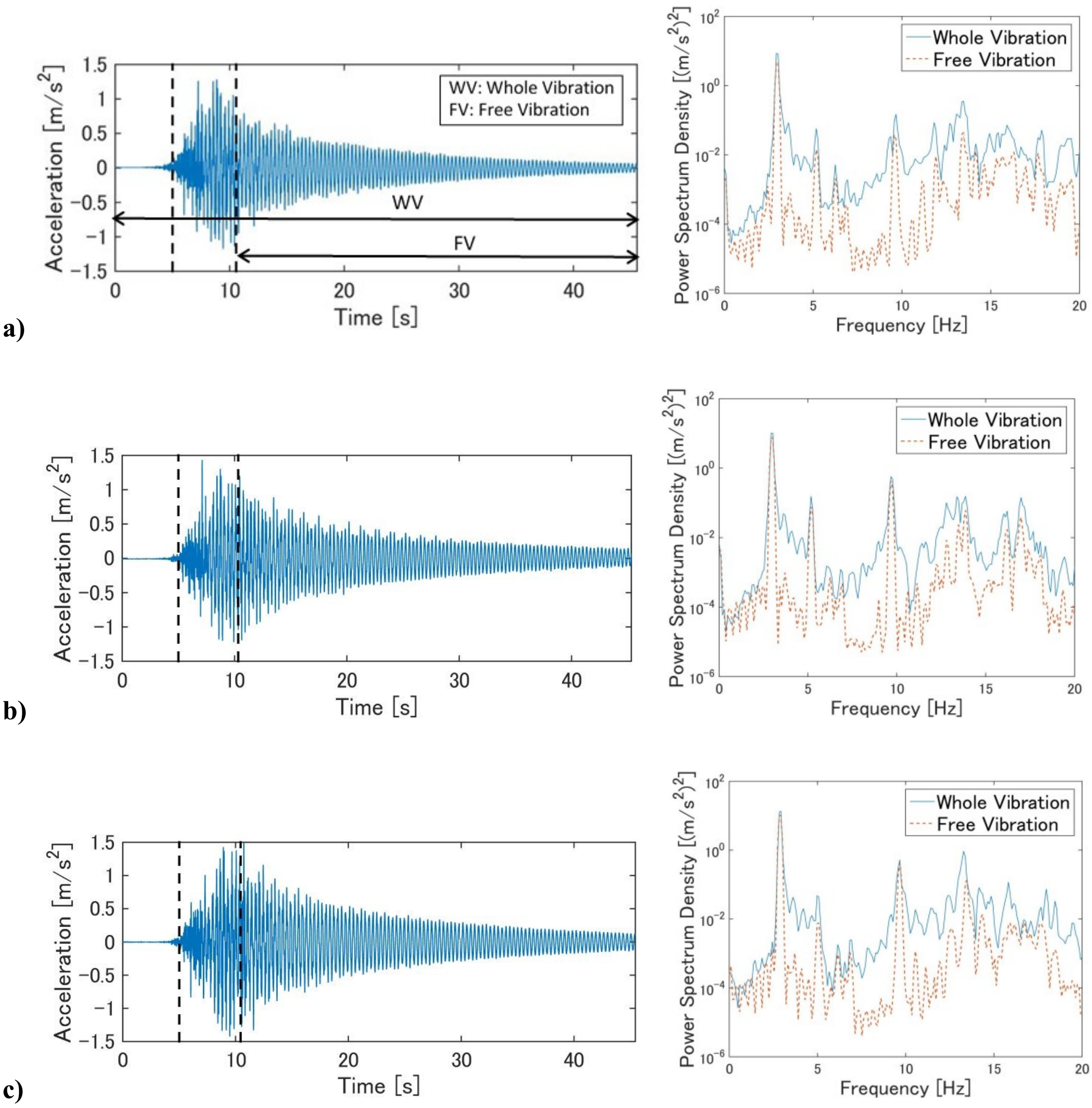

Figure 1.5 Examples of acquired time series at A3 sensor and their PSD curves:
a) For INT40; b) For DMG1; c) For DMG2.

Figure 1.5. According to the record of the photoelectric switches, the time series are separable at the moment of the vehicle exit. The time series after the vehicle exit can be interpreted as a free vibration data because no external loading significantly affected the bridge vibrations. Empirically, free vibration data are known to enable stable modal parameter identification because external loading can be a source of uncertainty for identification. However, the whole time series including excitation produced by a passing vehicle is still convenient for practical application because it requires no knowledge about the exit moment of vehicles. Therefore, this study examines both free vibration (FV) data and whole vibration (WV) data. Each of the intervals of the FV and WV data are depicted in Figure 1.5a.

The PSD curves in Figure 1.5 are estimated for both of the FV and the WV data. Those PSD curves provide instant view to grasp natural frequencies of the bridge as peaks in the curves. Note that the FV data gives more highlighted peaks since unwanted noise caused by the external forces is less than the WV data. Here, several dominant natural frequencies can be roughly examined by means of peak picking. However, there is still trouble to make decision about the possibility of damage in the bridge merely from those PSDs. That is because it is difficult to distinguish the changes caused by a damage from stochastic variance involved in the peaks appearing in the PSD curves. The following discussion investigates an effective methodology to find subtle changes caused by the damage in those data.

Chapter 2

Mathematical Description

2.1 Introduction

To develop a damage detection method of vibrating structure, this thesis investigates a method to detect stochastic changes in the vibration data. This chapter therefore provides mathematical description to investigate the damage detection method. As mentioned in Section 1.2, this study focuses on damage detection merely from vehicle induced acceleration data of bridges. Thus, the damage detection method should include methodologies to deal with following problems.

- How to describe random vibration of bridges.
- How to distinguish damage from huge amount of data.

Both of the above two problems are generally involved in the probability theory that enables to investigate uncertain phenomena.

The first problem is one of targets of modal analysis theory [35], which provides methodology to identify valid models of vibrating bridges, namely, modal models consisting of modal properties. In practice, however, inverse problems to estimate the modal properties involve difficulties caused by unexpected disturbance derived from uncertain natural phenomena. Several existing methods on modal analysis provide possible ways to reduce uncertainty from acquired data from vibrating structures [37], [46], [47] (see also Chapter 3). Most of the ambient vibration based modal analyses consider the probability theory to produce estimators of the modal properties. They usually adopt parametric models to describe random vibrations of the structures since their modal properties are represented by parameters in probability density functions (PDFs) describing the stochastic model. Referring the existing studies investigating modal analyses, how to make a convincing parametric model is one of their central tasks.

The second problem is involved in stochastic anomaly detection. Here, the main purpose of damage detection is to find changes in the modal properties through the parametric model representing the bridge vibration. The existing modal analysis methods are one of valid ways to enable convincing feature extraction since they provide plausible estimators of the modal properties. However, the problem of the unexpected disturbance have not been totally solved yet. That is because the natural excitation tends to violate mathematical assumptions given in modal analysis theory (For further discussion, see also Chapter 3 and Chapter 4). To realize the detection of change in modal properties, an efficient feature extraction method and statistic hypothesis testing method are needed. According to the machine learning theory [57], Bayesian statistics possibly provides effective feature extraction and hypothesis testing.

This chapter therefore establishes foundation for making a reliable decision on bridge safety based upon probability theory and modal analysis theory. Following discussions are included in this chapter: Firstly, the probability theory is introduced in Section 2.2 to describe the random phenomena. Bayesian and frequentist viewpoints are mutually reviewed. Especially for a linear regressive model, which are essential for identification of modal properties, estimation and inference procedures are provided. Secondly, Section 2.3 provides basic models of vibrating structures. Time invariant state space model enables to describe vibrating structures as a parametric model with modal properties. The state space model can be approximated to a simplified model, which is so-called an autoregressive (AR) model. These models are essential to the modal analysis.

2.2 Probability Theory

2.2.1 Basic properties

Since vibrations of bridges are resulted from complicated relation with natural phenomena, it is usually impossible to describe the responses exactly. The probability theory provides a consistent framework for the quantification and manipulation of those uncertain phenomena. The term of ‘probability’ is formally defined by the Kolmogorov’s axioms [59] based on the set theory and the measure theory. This section merely gives brief outline of the probability theory. The Kolmogorov’s axioms justify the following well-known characteristics of the probability: Letting a set $\mathcal{E}$ denote one of random events for which probability is evaluated, and a set Ω denotes the sampling space including the random events (i.e., $\mathcal{E} \in \Omega$) and $\Pr[\mathcal{E}]$ represents a probability such that the random event $\mathcal{E}$ occurs. According to the definition, the probability satisfies the following conditions.

$$0 \leq \Pr[\mathcal{E}] \leq 1. \tag{2.1}$$

$$\Pr[\Omega] = 1. \tag{2.2}$$

$$\Pr[\cup_{i=1}^{\infty} \mathcal{E}_i] = \Sigma_{i=1}^{\infty} \Pr[\mathcal{E}_i] \tag{2.3}$$

where, $\mathcal{E}_1, \mathcal{E}_2, ...$ denote mutually exclusive random events. The above conditions ensure that the probability measures uncertainty of random events onto the scale from 0 to 1. That is, an event never occurs produce probability 0 and an event always occurs produce probability 1.

Let $\mathcal{A}$ and $\mathcal{B}$ respectively represent random events, $\Pr[\mathcal{A}, \mathcal{B}]$ denotes a joint probability representing “the probability such that both of $\mathcal{A}$ and $\mathcal{B}$ occur”, and $\Pr[\mathcal{A}|\mathcal{B}]$ denotes a conditional probability representing “the probability such that $\mathcal{A}$ occurs supposing $\mathcal{B}$ is given in advance”. For the joint and conditional probabilities, this thesis only equips following two elementary rules to manipulate uncertainty, which are respectively known as the sum rule and the product rule [57].

$$\text{sum rule} \quad \Pr[\mathcal{A}] = \textstyle\sum_{\mathcal{B}} \Pr[\mathcal{A}, \mathcal{B}]. \tag{2.4}$$

$$\text{product rule} \quad \Pr[\mathcal{A}, \mathcal{B}] = \Pr[\mathcal{B}|\mathcal{A}]\Pr[\mathcal{A}]. \tag{2.5}$$

Here, $\Sigma_{\mathcal{B}}$ denotes summation over all exclusive events included in the sample space. The sum rule is directly produced from the Kolmogorov’s axiom and the product rule is the definition of the conditional probability itself. In particular, if the relationship that $\Pr[\mathcal{A}, \mathcal{B}] = \Pr[\mathcal{A}] \Pr[\mathcal{B}]$ is given, the events $\mathcal{A}$ and $\mathcal{B}$ are said to be independent.

Assuming $\Pr[\mathcal{A}] \neq 0$, the product rule immediately produces the following relationship between conditional probabilities.

$$\Pr[\mathcal{B}|\mathcal{A}] = \frac{\Pr[\mathcal{A}|\mathcal{B}]\Pr[\mathcal{B}]}{\Pr[\mathcal{A}]} \tag{2.6}$$

The above relationship is called Bayes’ theorem, which has a central role in the Bayesian statistics.

Practically, the random events are quantified by some random valuables, which is defined as mapping from the sample space Ω to a real number. For example, regarding bridge vibrations as random events, the acceleration monitored at a specific moment on a specific point of the vibrating bridge can be regarded as one of random variables representing the uncertain bridge vibration. This thesis adopts only continuous random valuables. Unless otherwise noted, PDF are presumed to exist for the random variables (For further discussions, see [59]). Letting ξ be a random variable, the PDF for ξ is defined as

$$p_{\xi}(x) = \frac{\mathrm{d}}{\mathrm{d}x} \Pr[\xi \in (-\infty, x)]. \tag{2.7}$$

Accordingly, the probability such that ξ lies in an interval (a, b) is given as

$$\Pr[\xi \in (a, b)] = \int_a^b p_{\xi}(x)\, \mathrm{d}x. \tag{2.8}$$

Since the value of the random variable must lie somewhere on the real axis, the PDF must satisfy following condition.

$$\int p_{\xi}(x)\mathrm{d}x = \lim_{\gamma \to \infty} \int_{-\gamma}^{\gamma} p_{\xi}(x)\mathrm{d}x = 1 \tag{2.9}$$

where the integral without notation denotes the integral over the whole of the real axis. In this thesis, for simplicity, integrals without notation represent the integrals taken over whole domain of the relevant variables as well as Eq. 2.9. Let $\xi_1, \xi_2, \dots, \xi_D$ denote D random variables, and let a vector $\boldsymbol{\xi}$ represent the collection of those random variables such that $\boldsymbol{\xi} = [\xi_1, \xi_2, \dots, \xi_D]^{\mathrm{T}}$. The joint probability for those random values is then functionally described by a joint PDF. The joint PDF $p_{\boldsymbol{\xi}}(\mathbf{x}) = p_{\boldsymbol{\xi}}(x_1, x_2, \dots, x_D)$ is defined by joint probability for $\xi_1, \xi_2, \dots, \xi_D$ as

$$p_{\boldsymbol{\xi}}(\mathbf{x}) = \frac{\partial^D}{\partial x_1 \dots \partial x_D} \Pr[\xi_1 \in (-\infty, x_1), \dots, \xi_D \in (-\infty, x_D)\ ]. \tag{2.10}$$

If the joint PDF of two random variables x and y satisfy relationship such that $p(x, y) = p(x)p(y)$, then the x and y are said to be independent to each other as well as random events.

According to the product rule given in Eq. 2.5, a conditional PDF is defined under a specific random event. The conditional PDF for ξ under a random event $\mathcal{E}$ is defined by the following relationship as well as Eq. 2.7.

$$p_\xi(x|\mathcal{E}) = \frac{\mathrm{d}}{\mathrm{d}x} \Pr[\xi \in (-\infty, x)|\mathcal{E}]. \tag{2.11}$$

A conditional probability under a condition represented by a random variable is formally defined using the abstract Lebesgue integral [59]. For simplicity, this thesis adopts the following narrow definition for those conditional probabilities instead of the formal definition.

$$\Pr[\mathcal{E}|\xi = x] = \frac{p_\xi(x|\mathcal{E})\Pr[\mathcal{E}]}{p_\xi(x)} \tag{2.12}$$

where the PDF $p_\xi(x)$ is assumed as $p_\xi(x) \neq 0$. Accordingly, a conditional PDF for another random variable η under the condition such that $\xi = x$ is defined as

$$p_\eta(y|\xi = x) = \frac{\mathrm{d}}{\mathrm{d}y} \Pr[\eta \in (-\infty, y)|\xi = x]. \tag{2.13}$$

Hereafter, random variables and their realized values are denoted by same letters and the suffixes put to the PDFs are omitted for simplicity. For instance, $p_\eta(y|\xi = x)$ in Eq. 2.13 is shortly noted as $p(y|x)$.

The sum and product rules of probability are equally applied to the random variables represented by joint and conditional PDFs as follows [57].

$$\text{sum rule} \quad p(x) = \int p(x, y)\mathrm{d}y. \tag{2.14}$$

$$\text{product rule} \quad p(x, y) = p(x|y)p(y). \tag{2.15}$$

Accordingly, the Bayes' theorem for random variables is given as

$$p(y|x) = \frac{p(x|y)p(y)}{p(x)}. \tag{2.16}$$

For multivariate PDFs, the sum and product rules are also formed in a similar way as Eqs. 2.14 and 2.15. Thus, Bayes' theorem for two vectors $\mathbf{x}$ and $\mathbf{y}$ is given as follows.

$$p(\mathbf{y}|\mathbf{x}) = \frac{p(\mathbf{x}|\mathbf{y})p(\mathbf{y})}{p(\mathbf{x})}. \tag{2.17}$$

Letting $f(x)$ is some function for a random variable x following a PDF $p(x)$, the expectation of the function is defined by

$$\mathbb{E}_x[f] = \int f(x)p(x)\mathrm{d}x. \tag{2.18}$$

Expectations with respect to multivariate random variable are also definable in a similar way, i.e., $\mathbb{E}_{\mathbf{x}}[f] = \int f(\mathbf{x})p(\mathbf{x})\mathrm{d}\mathbf{x}$. For a conditional distribution, so called conditional expectation is defined as

$$\mathbb{E}_x[f|y] = \int f(x)p(x|y)\mathrm{d}x. \tag{2.19}$$

According to the expectation, variation of the univariate function is defined by

$$\mathrm{Var}[f] = \mathbb{E}_x[(f(x) - \mathbb{E}_x[f(x)])^2]. \tag{2.20}$$

In particular, the expectation and variance of the random variable x itself, which are conventionally denoted as μ and σ^2, are given as follows.

$$\mu = \mathbb{E}_x[x] = \int xp(x)\mathrm{d}x. \tag{2.21}$$

$$\sigma^2 = \mathrm{Var}[x] = \mathbb{E}_x[(X - \mu)^2]. \tag{2.22}$$

For two random variables x and y, the covariance is defined by

$$\mathrm{Cov}[x, y] = \mathbb{E}_{x,y}\left[\{x - \mathbb{E}_x(x)\}\{y - \mathbb{E}_y(y)\}\right] \tag{2.23}$$

which expresses the extent to which x and y vary together. If x and y are independent, their covariance must be 0. Similarly, for two vectors of the random variables $\mathbf{x}$ and $\mathbf{y}$, a covariance matrix is defined by

$$\mathrm{Cov}[\mathbf{x}, \mathbf{y}] = \mathbb{E}_{\mathbf{x},\mathbf{y}}\left[\{\mathbf{x} - \mathbb{E}_{\mathbf{x}}(\mathbf{x})\}\{\mathbf{y} - \mathbb{E}_{\mathbf{y}}(\mathbf{y})\}^{\mathrm{T}}\right]. \tag{2.24}$$

For simplicity, let $\mathrm{Cov}[\mathbf{x}]$ shortly denote $\mathrm{Cov}[\mathbf{x}, \mathbf{x}]$.

2.2.2 Frequentist and Bayesian statistics for modal analysis

Classically, the probability is regarded as a scale to measure how frequently the random events occur. This viewpoint is sometimes referred as frequentist view comparing to the Bayesian view [57]. The

Bayesian view is fundamentally based upon the Bayes theorem. For instance in Eq. 2.6, the Bayes' theorem enables transformation from the probability $\Pr[\mathcal{B}]$ to the conditional probability $\Pr[\mathcal{B}|\mathcal{A}]$. This property therefore provides following application: Letting $\mathcal{A}$ be one of the observable random events, and letting the $\Pr[\mathcal{B}]$ describe the subjectively predefined probability of the event $\mathcal{B}$ prior to the observation, then $\Pr[\mathcal{B}|\mathcal{A}]$ describes the probability of the event $\mathcal{B}$ posterior to observation of the event $\mathcal{A}$. Here, the probabilities provides scale to measure subjective uncertainty of the event $\mathcal{B}$. The Bayesian viewpoint allows such subjective interpretation of probability. This allowance therefore provides more general framework to statistic, which is referred as Bayesian statistics. In the Bayesian statistics, the probabilities $\Pr[\mathcal{B}]$ and $\Pr[\mathcal{B}|\mathcal{A}]$ are respectively referred as a prior probability and a posterior probability for the event $\mathcal{B}$ with respect to the event $\mathcal{A}$.

Aiming at engineering application of the probability theory, parametric models are common tools to describe randomly occurring natural phenomena. In most cases, those random events are mathematically described using parametric model, which is conditional PDFs for observable random variables with adjustable parameters. For instance, random vibration of bridges can be described as a function of modal properties [44]. Here, let $\mathcal{D}$ is a dataset of random variables observed from a repeatable event, and $\boldsymbol{\theta}$ is a vector consisting of parameters for the parametric model. The parametric model representing the randomly observed dataset $\mathcal{D}$ is formulated into a conditional PDF as $p(\mathcal{D}|\boldsymbol{\theta})$. This PDF is also regarded as a function for the adjustable parameters $\boldsymbol{\theta}$ with fixed $\mathcal{D}$ since the actually observed dataset $\mathcal{D}$ is invariant. In this case the PDF $p(\mathcal{D}|\boldsymbol{\theta})$ is referred as the likelihood function for $\boldsymbol{\theta}$, which evaluates how likely the observation of dataset $\mathcal{D}$ occurs with respect to the parameters $\boldsymbol{\theta}$.

Especially for the operational modal analysis, the unknown modal properties are identified from the monitored vibration data, i.e., the parameters $\boldsymbol{\theta}$ are inferred from observed dataset $\mathcal{D}$. The frequentist and the Bayesian paradigm provide different strategies for the inference. In the frequentist paradigm, the parameters $\boldsymbol{\theta}$ are supposed to have specific values that are statistically determined by 'estimators'. One of the widely used estimators is a maximum likelihood that maximizes the likelihood function $p(\mathcal{D}|\boldsymbol{\theta})$. On the other hand, in the Bayesian paradigm, the parameters $\boldsymbol{\theta}$ are regarded as random variables expressed through a probability distribution as follows: Assuming that a PDF $p(\boldsymbol{\theta})$ represents the subjective uncertainty of the parameter $\boldsymbol{\theta}$ before observing data, and then a conditional PDF given as $p(\boldsymbol{\theta}|\mathcal{D})$ evaluates the uncertainty after observing the data. The probability distributions relevant to $p(\boldsymbol{\theta})$ and $p(\boldsymbol{\theta}|\mathcal{D})$ are respectively referred as a prior distribution and a posterior distribution. The following Bayes' theorem is used to convert the prior distribution into the posterior distribution.

$$p(\boldsymbol{\theta}|\mathcal{D}) = \frac{p(\mathcal{D}|\boldsymbol{\theta})p(\boldsymbol{\theta})}{p(\mathcal{D})}. \tag{2.25}$$

The denominator in Eq. 2.25 is the normalization constant, which ensures the sum rule upon the posterior PDF, i.e., the integral of $p(\boldsymbol{\theta}|\mathcal{D})$ over $\boldsymbol{\theta}$ is ensured to be 1. From the sum and the product rules, the denominator is expressed as follows using the prior distribution and the likelihood function.

$$p(\mathcal{D}) = \int p(\mathcal{D}|\boldsymbol{\theta})p(\boldsymbol{\theta})\mathrm{d}\boldsymbol{\theta}. \tag{2.26}$$

In Bayesian statistics, the normalization constant in Eq. 2.26 is usually regarded as fixed constant. Thus, Eq. 2.25 can be simplified to the following proportional form.

$$p(\boldsymbol{\theta}|\mathcal{D}) \propto p(\mathcal{D}|\boldsymbol{\theta})p(\boldsymbol{\theta}). \tag{2.27}$$

where $\propto$ denotes the both hand sides of the notation are proportional to each other. Since the integral of $p(\boldsymbol{\theta}|\mathcal{D})$ over $\boldsymbol{\theta}$ is ensured to be 1, Eq. 2.27 enables to infer the posterior distribution of $\boldsymbol{\theta}$ only from the prior distribution, the likelihood function, and the observed dataset $\mathcal{D}$. This statistical inference method is referred as 'Bayesian inference.'

The Bayesian inference allows the inclusion of subjective prior knowledge naturally. This property can be one of benefit of the Bayesian viewpoint if a reasonable prior distribution is available. However, this property also means that the posterior distribution depends on the subjective choice of the prior distribution, and thus poor choice of the prior distribution results in an unreliable posterior distribution. To avoid subjective choice of the prior distribution and to enable objective analysis based on observed data itself, noninformative priors are often adopted, which are designed to have as little influence on the posterior distribution as possible. For instance, Jeffreys [60] proposed one of widely used noninformative priors, so-called Jeffreys priors, whose functional forms are modified to be invariant with any transformation for their parameters. Once a posterior distribution is obtained from observed data, the posterior distribution can act as the prior distribution when additionally observed dataset is available. Thus, using the sequentially observed datasets, each of the datasets updates the current posterior distribution to the revised one. This approach, which is known as a sequential algorithm or an on-line algorithm, can be an efficient way to process large amount of data such as time series of acceleration obtained from long term monitoring of bridges. To realize objective analysis for decision-making, this thesis aim to utilize the Jeffreys prior and sequential algorithm for damage detection.

2.2.3 Linear regressive models

This section provides linear regressive models, which plays an important role in modal analysis theory. The regressive model provides prediction of a target variable $t \in \mathbb{R}$ under a given D-dimensional vector $\boldsymbol{x} = [x_1, x_2, \dots, x_D]^{\mathrm{T}}$ as input variables. One of the simplest form of the regressive models is linear function of the input variables as

$$t = w_1 x_1 + w_2 x_2 + \cdots + w_D x_D + \epsilon = \boldsymbol{w}^{\mathrm{T}}\boldsymbol{x} + \epsilon \tag{2.28}$$

where, ϵ denotes a random variable representing additive noise. The coefficients denoted as $\boldsymbol{w} =$

$[w_1, w_2, \dots, w_D]^{\mathrm{T}}$ are referred as 'regressive coefficients.' Hereafter, the relationship given in Eq. 2.28 is simply referred as 'linear regressive model.'

Assume that the additive noise ϵ is a zero-mean Gaussian random variable. Letting β denote a precision parameter defined as $\beta = (\mathrm{Var}[\epsilon])^{-1}$, then Eq. 2.28 produces conditional PDF for t as

$$p(t|\boldsymbol{x}, \boldsymbol{w}, \beta) = \mathcal{N}(t|\boldsymbol{w}^{\mathrm{T}}\boldsymbol{x}, \beta^{-1}) = \left(\frac{\beta}{2\pi}\right)^{\frac{1}{2}} \exp\left[-\frac{\beta}{2}(t - \boldsymbol{w}^{\mathrm{T}}\boldsymbol{x})^2\right]. \tag{2.29}$$

Here $\mathcal{N}(t|\boldsymbol{w}^{\mathrm{T}}\boldsymbol{x}, \beta^{-1})$ denotes the PDF of the univariate Gaussian distribution with expectation $\boldsymbol{w}^{\mathrm{T}}\boldsymbol{x}$ and variance β^{-1}, and $\exp[\cdot]$ denotes the natural exponential function.

Now let a dataset of input variables $\boldsymbol{X} = [\boldsymbol{x}_1, \boldsymbol{x}_2, \dots, \boldsymbol{x}_N]^{\mathrm{T}} \in \mathbb{R}^{N \times D}$ with a vector of corresponding target variables $\boldsymbol{t} = [t_1, t_2, \dots, t_N]^{\mathrm{T}}$ be given. Assuming that the target variables are drawn independently from the distribution given in Eq. 2.29, the likelihood function for the adjustable parameters $\boldsymbol{w}$ and β is obtained as

$$p(\boldsymbol{t}|\boldsymbol{X}, \boldsymbol{w}, \beta) = \prod_{n=1}^{N} \mathcal{N}(t_n|\boldsymbol{w}^{\mathrm{T}}\boldsymbol{x}_n, \beta^{-1}). \tag{2.30}$$

The input variable $\boldsymbol{X}$ will always appear in the set of conditioning variables, and thus from now on, the input variables will be omitted from expressions for simplicity. Taking the logarithm of the likelihood function shown in Eq. 2.30, following relationship is obtained.

$$\ln p(\boldsymbol{t}|\boldsymbol{w}, \beta) = \sum_{n=1}^{N} \ln \mathcal{N}(t_n|\boldsymbol{w}^{\mathrm{T}}\boldsymbol{x}_n, \beta^{-1}) = \frac{N}{2}\ln\beta - \frac{N}{2}\ln(2\pi) - \frac{1}{2}\beta E(\boldsymbol{w}). \tag{2.31}$$

Here, ln denotes the natural logarithm function, and $E(\boldsymbol{w})$ denotes the sum-of-squares error function defined as

$$E(\boldsymbol{w}) = \sum_{n=1}^{N} (t_n - \boldsymbol{w}^{\mathrm{T}}\boldsymbol{x}_n)^2 = ||\boldsymbol{t} - \boldsymbol{X}\boldsymbol{w}||^2 \tag{2.32}$$

where $||\cdot||$ denotes the Euclidean norm of a vector. The logarithm of the likelihood function given as Eq. 2.31 is referred as the log likelihood function.

As mentioned in Section 2.2.2, in frequentist paradigm, parameters representing stochastic models are statistically determined by estimators. The maximum likelihood of $\boldsymbol{w}$ is defined as the estimator that maximize the log likelihood function given in Eq. 2.31. Thus, the maximum likelihood is obtained by means of the least-squares method that minimizes the error function $E(\boldsymbol{w})$ shown in Eq. 2.32. Assuming that $N > D$ and the matrix $\boldsymbol{X}$ is full rank, the maximum likelihood is given as

$$\widehat{\boldsymbol{w}} = (\boldsymbol{X}^{\mathrm{T}}\boldsymbol{X})^{-1}\boldsymbol{X}^{\mathrm{T}}\boldsymbol{t} = \boldsymbol{X}^{\dagger}\boldsymbol{t} \tag{2.33}$$

where $\widehat{\boldsymbol{w}}$ denotes maximum likelihood of $\boldsymbol{w}$, and $\boldsymbol{X}^{\dagger}$ denotes the Moor-Penrose pseudo-inverse of the matrix $\boldsymbol{X}$. Accordingly, the maximum likelihood of the precision parameter β is obtained as

$$\hat{\beta} = \frac{N}{E(\widehat{\boldsymbol{w}})}. \tag{2.34}$$

In Bayesian paradigm, on the other hand, the prior distributions of the parameters $\boldsymbol{w}$ and β are beforehand assumed, and then their posterior distributions are obtained by the Bayesian inference based on the Bayes' theorem as follows.

$$p(\boldsymbol{w}, \beta|\boldsymbol{t}) = \frac{p(\boldsymbol{t}|\boldsymbol{w},\beta)p(\boldsymbol{w},\beta)}{p(\boldsymbol{t})} \tag{2.35}$$

where $\mathrm{p}(\boldsymbol{w}, \beta)$ stands for a prior joint PDF for $\boldsymbol{w}$ and β, which is predefined prior to the observation of $\boldsymbol{t}$, $\mathrm{p}(\boldsymbol{t})$ is a constant in manner of Bayesian inference, and thus the posterior PDF $\mathrm{p}(\boldsymbol{w}, \beta|\boldsymbol{t})$ is obtained only from the observed data $\boldsymbol{t}$ and the prior PDF $\mathrm{p}(\boldsymbol{w}, \beta)$.

As mentioned in Section 2.2.2, when no valuable information is available before observing data, noninformative priors can be a reasonable choice to reduce the dependence on the prior and to realize objective investigation. In general, letting $\boldsymbol{\theta}$ denote a vector consisting of parameters representing a parametric model, the PDF of a multivariate Jeffreys prior $\pi(\boldsymbol{\theta})$ satisfies following condition [60], [61].

$$\pi(\boldsymbol{\theta}) \propto |\boldsymbol{H}(\boldsymbol{\theta})|^{1/2} \tag{2.36}$$

where, $|\cdot|$ denotes determinant of a matrix. $\boldsymbol{H}(\boldsymbol{\theta})$ in Eq. 2.36 is the Fisher's information matrix whose (i, j) element is defined as

$$[\boldsymbol{H}(\boldsymbol{\theta})]_{ij} = -\int p(x|\boldsymbol{\theta}) \frac{\partial^2}{\partial\theta_i \partial\theta_j} \ln p(x|\boldsymbol{\theta})\,\mathrm{d}x \tag{2.37}$$

where, $p(x|\boldsymbol{\theta})$ denotes the PDF representing the parametric model. According to the Fisher information matrix for the parameters $\boldsymbol{w}$ and β, the Jeffreys prior satisfies following condition.

$$\pi(\boldsymbol{w}, \beta) \propto \beta^{\frac{D}{2}-1} \tag{2.38}$$

See Appendix to find the detailed expansion leading to Eq. 2.38. Note that the prior $\pi(\boldsymbol{w}, \beta)$ given in Eq. 2.38 is an improper distribution, i.e., the prior cannot be correctly normalized because the integral over the parameters diverges. Thus, in strict sense, the parameters $\boldsymbol{w}$ and β represented by the improper distribution are not random variables. In practice, however, improper priors can often be used when the corresponding posterior distribution is supposed to be proper [57], i.e., the integral over the parameters for the posterior distribution is correctly converges to 1. According to the Bayes' theorem, the Jeffreys prior $\pi(\boldsymbol{w}, \beta)$ given in Eq. 2.38 and the likelihood function given in Eq. 2.30 provide the following proper posterior distribution $p(\boldsymbol{w}, \beta|\boldsymbol{t})$ if $N > D$ and the dataset of the input variables $\boldsymbol{X}$ is full rank (see also Appendix).

$$p(\boldsymbol{w},\beta|\boldsymbol{t}) = \mathcal{N}(\boldsymbol{w}|\widehat{\boldsymbol{w}},(\beta\boldsymbol{X}^{\mathrm{T}}\boldsymbol{X})^{-1})Gam\left(\beta\middle|\frac{N}{2},\frac{1}{2}E(\widehat{\boldsymbol{w}})\right) \tag{2.39}$$

Here, $\mathcal{N}(\cdot)$ and $Gam(\cdot)$ are respectively denote the PDFs of the multivariate Gaussian distribution and the gamma distribution defined as

$$\mathcal{N}(\boldsymbol{x}|\boldsymbol{\mu},\boldsymbol{\Sigma}) = \frac{1}{(2\pi)^{d/2}}\frac{1}{|\boldsymbol{\Sigma}|^{1/2}} \ \exp\left(-\frac{1}{2}(\boldsymbol{x}-\boldsymbol{\mu})^{\mathrm{T}}\boldsymbol{\Sigma}^{-1}(\boldsymbol{x}-\boldsymbol{\mu})\right) \tag{2.40}$$

$$Gam(\lambda|a,b) = \frac{1}{\Gamma(a)}b^{a}\lambda^{a-1}\exp(-b\lambda) \tag{2.41}$$

where d is the dimension of a vector $\boldsymbol{x}$ and $\Gamma(\cdot)$ is the gamma function. The PDF given in Eq. 2.39 is referred as the Gaussian-gamma distribution. Here, the full-rank assumption of $\boldsymbol{X}$ is presumably satisfied as long as $n \gg mp$, i.e., as long as sufficient length of the time series is provided.

Note that the conditional expectations of the parameters relevant to the posterior PDF $p(\mathbf{w},\beta|\boldsymbol{t})$ in Eq. 2.39 are correspond to the maximum likelihoods of the parameters. That is,

$$\mathbb{E}_{\boldsymbol{w},\beta}[\boldsymbol{w}|\boldsymbol{t}] = \iint \boldsymbol{w}p(\boldsymbol{w},\beta|\boldsymbol{t})\mathrm{d}\boldsymbol{w}\mathrm{d}\beta = \int \widehat{\boldsymbol{w}}Gam\left(\beta\middle|\frac{N}{2},\frac{1}{2}E(\widehat{\boldsymbol{w}})\right)\mathrm{d}\beta = \widehat{\boldsymbol{w}} \tag{2.42}$$

$$\mathbb{E}_{\boldsymbol{w},\beta}[\beta|\boldsymbol{t}] = \iint \beta p(\boldsymbol{w},\beta|\boldsymbol{t})\mathrm{d}\boldsymbol{w}\mathrm{d}\beta = \int \beta Gam\left(\beta\middle|\frac{N}{2},\frac{1}{2}E(\widehat{\boldsymbol{w}})\right)\mathrm{d}\beta = \frac{N}{E(\widehat{\boldsymbol{w}})} = \hat{\beta}. \tag{2.43}$$

Thus, the posterior distribution led from the Jeffreys prior is compatible to the conventional maximum likelihood method. This relationship therefore justifies in adopting Bayesian statistics to extend modal analysis methods that is based on the maximum likelihood method.

The Gaussian-gamma distribution is so-called a conjugate prior for the parameters $\boldsymbol{w}$ and β [57]. That is, if the prior follows the Gaussian-gamma distribution, the posterior also follows the Gaussian-gamma distribution with different hyperparameters. For instance, let following prior distribution be assumed before obtaining data.

$$p(\boldsymbol{w},\beta) = \mathcal{N}(\boldsymbol{w}|\boldsymbol{m},(\beta\boldsymbol{L})^{-1})Gam(\beta|a,b) \tag{2.44}$$

where, $\boldsymbol{L} \in \mathbb{R}^{D\times D}$ is a symmetric and positive definite matrix, $a > 0$ and $b > 0$. The parameters $\boldsymbol{m}$, $\boldsymbol{L}$, a and b are referred as hyperparameters, which determine the form of the PDF for the parameters $\boldsymbol{w}$ and β. Then the following posterior PDF is obtained based on the Bayes' theorem (see also Appendix).

$$p(\boldsymbol{w},\beta) = \mathcal{N}(\boldsymbol{w}|\boldsymbol{m}',(\beta\boldsymbol{L}')^{-1})Gam(\beta|a',b') \tag{2.45}$$

where, $\boldsymbol{m}'$, $\boldsymbol{L}'$, a' and b' are the hyperparameters of the posterior PDF.

$$\boldsymbol{L}' = \boldsymbol{L} + \boldsymbol{X}^{\mathrm{T}}\boldsymbol{X} \tag{2.46}$$

$$\boldsymbol{m}' = \boldsymbol{L}'^{-1}(\boldsymbol{L}\boldsymbol{m} + \boldsymbol{X}^{\mathrm{T}}\boldsymbol{t}) \tag{2.47}$$

$$a' = a + \frac{N}{2} \tag{2.48}$$

$$b' = b + \frac{1}{2}\|\boldsymbol{t} - \boldsymbol{X}\boldsymbol{m}'\|^2 + \frac{1}{2}(\boldsymbol{m}' - \boldsymbol{m})^{\mathrm{T}}\boldsymbol{L}(\boldsymbol{m}' - \boldsymbol{m}) \tag{2.49}$$

Note that the prior and the posterior PDFs have same functional form. Hence, the sequential algorithm can be numerically realized by calculating hyperparameters given in Eqs. 2.46–2.49 step by step. Numerically, the posterior PDF complying with the non-informative prior is produced by substituting $[\boldsymbol{L}]_{ij} = 0 \ \ (i, j = 1 \dots mp\ \ ), a = 0$ and $b = 0$ to Eqs. 2.46–2.49. Once the posterior PDF is obtained from the non-informative prior, the posterior PDF is adoptable as the prior PDF for a newly observed data. Therefore, the sequential algorithm is easily realized by updating the hyperparameters of the posterior PDF using Eqs. 2.46–2.49 in a recursive manner whenever a newly observed dataset is available.

2.3 Models of Vibrating Structures

2.3.1 General description

According to the Newton's law, the dynamic behavior of a vibrating structure can be formulated by the proper equation of motions (EOMs). Especially for ambient vibration of a bridge, the displacement induced by the vibration is expected to be small enough. This study thus presumes that only elastic deformation occurs on the bridge and focuses on linear EOMs to describe their mechanical behavior. Finite element (FE) models are widely used to approximate the mechanical properties of the structures where the structures are divided into elements with proper material properties. Supposing mechanical system with n degree of freedom (DOF), the linear EOM for the FE model is described as following differential equation.

$$\boldsymbol{M}\ddot{\boldsymbol{z}}(t) + \boldsymbol{C}_d\dot{\boldsymbol{z}}(t) + \boldsymbol{K}\boldsymbol{z}(t) = \boldsymbol{f}(t) \tag{2.50}$$

where $\boldsymbol{M}, \boldsymbol{C}_d, \boldsymbol{K} \in \mathbb{R}^{n\times n}$ are the mass, damping and stiffness matrices. $\boldsymbol{z}(t), \boldsymbol{f}(t) \in \mathbb{R}^n$ are the displacement and external force vectors at continuous time t. The dots over $\boldsymbol{z}(t)$ denote the derivative with respect to time. The mass matrix $\boldsymbol{M}$ and stiffness matrix $\boldsymbol{K}$ are generated from the geometry and the material properties of the each element. The damping matrix $\boldsymbol{C}_d$ is employed to model the decay in the dynamic response.

The following discussion briefly describes the relationship between the FE model and the modal properties. The further discussions are given in [9], [35], [62]. Assuming that the initial displacements and velocities are zero, the time domain equation given in Eq. 2.50 is transformed into the Laplace domain [62], [63] as follows.

$$(s^2\boldsymbol{M} + s\boldsymbol{C}_d + \boldsymbol{K})Z(s) = F(s) \tag{2.51}$$

where $Z(s), F(s) \in \mathbb{R}^n$ are the Laplace transforms of $\boldsymbol{z}(t)$ and $\boldsymbol{f}(t)$, and $s \in \mathbb{C}$ denotes the frequency parameter of the Laplace domain. Accordingly, following relationship is given.

$$Z(s) = \boldsymbol{H}(s)F(s) \tag{2.52}$$

where

$$\boldsymbol{H}(s) = (s^2\boldsymbol{M} + s\boldsymbol{C}_d + \boldsymbol{K})^{-\mathbf{1}}. \tag{2.53}$$

Here, $\boldsymbol{H}(s)$ is referred as the transfer function matrix. According to the control theory, the poles of this transfer function, which are referred as the system poles, define the natural frequencies and damping ratio of the mechanical system. The system poles are equivalent to the roots of following equation.

$$|s\boldsymbol{P} + \boldsymbol{Q}| = 0 \tag{2.54}$$

where $\boldsymbol{P}, \boldsymbol{Q} \in \mathbb{R}^{2n\times 2n}$ are respectively given as

$$\boldsymbol{P} = \begin{bmatrix} \boldsymbol{C} & \boldsymbol{M} \\ \boldsymbol{M} & \boldsymbol{O} \end{bmatrix}, \tag{2.55}$$

$$\boldsymbol{Q} = \begin{bmatrix} \boldsymbol{K} & \boldsymbol{O} \\ \boldsymbol{O} & -\boldsymbol{M} \end{bmatrix}. \tag{2.56}$$

Here, $\boldsymbol{O}$ denotes zero matrix with proper size. The roots of Eq. 2.54 are given by solving the following eigenvalue problem.

$$\boldsymbol{P\Psi\Lambda} + \boldsymbol{Q\Psi} = 0 \tag{2.57}$$

where $\boldsymbol{\Psi} \in \mathbb{C}^{2n\times 2n}$ contains the $2n$ complex eigenvectors as its columns. $\boldsymbol{\Lambda} \in \mathbb{C}^{2n\times 2n}$ is a diagonal matrix containing the following eigenvalues.

$$\lambda_i, \lambda_i^* = -\xi_i\omega_i \pm j\sqrt{1-\xi_i^2}\,\omega_i \quad (i = 1, \ldots, n) \tag{2.58}$$

where the index '$*$' denotes complex conjugate, and j denotes the imaginary unit. ω_i and ξ_i are respectively angular natural frequencies and damping ratios. Letting $\mathrm{diag}[\cdot]$ denote a diagonal matrix, and letting $\boldsymbol{\Lambda} = \mathrm{diag}[\lambda_1, \lambda_2, \ldots, \lambda_n, \lambda_1^*, \lambda_2^*, \ldots, \lambda_n^*]$, the corresponding eigenvectors are given as

$$\boldsymbol{\Psi} = \begin{bmatrix} \boldsymbol{\phi}_1 & \cdots & \boldsymbol{\phi}_n & \boldsymbol{\phi}_1^* & \cdots & \boldsymbol{\phi}_n^* \\ \lambda_1\boldsymbol{\phi}_1 & \cdots & \lambda_n\boldsymbol{\phi}_n & \lambda_1^*\boldsymbol{\phi}_1^* & \cdots & \lambda_n^*\boldsymbol{\phi}_n^* \end{bmatrix} \tag{2.59}$$

where $\boldsymbol{\phi}_i \in \mathbb{C}^n$ $(i = 1, \ldots n)$ is referred as mode shape vectors, modal displacement vectors or modal vectors. According to Eq. 2.57, each of the eigenvalues and the eigenvectors satisfies following relationship.

$$\left(\lambda_i^2 \boldsymbol{M} + \lambda_i \boldsymbol{C}_d + \boldsymbol{K}\right)\boldsymbol{\phi}_i = \boldsymbol{0} \tag{2.60}$$

where $\boldsymbol{0}$ is a zero vector with a proper size.

Although the FE model provides good representation of a vibrating structure, it is not possible to measure all DOFs of the FE model in practice. The measurement in continuous time domain is not so practical either since the digital signal processing on computers requires discrete signals. Thus, most of the existing time domain modal analyses [35]–[37] are based upon the discrete state space model given in the following discussion.

2.3.2 State space model

The EOM in Eq. 2.50 and matrices in Eqs. 2.55 and 2.56 generate the following first order differential equation.

$$\dot{\boldsymbol{x}}(t) = \boldsymbol{A}_c \boldsymbol{x}(t) + \boldsymbol{B}_c \boldsymbol{f}(t) \tag{2.61}$$

where

$$\boldsymbol{x}(t) = \begin{bmatrix} \boldsymbol{q}(t) \\ \dot{\boldsymbol{q}}(t) \end{bmatrix}, \tag{2.62}$$

$$\boldsymbol{A}_c = -\boldsymbol{P}^{-1}\boldsymbol{Q} = \begin{bmatrix} \boldsymbol{O} & \boldsymbol{I} \\ -\boldsymbol{M}^{-1}\boldsymbol{K} & -\boldsymbol{M}^{-1}\boldsymbol{C}_d \end{bmatrix}, \tag{2.63}$$

$$\boldsymbol{B}_c = \boldsymbol{P}^{-1}\begin{bmatrix} \boldsymbol{I} \\ \boldsymbol{O} \end{bmatrix} = \begin{bmatrix} \boldsymbol{O} \\ \boldsymbol{M}^{-1} \end{bmatrix} \tag{2.64}$$

where $\boldsymbol{I}$ is an unit matrix with a proper size. $\boldsymbol{x}(t) \in \mathbb{R}^{2n}$ is called the state vector and Eq. 2.61 is called a state equation. Eqs. 2.57 and 2.63 show that the eigenvalue decomposition of the matrix $\boldsymbol{A}_c$ is given as

$$\boldsymbol{A}_c = \boldsymbol{\Psi}\boldsymbol{\Lambda}\boldsymbol{\Psi}^{-1}. \tag{2.65}$$

In a practical vibration experiment, the dynamic behavior of the structures are partially measured on several locations. The sensors for the measurement can be either accelerometers, velocity or displacement transducers in general. Assuming that the measurement are taken at m locations on the structure, the observation is given as following equation

$$\boldsymbol{y}(t) = \boldsymbol{C}_{acc}\ddot{\boldsymbol{z}}(t) + \boldsymbol{C}_{vel}\dot{\boldsymbol{z}}(t) + \boldsymbol{C}_{dis}\boldsymbol{z}(t) \tag{2.66}$$

where $\boldsymbol{y}(t) \in \mathbb{R}^{m}$ are the measured outputs of the system. $\boldsymbol{C}_{acc}, \boldsymbol{C}_{vel}, \boldsymbol{C}_{dis} \in \mathbb{R}^{m\times n}$ are the output location matrices for acceleration, velocity and displacement respectively. Using Eqs. 2.50 and 2.61 to eliminate $\ddot{\boldsymbol{z}}(t)$ and $\boldsymbol{x}(t)$, Eq. 2.66 can be transformed into

$$\boldsymbol{y}(t) = \boldsymbol{C}\boldsymbol{x}(t) + \boldsymbol{D}\boldsymbol{f}(t) \tag{2.67}$$

where

$$\boldsymbol{C} = [\boldsymbol{C}_{dis} - \boldsymbol{C}_{acc}\boldsymbol{M}^{-1}\boldsymbol{K} \quad \boldsymbol{C}_{vel} - \boldsymbol{C}_{acc}\boldsymbol{M}^{-1}\boldsymbol{C}_{d}], \tag{2.68}$$

$$\boldsymbol{D} = \boldsymbol{C}_{acc}\boldsymbol{M}^{-1}. \tag{2.69}$$

Eq. 2.67 is referred as an observation equation. A mathematical model noted by the state and observation equations, which are respectively shown in Eqs. 2.61 and 2.67, is referred as a state space model.

The continuous-time equations are discretized by choosing a certain fixed sampling period Δt with the discrete time instants $k \in \mathbb{N}$, where $t = k\Delta t$. Under the zero-order hold assumption [62], the state space model shown in Eqs. 2.61 and 2.67 is discretized as follows.

$$\boldsymbol{x}_{k+1}^{s} = \boldsymbol{A}\boldsymbol{x}_{k}^{s} + \boldsymbol{B}\boldsymbol{f}_{k} \tag{2.70}$$

$$\boldsymbol{y}_{k} = \boldsymbol{C}\boldsymbol{x}_{k}^{s} + \boldsymbol{D}\boldsymbol{f}_{k} \tag{2.71}$$

where $\boldsymbol{x}_{k}^{s} = \boldsymbol{x}(k\Delta t)$ is the discrete-time state vector. Similarly, $\boldsymbol{y}_{k} = \boldsymbol{y}(k\Delta t)$ and $\boldsymbol{f}_{k} = \boldsymbol{f}(k\Delta t)$. The matrices $\boldsymbol{A}$ and $\boldsymbol{B}$ in Eq. 2.70 are related to their continuous-time counterparts in Eqs. 2.63 and 2.64 as follows.

$$\boldsymbol{A} = \exp(\boldsymbol{A}_{c}\Delta t) \tag{2.72}$$

$$\boldsymbol{B} = (\boldsymbol{A} - \boldsymbol{I})\boldsymbol{A}_{c}^{-1}\boldsymbol{B}_{c} \tag{2.73}$$

The matrix $\boldsymbol{A}$ is referred as the (discrete) state matrix of the system. Eqs. 2.65 and 2.72 show that the eigenvalue decomposition of the state matrix has following relation to the system poles.

$$\boldsymbol{A} = \boldsymbol{\Psi}\exp(\boldsymbol{\Lambda}\Delta t)\boldsymbol{\Psi}^{-1} = \boldsymbol{\Psi}\boldsymbol{\Lambda}_{d}\boldsymbol{\Psi}^{-1} \tag{2.74}$$

where $\boldsymbol{\Lambda}_{d} = \exp(\boldsymbol{\Lambda}\Delta t)$ is a diagonal matrix consisting of the eigenvalues of $\boldsymbol{A}$. Thus, each of the eigenvalues of $\boldsymbol{A}$ is relevant to the natural frequencies and the damping ratios through Eq. 2.58. Letting $\tilde{\boldsymbol{x}}_{k}^{s} = \boldsymbol{\Psi}^{-1}\boldsymbol{x}_{k}^{s}$, the discretized state space model shown in Eqs. 2.70 and 2.71 is transposed as

$$\tilde{\boldsymbol{x}}_{k+1}^{s} = \boldsymbol{\Lambda}_{d}\tilde{\boldsymbol{x}}_{k}^{s} + \boldsymbol{\Psi}\boldsymbol{B}\boldsymbol{f}_{k} \tag{2.75}$$

$$\boldsymbol{y}_{k} = \boldsymbol{V}\tilde{\boldsymbol{x}}_{k}^{s} + \boldsymbol{D}\boldsymbol{f}_{k} \tag{2.76}$$

where $\boldsymbol{V} = \boldsymbol{C}\boldsymbol{\Psi}$ is referred as modal output matrix that is essential to identify mode shapes using the operational modal analyses. Hereafter, assume that $\boldsymbol{y}(t) = \boldsymbol{C}_{acc}\ddot{\boldsymbol{z}}(t)$ for simplicity, i.e., only acceleration are measured at m locations on the structure. The Eqs. 2.59, 2.60 and 2.68 accordingly generate modal output matrix as

$$\boldsymbol{V} = -\boldsymbol{C}_{acc}[\boldsymbol{M}^{-1}\boldsymbol{K} \quad \boldsymbol{M}^{-1}\boldsymbol{C}_d]\boldsymbol{\Psi} = \boldsymbol{C}_{acc}[\lambda_1^2\boldsymbol{\phi}_1 \quad \cdots \quad \lambda_n^2\boldsymbol{\phi}_n \quad \lambda_1^{*2}\boldsymbol{\phi}_1^* \quad \cdots \quad \lambda_n^{*2}\boldsymbol{\phi}_n^*] \tag{2.77}$$

Since the system poles λ_i appearing in Eq. 2.77 are just alter the scale of each column, Eq. 2.77 shows that each of the columns of the modal output matrix $\boldsymbol{V}$ denotes the part of the mode shape vectors $\boldsymbol{\phi}_i$ that can be observed from data. In practice, it is difficult to identify geometry constructing the FE model merely from observed output data. Thus, the columns of the $\boldsymbol{V}$ are usually regarded as the observed mode shapes instead of $\boldsymbol{\phi}_i$ in Eq. 2.59 for the operational modal analyses.

The interest for this thesis is ambient vibration based modal analysis and damage detection as mentioned in Section 1.2, and thus the external force $\boldsymbol{f}_k$ are supposed to be not measured. The following stochastic state space model approximately substitutes the deterministic formulation of the state space model given in Eqs. 2.70 and 2.71.

$$\boldsymbol{x}_{k+1}^s = \boldsymbol{A}\boldsymbol{x}_k^s + \boldsymbol{w}_k \tag{2.78}$$

$$\boldsymbol{y}_k = \boldsymbol{C}\boldsymbol{x}_k^s + \boldsymbol{v}_k \tag{2.79}$$

where $\boldsymbol{w}_k \in \mathbb{R}^n$ and $\boldsymbol{v}_k \in \mathbb{R}^m$ are zero-mean white noise vectors. The external force is implicitly modelled by the noise terms. Although this white noise assumption sometimes does not provide proper representation of the external force, the assumption is necessary for the system identification [9]. When the with noise assumption is violated, for instance external force contains some dominant frequency components, these frequency components cannot be separated from the natural frequencies of the system and they will appear as spurious poles of the state matrix $\boldsymbol{A}$ (see also Chapter 4).

An alternative model for stochastic systems is more suitable for some application, which is so-called forward innovation model. It is obtained by applying the steady-state Kalman filter to the stochastic state-space model as follows.

$$\boldsymbol{x}_{k+1}^f = \boldsymbol{A}\boldsymbol{x}_k^f + \boldsymbol{K}_g\boldsymbol{e}_k \tag{2.80}$$

$$\boldsymbol{y}_k = \boldsymbol{C}\boldsymbol{x}_k^f + \boldsymbol{e}_k \tag{2.81}$$

where the elements of the sequence $\boldsymbol{e}_k$ is called innovations, which also can be interpreted as the prediction errors of the Kalman filter. $\boldsymbol{x}_k^f$ is the state vector of the forward innovation model. The matrix $\boldsymbol{K}_g$ is so-called forward Kalman gain, which can be alternatively transformed from the covariance matrices of the noise vectors $\boldsymbol{w}_k$ and $\boldsymbol{v}_k$ [47].

2.3.3 Autoregressive models

The state vector is eliminated from the forward innovation state-space model to the following autoregressive moving average (ARMA) model.

$$\boldsymbol{y}_k = \boldsymbol{\alpha}_1 \boldsymbol{y}_{k-1} + \cdots + \boldsymbol{\alpha}_p \boldsymbol{y}_{k-p} + \boldsymbol{e}_k + \boldsymbol{\gamma}_1 \boldsymbol{e}_{k-1} + \cdots + \boldsymbol{\gamma}_p \boldsymbol{e}_{p-1} \tag{2.82}$$

where $\boldsymbol{\alpha}_i, \boldsymbol{\gamma}_i \in \mathbb{R}^{m\times m}$ $(i = 1, \dots, p)$ are respectively AR coefficient matrices and moving average coefficient matrices, and p is the AR order. The AR coefficients are obtained by solving following linear system of equations for $\boldsymbol{\alpha}_i$ [64].

$$\begin{bmatrix}\boldsymbol{\alpha}_p & \boldsymbol{\alpha}_{p-1} \dots & \boldsymbol{\alpha}_1\end{bmatrix}\boldsymbol{\Gamma}_p = \boldsymbol{C}\boldsymbol{A}^p \tag{2.83}$$

where $\boldsymbol{\Gamma}_p \in \mathbb{R}^{mp\times 2n}$ is so-called observability matrix defined as

$$\boldsymbol{\Gamma}_p = \begin{bmatrix} \boldsymbol{C} \\ \boldsymbol{CA} \\ \vdots \\ \boldsymbol{CA}^{p-1} \end{bmatrix} \tag{2.84}$$

If the system is observable [62], i.e. $\mathrm{rank}(\boldsymbol{\Gamma}_p) = 2n$, the AR coefficients are uniquely determined by Eq. 2.83. The moving average coefficients also can be determined by the following equation.

$$\begin{bmatrix}\boldsymbol{\gamma}_p & \boldsymbol{\gamma}_{p-1} \cdots \boldsymbol{\gamma}_1 & \boldsymbol{I}\end{bmatrix} = \begin{bmatrix}-\boldsymbol{\alpha}_p & -\boldsymbol{\alpha}_{p-1} \dots & -\boldsymbol{\alpha}_1 & \boldsymbol{I}\end{bmatrix}\begin{bmatrix} \boldsymbol{I} & \boldsymbol{O} & \cdots & \boldsymbol{O} \\ \boldsymbol{CK}_g & \boldsymbol{I} & \cdots & \boldsymbol{O} \\ \vdots & \vdots & \ddots & \vdots \\ \boldsymbol{CA}^{p-1}\boldsymbol{K}_g & \boldsymbol{CA}^{p-2}\boldsymbol{K}_g & \cdots & \boldsymbol{I} \end{bmatrix} \tag{2.85}$$

Assuming $mp = 2n$, the similarity transformation for the state matrix $\boldsymbol{A}$ using $\boldsymbol{\Gamma}_p$ is produces following relationship

$$\acute{\boldsymbol{A}} = \boldsymbol{\Gamma}_p \boldsymbol{A} \boldsymbol{\Gamma}_p^{-1} = \begin{bmatrix} \boldsymbol{O} & \boldsymbol{I} & \cdots & \boldsymbol{O} \\ \vdots & \vdots & \ddots & \vdots \\ \boldsymbol{O} & \boldsymbol{O} & \cdots & \boldsymbol{I} \\ \boldsymbol{\alpha}_p & \boldsymbol{\alpha}_{p-1} & \cdots & \boldsymbol{\alpha}_1 \end{bmatrix} \tag{2.86}$$

Since $\boldsymbol{C}\boldsymbol{\Gamma}_p^{-1} = [\boldsymbol{I}\ \ \boldsymbol{O} \dots \boldsymbol{O}]$, the forward innovation state-space model is transformed as

$$\acute{\boldsymbol{x}}_{k+1}^f = \acute{\boldsymbol{A}}\acute{\boldsymbol{x}}_k^f + \boldsymbol{\Gamma}_p \boldsymbol{K}_g \boldsymbol{e}_k \tag{2.87}$$

$$\boldsymbol{y}_k = [\boldsymbol{I}\ \ \boldsymbol{O} \dots \boldsymbol{O}]\acute{\boldsymbol{x}}_k^f + \boldsymbol{e}_k \tag{2.88}$$

where $\acute{\boldsymbol{x}}_k^f = \boldsymbol{\Gamma}_p \boldsymbol{x}_k^f$. Since the eigenvalues are invariant under similarity transformation, the system poles and mode shapes can be identified by the eigenvalue decomposition of $\acute{\boldsymbol{A}}$**.** Therefore, the p-th order ARMA model is a good representation of a vibrating structure with pm modes assuming the white noise excitation.

AR models are defined as ARMA model without moving average part, namely, as the following form.

$$\boldsymbol{y}_k = \boldsymbol{\alpha}_1 \boldsymbol{y}_{k-1} + \cdots + \boldsymbol{\alpha}_p \boldsymbol{y}_{k-p} + \boldsymbol{e}_k \tag{2.89}$$

The modal properties are identified from eigenvalue decomposition of $\acute{\boldsymbol{A}}$ as well as ARMA models (see also Section 3.2.1). Although the AR model is not merely equivalent to the ARMA model, He and De Roeck [36] showed that the finite order ARMA model can be approximated by a high order AR model. Note that the AR coefficients are easily estimated by means of the least square problems since the AR model can be regarded as one of the linear regressive model mentioned in Section 2.2.3. The prompt estimation method for the AR coefficients motivated the use of AR models in system identification of vibrating structures. This thesis mainly adopts the AR model to realize prompt damage detection method. The application for the damage detection is stated in Chapter 5 and Chapter 6.

Chapter 3

Operational Modal Analysis

3.1 Introduction

This chapter reviews several existing modal analysis methods aiming at vibration based damage detection of bridges under traffic. As mentioned in Section 1.1.2, most of existing studies have adopted operational modal analysis methods for vibration-based bridge health monitoring. Advantages and disadvantages of the operational modal analysis are summarized as follows [35]:

Advantages:

- During operational modal analysis, the structure remains in its operational conditions. Thus, the mechanical properties in actual loading condition is to be obtained.
- Operational modal analysis does not require the use of any artificial excitation devices to excite bridges since it makes use of the naturally available excitation.
- Thanks to the natural presence of the ambient excitation, operational modal analysis is suited for use in continuous monitoring of systems.

Disadvantages:

- Operational modal analysis assumes that the input signal is a white noise sequence. A violation of this assumption yield extra spurious poles in identified mechanical system.
- In some cases, the overall level of the ambient excitation can be quite low. Thus, resulting data will be noisy and the estimated modal parameters will be uncertain.

The operational modal analysis methods are roughly divided into time domain analyses and frequency domain analyses [35], [62]. The time-domain analyses directly utilize time series data to identify the modal properties. The frequency domain analyses, on the other hand, utilize data transformed into the frequency domain. In practice, the fast Fourier transform (FFT) is widely adopted to obtain the frequency domain representation of the original time series. Since this thesis investigates a damage indicator directly observed from time series of acceleration, time domain analyses are mainly investigated in following discussions. Additionally, to investigate feasibility of Bayesian statistics, the operational modal analysis adopting Bayesian inference is also introduced.

The parametric models given in Section 2.3 provide the foundation of time domain modal analysis methods. To establish a concise damage detection using time series of acceleration, one of the simplest time-domain analysis called Yule-Walker (YW) method is firstly reviewed. To make advanced discussion involved in feature extraction, data-driven stochastic subspace identification (SSI) which provides a powerful tool for noise reduction is secondly reviewed. To investigate the validity of the Bayesian approach, a frequency domain Bayesian modal analysis method that is called Bayesian operational modal analysis (BAYOMA) thirdly reviewed. Each of the time domain modal analysis methods provides a case study utilizing the experimental data given in Section 1.4. For the BAYOMA, a case study will be given in Chapter 4.

3.2 Methodologies

3.2.1 Yule-Walker method

Let $\boldsymbol{y}_k \in \mathbb{R}^m$ denote a column vector of the discrete time series of measured acceleration data whose components respectively correspond to m measurement locations. The time series obtained from a linear structural system excited by white noise can be approximately modeled as an autoregressive (AR) model of sufficient model order p as

$$\boldsymbol{y}_k = \sum_{i=1}^{p} \boldsymbol{\alpha}_i \boldsymbol{y}_{k-i} + \boldsymbol{e}_k \tag{3.1}$$

where $\boldsymbol{\alpha}_i$ denotes the i-th AR coefficient matrix and $\boldsymbol{e}_k$ denotes a white noise vector as described in Section 2.2.3. The autoregressive moving average (ARMA) model, which is relevant to the state space model, is asymptotically equivalent to the AR model in Eq. 3.1 as $p \to \infty$ [36]. Thus, the AR model with a higher AR order generates approximated estimators of the modal properties. This high order assumption however means that the AR model produces many numerical poles to obtain reasonable modal properties as discussed later.

The autocorrelation matrices of the measured data $\boldsymbol{y}_k$ are defined as $\boldsymbol{R}(s) = \mathrm{Cov}[\boldsymbol{y}_k, \boldsymbol{y}_{k-s}] \in \mathbb{R}^{m\times m}$. Because of the white noise assumption, $\mathrm{Cov}[\boldsymbol{e}_k, \boldsymbol{y}_{k-s}] = \boldsymbol{O}$ is satisfied for $s > 0$. Thus, multiplying $(\boldsymbol{y}_{k-s})^{\mathrm{T}}$ from right in Eq. 3.1, and taking the expectation, the following relationships called Yule–Walker equation is obtained.

$$\boldsymbol{R}(s) = \sum_{i=1}^{p} \boldsymbol{\alpha}_i \boldsymbol{R}(-i) + \boldsymbol{W} \quad (s = 0) \tag{3.2}$$

$$\boldsymbol{R}(s) = \sum_{i=1}^{p} \boldsymbol{\alpha}_i \boldsymbol{R}(s-i) \quad (s = 1, 2, \dots) \tag{3.3}$$

where, $\boldsymbol{W} \in \mathbb{R}^{m\times m}$ is a covariance matrix defined as $\boldsymbol{W} = \mathrm{Cov}[\boldsymbol{e}_k]$. From a measured time series of finite data length N, autocorrelation matrices are estimated as follows.

$$\hat{\boldsymbol{R}}(s) = \frac{1}{N}\sum_{k=s}^{N} \boldsymbol{y}_k \boldsymbol{y}_{k-s}{}^{\mathrm{T}} \quad (s = 0,1,\cdots) \tag{3.4}$$

$$\hat{\boldsymbol{R}}(s) = \hat{\boldsymbol{R}}(-s)^{\mathrm{T}} \qquad (s < 0). \tag{3.5}$$

Existing studies [48], [50], [65] provides a least square estimation method with simultaneous equations for $s = 0,1,\cdots,s_{\max}$ in Eq. 3.3. Here, $s_{\max}$ is defined empirically. To avoid an arbitrary decision, this thesis merely adopts the simplest case such that $s_{\max} = p$. For that case, Eq. 3.3 can be summarized as the following equations using the autocorrelation matrices in Eqs. 3.4 and 3.5.

$$[\boldsymbol{\alpha}_1 \;\; \boldsymbol{\alpha}_2 \ldots \boldsymbol{\alpha}_p]\boldsymbol{T} = [\hat{\boldsymbol{R}}(1) \;\; \hat{\boldsymbol{R}}(2) \ldots \hat{\boldsymbol{R}}(p)] \tag{3.6}$$

$$\boldsymbol{T} = \begin{bmatrix} \hat{\boldsymbol{R}}(0) & \hat{\boldsymbol{R}}(1) & \cdots & \hat{\boldsymbol{R}}(p-1) \\ \hat{\boldsymbol{R}}(-1) & \hat{\boldsymbol{R}}(0) & \cdots & \hat{\boldsymbol{R}}(p-2) \\ \vdots & \vdots & \ddots & \vdots \\ \hat{\boldsymbol{R}}(1-p) & \hat{\boldsymbol{R}}(2-p) & \cdots & \hat{\boldsymbol{R}}(0) \end{bmatrix}. \tag{3.7}$$

The AR coefficient matrices $\boldsymbol{\alpha}_i$ are accordingly estimated from an actually measured time series by solving Eq. 3.6. Assuming that $\boldsymbol{y}_k = 0$ is satisfied for $k < 0$, the estimators of the AR coefficients resulting from Eq. 3.6 correspond to the most likelihoods mentioned in Section 2.2.3. The estimated autocorrelation matrices given in Eqs. 3.4 and 3.5 provide the positive definite matrix $\boldsymbol{T}$ for which the inverse matrix is assured to exist. Note that $\hat{\boldsymbol{R}}(s)$ in Eq. 3.4 is a biased estimator, i.e., the expectation of $\hat{\boldsymbol{R}}(s)$ is biased from the true value of $\boldsymbol{R}(s)$ since the term $\sum_{k=s}^{N} \boldsymbol{y}_k \boldsymbol{y}_{k-s}{}^{\mathrm{T}}$ is divided by N instead of $(N - s + 1)$. This biased estimators ensure that the matrix $\boldsymbol{T}$ is positive definite if sufficient length of the data satisfying $N \gg p$ is obtained, and thus the AR coefficient matrices are uniquely determined only from the observed time series and the predefined AR order p. That is why the biased autocorrelation matrices are adopted as the estimators.

As mentioned in Section 2.2.3, the system poles of the transfer function are obtainable by solving the eigenvalue problem represented by the following characteristic equation with respect to z.

$$|\boldsymbol{I}z - \acute{\boldsymbol{A}}| = 0 \tag{3.8}$$

$$\acute{\boldsymbol{A}} = \begin{bmatrix} \boldsymbol{O} & \boldsymbol{I} & \cdots & \boldsymbol{O} \\ \vdots & \vdots & \ddots & \vdots \\ \boldsymbol{O} & \boldsymbol{O} & \cdots & \boldsymbol{I} \\ \boldsymbol{\alpha}_p & \boldsymbol{\alpha}_{p-1} & \cdots & \boldsymbol{\alpha}_1 \end{bmatrix}. \tag{3.9}$$

Since the roots of Eq. 3.8 correspond to eigenvalues of $\acute{\boldsymbol{A}}$, the system poles are determined through following eigenvalue decomposition.

$$\acute{\boldsymbol{A}} = \acute{\boldsymbol{\Psi}}\boldsymbol{\Lambda}_d\acute{\boldsymbol{\Psi}}^{-1}. \tag{3.10}$$

where $\boldsymbol{\Lambda}_d \in \mathbb{C}^{mp \times mp}$ is a diagonal matrix consisting of the eigenvalues and $\acute{\boldsymbol{\Psi}} \in \mathbb{C}^{mp \times mp}$ is a matrix containing the relevant eigenvectors as its columns. According to Eqs. 2.58 and 2.74, the modal properties and the eigenvalues have the following relationship.

$$\lambda_i^{\mathrm{d}}, \lambda_i^{\mathrm{d}*} = \exp\left[\left(-\xi_i \omega_i \pm \jmath \sqrt{1-\xi_i^2}\omega_i\right)\Delta t\right] \tag{3.11}$$

where λ_i^{d} and $\lambda_i^{\mathrm{d}*}$ are the conjugate pairs of the eigenvalues contained in the matrix $\boldsymbol{\Lambda}_d$. ω_i and ξ_i denote respectively angular natural frequencies and damping ratios as mentioned in Section 2.2.3. Therefore, the ω_i and ξ_i are estimated as follows.

$$\omega_i = \frac{\mathrm{abs}(\ln \lambda_i^{\mathrm{d}})}{\Delta t} \tag{3.12}$$

$$\xi_i = -\cos(\mathrm{angle}(\ln \lambda_i^{\mathrm{d}})) \tag{3.13}$$

where $\mathrm{abs}(\cdot)$, $\mathrm{angle}(\cdot)$ and $\cos(\cdot)$ respectively denote an absolute value, a phase angle and its cosine. According to Eqs. 2.74 and 2.86, $\acute{\boldsymbol{\Psi}} = \boldsymbol{\Gamma}_p \boldsymbol{\Psi}$ is satisfied where $\boldsymbol{\Gamma}_p$ is the observability matrix defined in Eq. 2.84. Thus, the following modal output matrix is estimated.

$$\boldsymbol{V} = [\boldsymbol{I} \quad \boldsymbol{O} \quad \cdots \quad \boldsymbol{O}]\acute{\boldsymbol{\Psi}} \in \mathbb{C}^{m \times mp}. \tag{3.14}$$

That is, the modal output matrix $\boldsymbol{V}$ is given as the submatrix consisting of the first m rows of $\acute{\boldsymbol{\Psi}}$. Each column of $\boldsymbol{V}$ is the estimated mode shape that corresponds to each of the eigenvalues contained in the $\boldsymbol{\Lambda}_d$. According to the above discussion, the AR model of p order produces estimators of modal properties for at most $mp/2$ DOF mechanical system.

3.2.2 Stochastic subspace identification

The YW method mentioned in Section 3.2.1 has simple estimation process for modal identification. However, the asymptotical assumption requires sufficiently higher AR order p in the analysis, and thus the estimators of modal properties contain spurious results. The data-driven SSI [47] enables reduction of the DOF of the system model to a reasonable one. This procedure is called model reduction.

The SSI generates estimators of the system matrices $\boldsymbol{A}$, $\boldsymbol{C}$ and the Kalman gain $\boldsymbol{K}_g$ in the following forward innovation model.

$$\boldsymbol{x}_{k+1}^f = \boldsymbol{A}\boldsymbol{x}_k^f + \boldsymbol{K}_g \boldsymbol{e}_k \tag{3.15}$$

$$\boldsymbol{y}_k = \boldsymbol{C}\boldsymbol{x}_k^f + \boldsymbol{e}_k \tag{3.16}$$

System matrices $\boldsymbol{A}$ and $\boldsymbol{C}$, which can be converted to the modal properties, are estimated by means of least-squares method that minimizes prediction errors of the state vector $\boldsymbol{x}_k^f$ produced by the forward Kalman filter.

The algorithm for the SSI is described briefly as follows: Firstly, the projection matrix $\boldsymbol{O}_p$ is generated as

$$\boldsymbol{O}_p = \mathbf{Y}_\mathrm{f}\mathbf{Y}_\mathrm{p}^\mathrm{T}\left(\mathbf{Y}_\mathrm{p}\mathbf{Y}_\mathrm{p}^\mathrm{T}\right)^\dagger\mathbf{Y}_\mathrm{p}. \tag{3.17}$$

Therein, $\mathbf{Y}_\mathrm{f}$ and $\mathbf{Y}_\mathrm{p}$, which respectively represent the block Hankel matrices of the future and past outputs, are defined as follows.

$$\mathbf{Y}_\mathrm{p} = \begin{bmatrix} \boldsymbol{y}_0 & \boldsymbol{y}_1 & \cdots & \boldsymbol{y}_{N'-1} \\ \cdots & \cdots & \cdots & \cdots \\ \boldsymbol{y}_{p-2} & \boldsymbol{y}_{p-1} & \cdots & \boldsymbol{y}_{p+N'-3} \\ \boldsymbol{y}_{p-1} & \boldsymbol{y}_p & \cdots & \boldsymbol{y}_{p+N'-2} \end{bmatrix} \in \mathbb{R}^{mp\times N'} \tag{3.18}$$

$$\mathbf{Y}_\mathrm{f} = \begin{bmatrix} \boldsymbol{y}_p & \boldsymbol{y}_{p+1} & \cdots & \boldsymbol{y}_{p+N'-1} \\ \cdots & \cdots & \cdots & \cdots \\ \boldsymbol{y}_{2p-2} & \boldsymbol{y}_{2p-1} & \cdots & \boldsymbol{y}_{2p+N'-3} \\ \boldsymbol{y}_{2p-1} & \boldsymbol{y}_{2p} & \cdots & \boldsymbol{y}_{2p+N'-2} \end{bmatrix} \in \mathbb{R}^{mp\times N'}. \tag{3.19}$$

Here, N' is determined as $N' = N - 2p + 1$, and p is a predefined parameter determining the size of the Hankel matrix. Similarly, the following projection matrix is also defined.

$$\boldsymbol{O}_{p-1} = \mathbf{Y}_\mathrm{f}^-\mathbf{Y}_\mathrm{p}^{+\mathrm{T}}\left(\mathbf{Y}_\mathrm{p}^+\mathbf{Y}_\mathrm{p}^{+\mathrm{T}}\right)^\dagger\mathbf{Y}_\mathrm{p}^+ \tag{3.20}$$

where $\mathbf{Y}_\mathrm{p}^+$ and $\mathbf{Y}_\mathrm{f}^-$ are respectively defined as

$$\mathbf{Y}_\mathrm{p}^+ = \begin{bmatrix} \boldsymbol{y}_0 & \boldsymbol{y}_1 & \cdots & \boldsymbol{y}_{N'-1} \\ \cdots & \cdots & \cdots & \cdots \\ \boldsymbol{y}_{p-1} & \boldsymbol{y}_p & \cdots & \boldsymbol{y}_{p+N'-2} \\ \boldsymbol{y}_p & \boldsymbol{y}_{p+1} & \cdots & \boldsymbol{y}_{p+N'-1} \end{bmatrix} \in \mathbb{R}^{m(p+1)\times N'} \tag{3.21}$$

$$\mathbf{Y}_\mathrm{f}^- = \begin{bmatrix} \boldsymbol{y}_{p+1} & \boldsymbol{y}_{p+2} & \cdots & \boldsymbol{y}_{p+N'} \\ \cdots & \cdots & \cdots & \cdots \\ \boldsymbol{y}_{2p-2} & \boldsymbol{y}_{2p-1} & \cdots & \boldsymbol{y}_{2p+N'-3} \\ \boldsymbol{y}_{2p-1} & \boldsymbol{y}_{2p} & \cdots & \boldsymbol{y}_{2p+N'-2} \end{bmatrix} \in \mathbb{R}^{m(p-1)\times N'}. \tag{3.22}$$

The singular value decomposition (SVD) is then applied to factorize $\boldsymbol{O}_p$ as

$$\boldsymbol{W}_1\boldsymbol{O}_p\boldsymbol{W}_2 = \mathbf{USV}^\mathbf{T} = (\mathbf{U_1U_2})\begin{pmatrix} \mathbf{S_1} & \mathbf{0} \\ \mathbf{0} & \mathbf{S_2} \end{pmatrix}(\mathbf{V_1V_2})^\mathbf{T} \simeq \mathbf{U_1S_1V_1^T} \tag{3.23}$$

where $\boldsymbol{W}_1$ and $\boldsymbol{W}_2$ are user-defined weighting matrices such that $\boldsymbol{W}_1$ is full rank and $\boldsymbol{W}_2$ obeys $\mathrm{rank}(\mathbf{Y}_\mathrm{p}) = \mathrm{rank}(\mathbf{Y}_\mathrm{p}\boldsymbol{W}_2)$. For simplicity, the SSI discussed in this thesis only adopts unit matrices as those weighting matrices. In that case, the SSI algorithm is also referred as unweighted principal component analysis [47], [66]. $\mathbf{U}$ and $\mathbf{V}$ are unitary matrices with an appropriate size; $\mathbf{S}$ is a diagonal matrix with non-negative real elements. Diagonal elements of $\mathbf{S}$ are referred as singular values of $\boldsymbol{O}_p$. Supposing that those singular values in $\mathbf{S}$ are listed in descending order, the projection matrix is approximately reproduced by the dominant singular values and the corresponding vectors as $\mathbf{U_1 S_1 V_1^T}$. Components in $\mathbf{U_2 S_2 V_2^T}$ are regarded as trivial components and ignored in the estimation. The optimal state sequence $\mathbf{X}_p = [\boldsymbol{x}_p^f \quad \boldsymbol{x}_{p+1}^f \quad \cdots \quad \boldsymbol{x}_{p+N'-1}^f]$ predicted by the Kalman filter in a least-squares sense. The observability matrix $\boldsymbol{\Gamma}_p$ and optimal state sequence $\mathbf{X}_p$ are respectively obtained as shown below [47].

$$\boldsymbol{\Gamma}_p = \mathbf{U_1 S_1^{1/2}} \tag{3.24}$$

$$\mathbf{X}_p = \mathbf{S_1^{1/2} V_1^T} \tag{3.25}$$

Here, the significant components in the state sequence are extracted by applying SVD to $\boldsymbol{O}_p$. The one-step-ahead state sequence $\mathbf{X}_{p+1} = [\boldsymbol{x}_{p+1}^f \quad \boldsymbol{x}_{p+2}^f \quad \cdots \quad \boldsymbol{x}_{p+N'}^f]$ is estimated as

$$\mathbf{X}_{p+1} = \boldsymbol{\Gamma}_{p-1}^{\dagger} \boldsymbol{O}_{p-1} \tag{3.26}$$

where $\boldsymbol{\Gamma}_{p-1}$ is obtained as $\boldsymbol{\Gamma}_p$ without last m rows according to the definition of the observability matrix given in Eq. 2.86. Consequently, Eqs. 3.15 and 3.16 generate the least square estimators of the system matrices $\boldsymbol{A}$ and $\boldsymbol{C}$ as

$$\boldsymbol{A} = \mathbf{X}_{p+1} \mathbf{X}_p^{\dagger} \tag{3.27}$$

$$\boldsymbol{C} = \mathbf{Y} \mathbf{X}_p^{\dagger} \tag{3.28}$$

where $\mathbf{Y} = [\boldsymbol{y}_p \quad \boldsymbol{y}_{p+1} \quad \cdots \quad \boldsymbol{y}_{p+N'-1}]$ is observed time series relevant to the state space. Note that the dimension of the state vector $\boldsymbol{x}_k^f$ is reduced by means of the SVD. The number of the system poles thus corresponds to the number of the singular values consisting the matrix $\mathbf{S_1}$ in Eq. 3.23. Therefore, the significant modal response of the bridge is presumably extracted from the measured acceleration using the SVD. The modal properties are identified from the system matrices $\boldsymbol{A}$ and $\boldsymbol{C}$ by means of the eigenvalue analysis as well as the YW method.

3.2.3 Bayesian operational modal analysis

The Bayesian inference method for modal identification is formulated by Yuen and Katafygiotis in both of the time and frequency domain [42], [43], [67]. Au [44]–[46] proposed a fast computation algorithm to solve those Bayesian inference problem, which is called BAYOMA in this thesis. Hereafter, brief introduction of the BAYOMA is provided.

The BAYOMA is based on the following modal model in time domain.

$$\boldsymbol{y}_j = \sum_{i=1}^{r} \boldsymbol{\phi}_i \ddot{\eta}_i(t_j) + \boldsymbol{\epsilon}_j \tag{3.29}$$

where, $\boldsymbol{\epsilon}_j \in R^m$ is the measurement noise in j-th discreet time step, $t_j = j\Delta t$ is the relevant time, $\boldsymbol{\phi}_i$ is the i-th mode vector, and r is the number of modes composing the modal response. The measurement noise $\boldsymbol{\epsilon}_j$ is modeled as a white noise vector. $\eta_i(t)$ is the modal displacement that satisfies following relationship.

$$\ddot{\eta}_i(t) + 2\xi_i\omega_i\dot{\eta}_i(t) + \omega_i^2\eta_i(t) = p_i(t) \tag{3.30}$$

where $p_i(t)$ is the modal force corresponding to the i-th mode. Note that Eq. 3.30 is easily generated from the equation of motion in Eq. 2.50 assuming the proportional damping [35].

For computational convenience, the following FFT is adopted as an observed dataset for the Bayesian inference.

$$F_k = \sqrt{\frac{2\Delta t}{N}} \sum_{j=1}^{N} \boldsymbol{y}_j \exp\left[-\frac{2\pi\mathfrak{j}(k-1)(j-1)}{N}\right]. \tag{3.31}$$

F_k is the FFT relevant to the frequency $\mathrm{f}_k = (k-1)/N\Delta t$. Accordingly, Eq. 3.29 can be transformed into the frequency domain as

$$F_k = \sum_{i=1}^{m} \boldsymbol{\phi}_i \ddot{\eta}'_{ik} + \boldsymbol{\epsilon}'_k \tag{3.32}$$

where $\ddot{\eta}'_{ik}$ and $\boldsymbol{\epsilon}'_k$ are respectively the FFTs of $\ddot{\eta}_i(t_j)$ and $\boldsymbol{\epsilon}_j$ relevant to the frequency f_k. Similarly, Eq. 3.30 is transformed as

$$\ddot{\eta}'_{ik} = -h_{ik}p'_{ik} \tag{3.33}$$

$$h_{ik} = \left[(\beta_{ik}^2 - 1) + \mathfrak{j}(2\xi_i\beta_{ik})\right]^{-1} \tag{3.34}$$

where p'_{ik} is the FFT of $p_i(t_j)$, h_{ik} is the transfer function in frequency domain relevant to the i-th mode, and β_{ik} is defined as $\beta_{ik} = \omega_i/2\pi\mathrm{f}_k$.

To formulate the likelihood function for the Bayesian inference, the following vectors consisting of the real and imaginal parts of the FFTs are introduced.

$$\boldsymbol{Z}_k = \begin{bmatrix} \mathrm{Re}\ F_k \\ \mathrm{Im}\ F_k \end{bmatrix} \in \mathbb{R}^{2m} \tag{3.35}$$

where Re and Im respectively denote the real and imaginary part of a complex matrix. If the sufficient length of the data is available, the vectors $\boldsymbol{Z}_k$ are formulated as Gaussian vectors whose covariance matrices are given as follows [43].

$$\mathrm{Cov}[\boldsymbol{Z}_k] = \mathbf{C}_k = \frac{1}{2}\begin{bmatrix} \boldsymbol{\Phi}\mathrm{Re}\ \mathbf{H}_k\boldsymbol{\Phi}^{\mathrm{T}} & -\boldsymbol{\Phi}\mathrm{Im}\ \mathbf{H}_k\boldsymbol{\Phi}^{\mathrm{T}} \\ \boldsymbol{\Phi}\mathrm{Im}\ \mathbf{H}_k\boldsymbol{\Phi}^{\mathrm{T}} & \boldsymbol{\Phi}\mathrm{Re}\ \mathbf{H}_k\boldsymbol{\Phi}^{\mathrm{T}} \end{bmatrix} - \frac{S_e}{2}\boldsymbol{I} \tag{3.36}$$

where $\boldsymbol{\Phi} = [\boldsymbol{\phi}_1, \boldsymbol{\phi}_2, \dots, \boldsymbol{\phi}_r] \in \mathbb{R}^{n\times r}$ is a matrix consisting of the modal vectors and S_e is the power spectrum density (PSD) of the $\boldsymbol{\epsilon}_j$. Note that S_e is a constant because of the white noise assumption. $\mathbf{H}_k$ is the PSD matrix generated from Eq. 3.33 as

$$\mathbf{H}_k = \mathrm{diag}[h_{1k},\ h_{2k}, \dots, h_{rk}]\ \mathbf{S}\ \mathrm{diag}[h_{1k}^*,\ h_{2k}^*, \dots, h_{rk}^*] \tag{3.37}$$

where $\mathbf{S} \in \mathbb{C}^{r\times r}$ is the PSD matrix of the modal forces $p_i(t_j)$ $(i = 1, \dots, r)$, which are also assumed as white noise. The above discussion shows that the covariance matrix $\mathbf{C}_k$ is a function of the modal properties $\omega_i,\ \xi_i\ , \boldsymbol{\phi}_i$ $(i = 1, \dots r)$ and the PSD constants $\mathbf{S}$ and S_e. Therefore, the likelihood function for the parameters $\boldsymbol{\theta} = \{\omega_i, \xi_i, \boldsymbol{\phi}_i, \mathbf{S}, S_e | i = 1, \dots r\}$ is given as the following conditional PDF for $\boldsymbol{Z}_k$.

$$p(\{\boldsymbol{Z}_k\}|\boldsymbol{\theta}) = (2\pi)^{-mN}\exp[-L(\boldsymbol{\theta})] \tag{3.38}$$

$$L(\boldsymbol{\theta}) = \frac{1}{2}\sum_k \ln|\mathbf{C}_k(\boldsymbol{\theta})| + \frac{1}{2}\sum_k \boldsymbol{Z}_k^T\mathbf{C}_k(\boldsymbol{\theta})^{-1}\boldsymbol{Z}_k \tag{3.39}$$

where $\{\boldsymbol{Z}_k\}$ represents the dataset consisting of available data vectors $\boldsymbol{Z}_k$. $L(\boldsymbol{\theta})$ is the negative log likelihood function of $\boldsymbol{\theta}$. Assuming the uniform prior distribution, the posterior distribution is proportional to the likelihood function as

$$p(\boldsymbol{\theta}|\{\boldsymbol{Z}_k\}) \propto \exp[-L(\boldsymbol{\theta})]. \tag{3.40}$$

Thus, the most provable value of the posterior distribution function $p(\boldsymbol{\theta}|\{\boldsymbol{Z}_k\})$ is produced as the most likelihood function that is minimize $L(\boldsymbol{\theta})$.

Letting $\widehat{\boldsymbol{\theta}}$ denotes the most provable value minimizing $L(\boldsymbol{\theta})$, the negative log likelihood function is approximate to the following form by the Taylor expansion [45].

$$L(\boldsymbol{\theta}) \approx L(\widehat{\boldsymbol{\theta}}) + \frac{1}{2}(\boldsymbol{\theta} - \widehat{\boldsymbol{\theta}})^T\widehat{H}_L(\boldsymbol{\theta} - \widehat{\boldsymbol{\theta}}). \tag{3.41}$$

where $\widehat{H}_L$ is the Hessian matrix of $L(\theta)$ at $\widehat{\boldsymbol{\theta}}$. Accordingly the posterior distribution approximately satisfies

$$p(\boldsymbol{\theta}|\{\boldsymbol{Z}_k\}) \propto \exp\left[-\frac{1}{2}(\boldsymbol{\theta} - \widehat{\boldsymbol{\theta}})^T\widehat{H}_L(\boldsymbol{\theta} - \widehat{\boldsymbol{\theta}})\right]. \tag{3.42}$$

That is the posterior distribution $p(\boldsymbol{\theta}|\{\boldsymbol{Z}_k\})$ is approximated to the Gaussian distribution with the expectation $\widehat{\boldsymbol{\theta}}$ and the covariance matrix $\widehat{H}_L^{-1}$.

The most probable value $\widehat{\boldsymbol{\theta}}$ is obtained by numerical optimization for minimizing the negative log likelihood function $L(\boldsymbol{\theta})$ because of its nonlinearity. The computational procedure for the numerical optimization is given in [44]. To avoid complexity in the computational process, frequency band of the FFT need to be limited. The BAYOMA therefore requires preliminary analysis to find the frequency band to be analyzed in advance to the modal analysis [46], [68]. This problem is discussed in Chapter 4.

3.3 Case Studies

Although the methodologies cited in Section 3.2 enable to estimate the mechanical system model generating the dynamic responses, the estimators contain spurious system poles derived from the violation of the white noise assumption. The following two problems have to be settled for modal identification:

- Which is the suitable size of the model to describe the bridge vibration?
- Which poles are physically meaningful in the estimated model?

The first problem is so-called model selection problem [57]. For instance in the AR model, the AR order *p* should be predefined for the estimation. For the model selection problems, information criteria possibly provide scales for the goodness of the models. The second problem is one of feature extraction problem. That is, the modal properties of the structure are to be extracted from numerical estimators of the system poles. The stabilization diagrams [35] is one of the widely used methods to distinguish the physically meaningful poles.

Hereafter the model selection and feature extraction problems are investigated for the time domain operational analysis methods, namely, YW method and SSI. Let the ten samples of the time series in INT40 scenario given in Section 1.4 be investigated for this case study.

3.3.1 Model selection

This section adopts two widely used information criteria, namely, Akaike information criterion (AIC) and Bayesian information criterion (BIC). Firstly, feasibility of information criteria is examined for the AR model. The AIC scales goodness of a model according to a Kullback-Leibler divergence between the estimated model and an unknown real model [69]. Generally, the AIC is formulated as

$$\mathrm{AIC} = -2\ln p\left(\mathcal{D}\middle|\widehat{\boldsymbol{\theta}}\right) + 2M \tag{3.43}$$

where $\mathcal{D}$ is the observed dataset and $\ln p(\mathcal{D}|\boldsymbol{\theta})$ is the log likelihood function mentioned in

Section 2.2.3. $\widehat{\boldsymbol{\theta}}$ is the most likelihood estimator of the parameter $\boldsymbol{\theta}$ that maximizes the likelihood function. M is the number of the variable parameters contained in the parametric model. The likelihood term $-2\ln p(\mathcal{D}|\widehat{\boldsymbol{\theta}})$ in Eq. 3.43 evaluates the fitting performance of the model, and the term $2M$ is regarded as a penalty term to avoid adopting complicated model leading to overfitting. Thus, the lower AIC presumably produces the better model to generate the observed dataset $\mathcal{D}$. Assuming the Gaussian white noise for the AR model, the likelihood function is given as

$$\ln p(\{\boldsymbol{y}_k\}|\boldsymbol{\alpha}_1, \dots, \boldsymbol{\alpha}_p, \boldsymbol{\Sigma}) = \sum_{k=1}^{N} \ln \mathcal{N}(\boldsymbol{y}_k | \sum_{\boldsymbol{i=1}}^{\boldsymbol{p}} \boldsymbol{\alpha}_i \boldsymbol{y}_{k-i}, \boldsymbol{\Sigma}) \tag{3.44}$$

where $\boldsymbol{\Sigma} = \mathrm{Cov}[\boldsymbol{e}_k]$. The most likelihoods of the AR coefficients are approximately obtained by the YW method. Accordingly, the maximized log likelihood function is given as

$$\ln p(\{\boldsymbol{y}_k\}|\widehat{\boldsymbol{\alpha}}_1, \dots, \widehat{\boldsymbol{\alpha}}_p, \widehat{\boldsymbol{\Sigma}}) = -\frac{N}{2}(m \ln 2\pi + \ln|\widehat{\boldsymbol{\Sigma}}_{AR}| + m) \tag{3.45}$$

where $\widehat{\boldsymbol{\Sigma}}_{AR}$ is the most likelihood of the covariance matrix of $\boldsymbol{e}_k$ estimated as follows.

$$\widehat{\boldsymbol{\Sigma}}_{AR} = \widehat{\boldsymbol{R}}(0) - \sum_{\boldsymbol{i=1}}^{\boldsymbol{p}} \widehat{\boldsymbol{\alpha}}_i \widehat{\boldsymbol{R}}(-i) \tag{3.46}$$

The variable parameters in the AR model are given as the components of $\boldsymbol{\alpha}_1, \dots, \boldsymbol{\alpha}_p, \boldsymbol{\Sigma}$. Note that $\boldsymbol{\Sigma}$ is a symmetry positive definite matrix, and thus $m(m+1)/2$ parameters are variable in the matrix $\boldsymbol{\Sigma}$. Accordingly, the AIC for the AR model is given as

$$\mathrm{AIC} = N(m \ln 2\pi + \ln|\widehat{\boldsymbol{\Sigma}}_{AR}| + m) + 2m^2 p + m(m+1) \tag{3.47}$$

The BIC is derived from the model evidence approximated as follows [57].

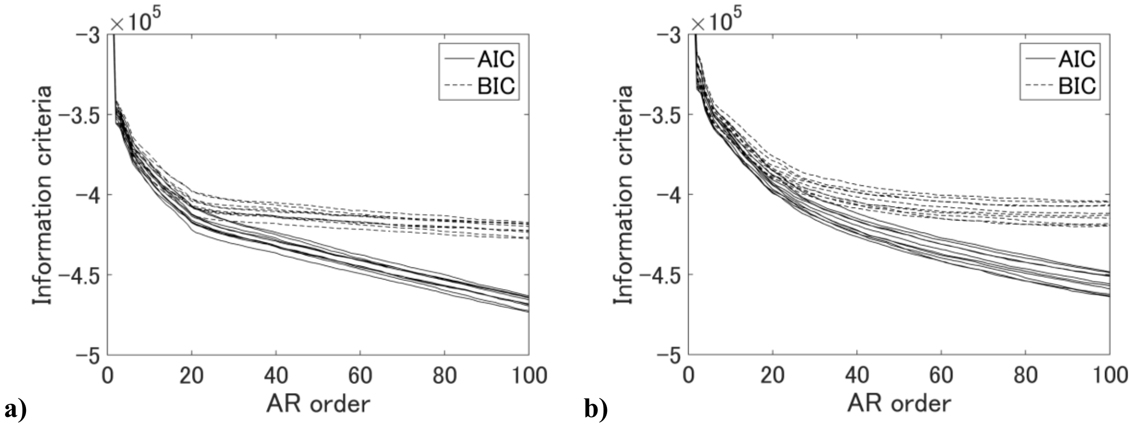

Figure 3.1 Information criteria for the AR models with respect to the model orders: a) for WV data; b) for FV data

$$p(\mathcal{D}) = \int p(\mathcal{D}|\boldsymbol{\theta})p(\boldsymbol{\theta})\mathrm{d}\boldsymbol{\theta} \approx p(\mathcal{D}|\widehat{\boldsymbol{\theta}}) - \frac{1}{2}M\ln N \tag{3.48}$$

where $p(\boldsymbol{\theta})$ represents a broad prior. The model evidence produces the marginalized likelihood of the model. According to Eq. 3.48, BIC is generally formulated as

$$\mathrm{BIC} = -2\ln p(\mathcal{D}|\widehat{\boldsymbol{\theta}}) + M\ln N. \tag{3.49}$$

Thus, the BIC for the AR model is given as

$$\mathrm{BIC} = N\left(m\ln 2\pi + \ln\left|\widehat{\boldsymbol{\Sigma}}_{AR}\right| + m\right) + \left(m^2 p + \frac{1}{2}m(m+1)\right)\ln N. \tag{3.50}$$

In Figure 3.1, the AIC and BIC for the AR model is evaluated with respect to the AR order p. The solid and dashed lines in Figure 3.1 respectively show the AIC and BIC relevant to the 10 samples of the vehicle loading tests contained in INT40. Both of the information criteria do not converge when p is lower than 100. That is possibly because the higher order AR models asymptotically approximate the mechanical system as mentioned in Section 2.3.3. Those results show the higher order AR models give the better models to minimize the measurement errors. However, the higher order AR models produce the more spurious poles, and thus the lower order AR model is actually reasonable to describe vibrating bridge as discussed later. Because of the difference in the penalty terms, the slopes of the BIC tend to be smoother than the slopes of the AIC. Each of the slopes of the BIC in Figure 3.1 gets smoother as the AR order increases. That is, for the higher order AR model, the increase of the AR order is less informative than the lower order AR model. For instance, the slopes of the BIC in Figure 3.1a show that the AR coefficients with AR order lower than 20 are more informative than the coefficients with order higher than 20. Similarly, the slopes in Figure 3.1b show the models with order lower than 40 is informative.

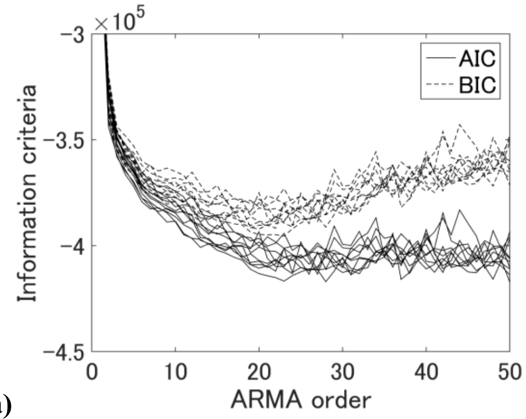

a)

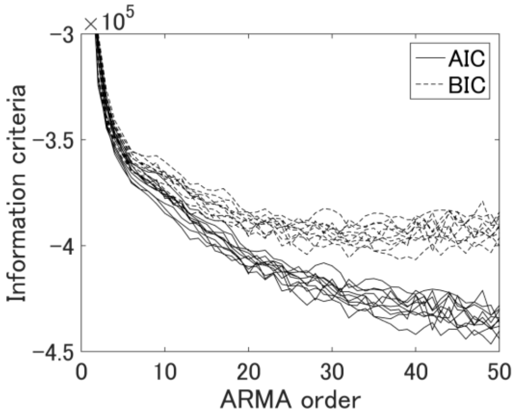

b)

Figure 3.2 Information criteria for the ARMA models with respect to the model orders: a) for WV data; b) for FV data.

The information criteria for the state space model is also evaluated for the SSI without model reduction. As mentioned in Section 2.3.3, the forward-innovation state space model for SSI is relevant to the ARMA model of p order. Note that the ARMA order corresponds to the predefined size of the Hankel matrix of the SSI. Since the variable parameters in the ARMA model appear in the ARMA coefficients and the covariance matrix of $\boldsymbol{e}_k$, the AIC and BIC for the ARMA model is given as

$$\mathrm{AIC} = N'\left(m \ln 2\pi + \ln\left|\widehat{\boldsymbol{\Sigma}}_{ARMA}\right| + m\right) + 4m^2 p + m(m+1) \tag{3.51}$$

$$\mathrm{BIC} = N'\left(m \ln 2\pi + \ln\left|\widehat{\boldsymbol{\Sigma}}_{ARMA}\right| + m\right) + \left(2m^2 p + \frac{1}{2}m(m+1)\right)\ln N'. \tag{3.52}$$

where $\widehat{\boldsymbol{\Sigma}}_{ARMA}$ is a covariance matrix of $\boldsymbol{e}_k$ estimated in the ARMA model, which is determined by using the estimators of the state space model as follows.

$$\widehat{\boldsymbol{\Sigma}}_{ARMA} = \frac{1}{N'}\left(\mathbf{Y} - \boldsymbol{C}\mathbf{X}_p\right)\left(\mathbf{Y} - \boldsymbol{C}\mathbf{X}_p\right)^{\mathrm{T}}. \tag{3.53}$$

Figure 3.2 shows the information criteria for the ARMA model as well as Figure 3.1. The BICs in Figure 3.2a provide the optimal values of the ARMA order around 20. That is, the ARMA model with 20 order is the most reliable according to BIC. Apparently, the AICs in Figure 3.2a are converged as the ARMA order are higher than 20. This observation shows the ARMA models with higher than 20 order are less informative. Similarly, the BIC in Figure 3.2b shows the optimal values around 30 and 40 order.

The results given in Figure 3.2 are relevant to Figure 3.1 where the informative AR orders are 20 and 40 respectively for the WV data and FV data. The AR models with higher order approximate the moving average terms rather than the autoregressive terms appearing in the ARMA models. Since the modal properties are estimated from the AR coefficients, the AR models with 20 and 40 order are enough to estimate the modal properties. The above observations also demonstrate the BIC is more suitable than the AIC to find informative model order to describe vibrating bridge in practice because of its strict penalty term. That is, a reasonable choice of the AR order is possibly observed from the slope of the BIC curves for the AR models. The minimum value of BIC for the ARMA models produces the optimal size of the Hankel matrix for the SSI.

3.3.2 Feature extraction

Here, feature extraction using stabilization diagram is examined for one sample chosen from INT 40 scenario at first for simplicity. The stabilization diagram is known as a scatter diagram depicting estimated natural frequencies with respect to the model order of the linear system model. For instance, the natural frequencies relevant to the system poles estimated by the YW method are depicted as dots in the scatter diagram, where the horizontal axis represents the estimated natural frequencies and the vertical axis represents the AR order. A physically meaningful modes yield similar natural frequencies even if the model order is over-specified. Therefore, the meaningful modes display a nearly vertical line in the stabilization diagram. Furthermore, stability criteria with respectively predefined thresholds for the natural frequencies, damping ratio, and mode shapes are usually adopted to assist the feature extraction procedure [35]. This study considers the following stability criteria to extract stable modes.

$$f_{p+\kappa} - f_{th} < f_p < f_{p+\kappa} + f_{th} \tag{3.54}$$

$$\xi_{p+\kappa} - \xi_{th} < \xi_p < \xi_{p+\kappa} + \xi_{th} \tag{3.55}$$

$$MAC_{th} < \mathrm{MAC}(\boldsymbol{\phi}_p, \boldsymbol{\phi}_{p+\kappa}) \tag{3.56}$$

$$(\kappa = -\kappa_{th}, \dots, -1, 1, \dots, \kappa_{th})$$

In those expressions, $f_p, \xi_p, \boldsymbol{\phi}_p$ respectively denote the estimated natural frequency, damping ratio, and modal shape with model order p. $\mathrm{MAC}(\boldsymbol{\phi}_p, \boldsymbol{\phi}_{p+\kappa})$ stands for the modal assurance criterion (MAC) value between modal shapes $\boldsymbol{\phi}_p$ and $\boldsymbol{\phi}_{p+\kappa}$, which is defined as

$$\mathrm{MAC}(\boldsymbol{\phi}_p, \boldsymbol{\phi}_{p+\kappa}) = \frac{\left\|\boldsymbol{\phi}_p^T \boldsymbol{\phi}_{p+\kappa}\right\|^2}{\|\boldsymbol{\phi}_p\| \|\boldsymbol{\phi}_{p+\kappa}\|}. \tag{3.57}$$

Parameters f_{th}, $\xi_{th,}$ MAC_{th} in Eqs. 3.54–3.56 are thresholds for the tolerable range of the modal properties; κ_{th} is the range of model order to evaluate the inequalities.

Figure 3.3 shows the stabilization diagram for the AR model estimated by the YW method respectively for the WV data and FV data. The black dots in those diagrams represent the system poles estimated by the YW method. The red circles describe the stable poles extracted by the stability criteria given as Eqs. 3.54–3.56, where, the thresholds are respectively predefined as $f_{th} = 0.05$Hz, $\xi_{th,} = 0.5\%$, $MAC_{th} = 95\%$ and $\kappa_{th} = 3$. As shown in Figure 3.3, stabilization diagram promptly enables to find the physically meaningful mode among numerous estimated poles. Note that whether the poles are extracted or not relies on the stability criteria. Thus, the thresholds should be modified manually referring the results appearing in the diagram.

The dashed vertical lines in Figure 3.3 show the identified natural frequencies as the stable poles. Apparently, the poles relevant to the natural frequencies distributed as AR order are over 20. This observation is possibly relevant to the results given in Figure 3.1. That is, the AR coefficients below the 20 order are essential to represent the observed acceleration. Since the ARMA models relevant to the actual mechanical systems are asymptotically approximated by the higher order AR models as mentioned in Section 2.3.3, the stable poles tend to appear in the AR model with model order over 20. The higher order AR models however tend to produce spurious poles since the higher DOF is assumed for the system model. In the stabilization diagrams given in Figure 3.3a, four natural frequencies are identified, namely, 3.0 Hz, 6.9 Hz, 9.6 Hz, and 10.5 Hz. Additionally the fifth natural frequency is given as 13.4 Hz in Figure 3.3b. More stable poles appear to be observed in FV data than the WV data. This observation is discussed later.

The stabilization diagram can be also defined for the SSI. The SSI requires SVD in its computational processes, and thus it is reasonable to adopt the singular value order of the SVD as the vertical axis of the stabilization diagram. In advance of operating the SSI, the size of the Hankel matrix should be predefined. This study adopted *p*=20 and *p*=40 respectively for the WV and FV data according to the information criteria shown in Figure 3.2 to ensure that informative regressive models are provided before the model reduction by the SVD. Figure 3.4 shows the stabilization diagrams for the SSI obtained from the same

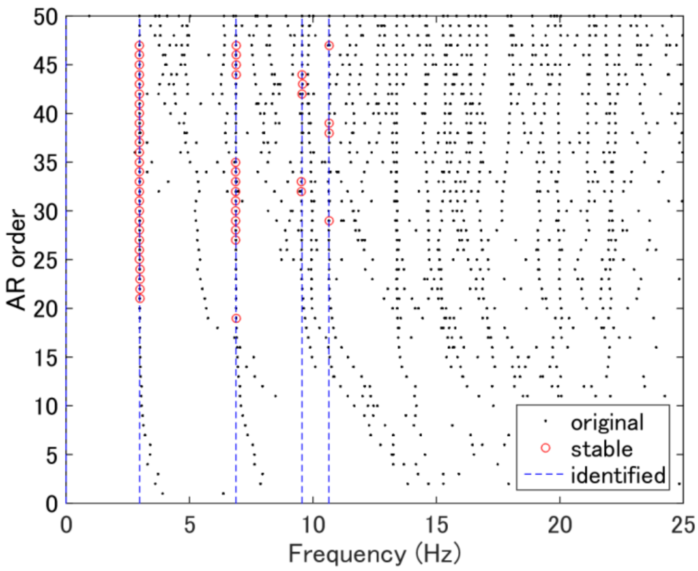

a)

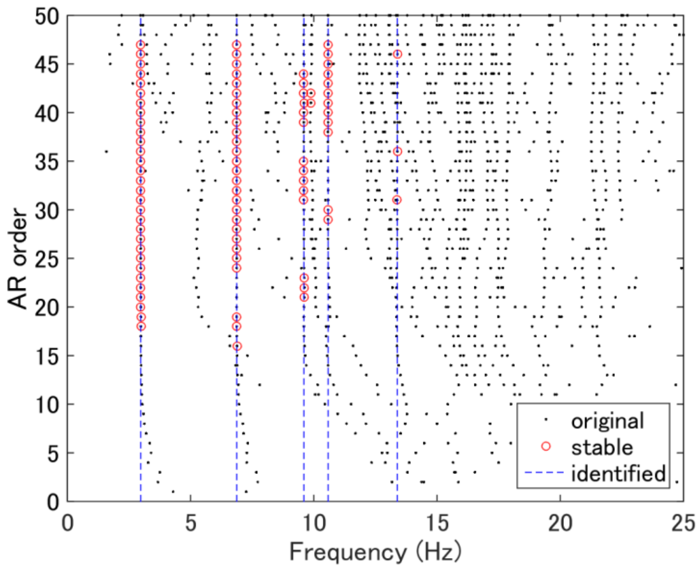

b)

Figure 3.3 Exsample of stabilization diagram for the AR models:

a) For WV data; b) For FV data

time series used in Figure 3.3. The thresholds for the stability criteria are not altered from the ones used in Figure 3.3 for comparison. In Figure 3.4, the five natural frequencies are stably extracted from both of the WV and FV data. The FV data also shows stable results for the SSI as well as the YW method. Figure 3.4b describes even higher modes are observed in a frequency range over 15 Hz. The stabilization diagrams in Figure 3.4 shows that the SVD operated in the SSI analysis enables plausible feature extraction.

In fact, the natural frequencies are not always identified by the stabilization diagrams even though

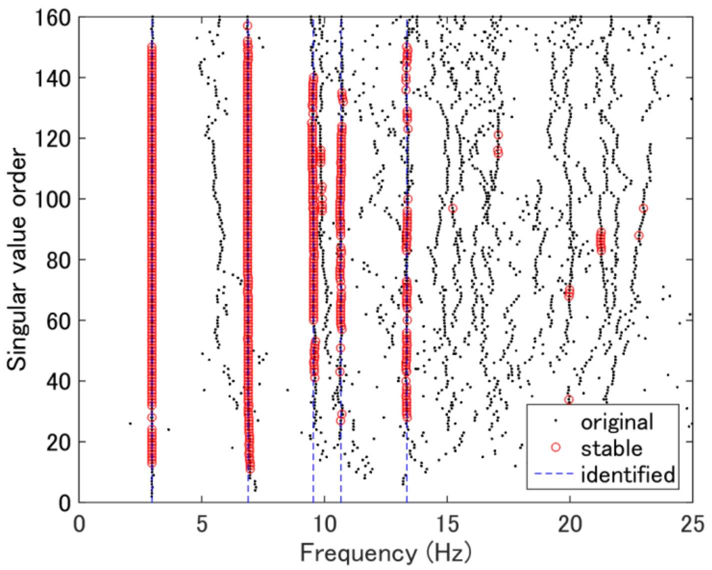

a)

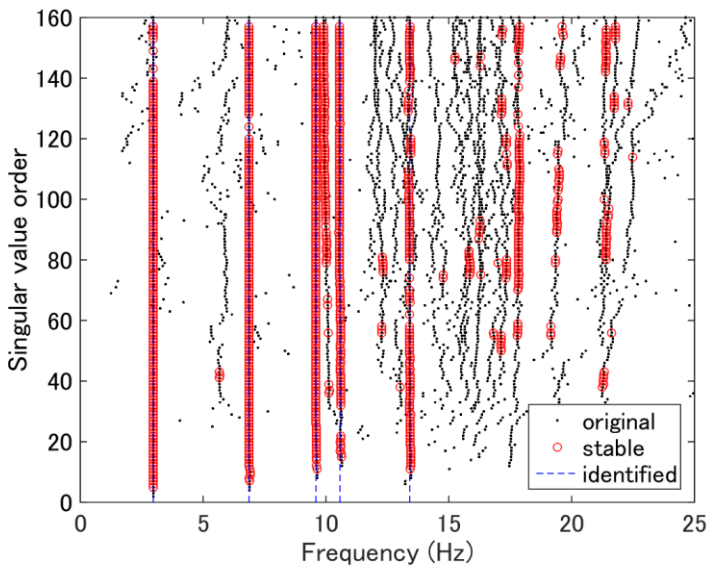

b)

Figure 3.4 Stabilization diagram for the SSI with respect to the singular value orders: a) For WV data; b) For FV data

proper critical values are predefined for the stability criteria. That is because uncertain vibration of the bridges possibly violates the mathematical assumptions. Table 3.1 shows the numbers of the correctly extracted poles by means of the stabilization diagrams for the ten samples observed as the INT40 scenario. Therein the 1st to 5th modes represent the identified modes shown as the vertical dashed lines in Figure 3.3 andFigure 3.4. For both of the YW method and SSI, the FV data provides better results. That is because the free vibration is more suitable for modal identification in general since unexpected external force is less affected from the vehicle loading [50], [51]. This observation also corresponds to the results of the power spectrum densities shown in Figure 1.5, where the more significant peaks are observed for the FV data than for the WV data because of the low noise level. For the 1st, 2nd and 3rd modes, both of the YW method and SSI show stable results since the low order modes are dominantly exited in general. On the

Table 3.1 Numbers of the correctly extracted poles.

Methods	Inputs	Modes (Frequency)				
		1st (3.0Hz)	2nd (6.9 Hz)	3rd (9.6 Hz)	4th (10.5 Hz)	5th (13.4 Hz)
YW method	WV data	10/10	9/10	9/10	7/10	2/10
	FV data	10/10	10/10	10/10	9/10	4/10
SSI	WV data	10/10	9/10	9/10	9/10	9/10
	FV data	10/10	10/10	10/10	10/10	10/10

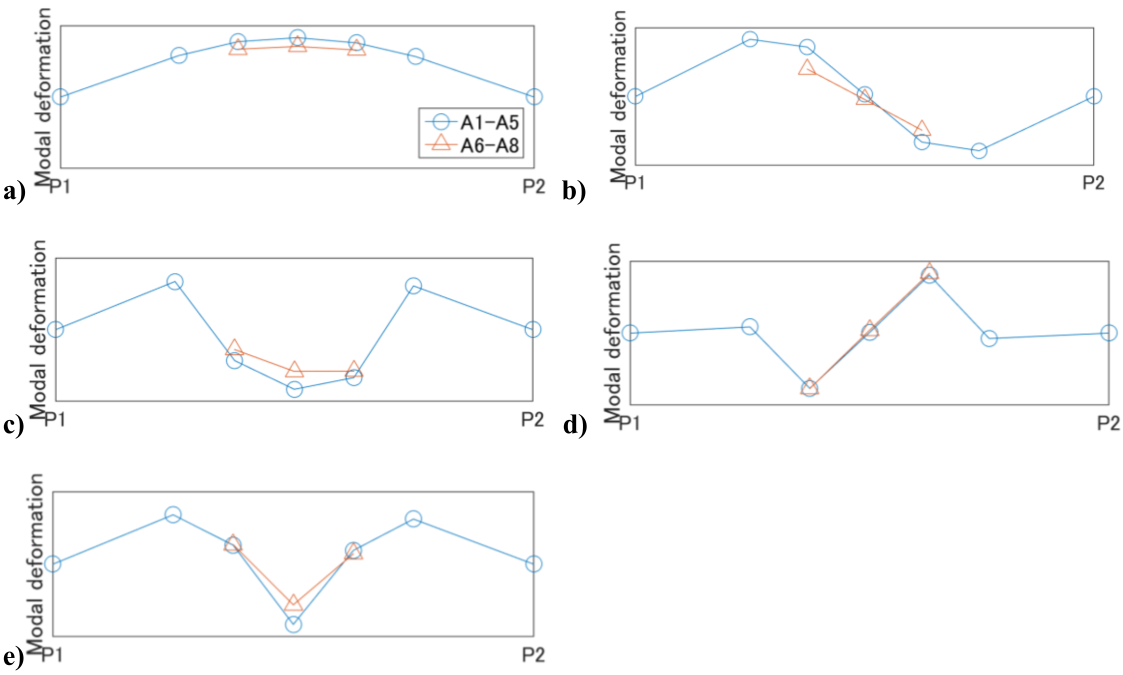

Figure 3.5 Mode shapes identified from SSI: a) 1st; b) 2nd; c) 3rd; d) 4th; e) 5th

other hand, the SSI shows better results for the 4th and 5th modes than the YW method. Thus, the SSI appears more suitable to find modal properties of the higher modes avoiding the spurious poles. That is, the model reduction procedure by SVD stably enables feature extraction for the higher modes.

Although the stabilization diagram enables to extract plausible modal properties, those results do not always ensure that the extracted properties actually describe the mechanical characteristics of the bridge. That is because the spurious poles are possibly involved in the extracted poles by the stability criteria in spite of the properly predefined thresholds. Fundamental knowledge based upon structural dynamics is required to obtain reliable results. For instance, a finite element (FE) model enables to estimate modal properties beforehand, based on proper assumptions about the mass, stiffness, boundary condition and geometry of the structure. Numerically, eigenvalue analysis on the FE model promptly provides the estimated modal properties even for structures with complicated geometry. For experimental aspect, the reliable modal identification is realized by examining the experimentally estimated mode shapes. Note that only the multi-point measurement enables to estimate the mode shape in operational modal analysis. The five mode shapes identified by the SSI for the FV data are listed in Figure 3.5 for instance. Therein, the A1 to A8 in the diagrams represent the measurement locations shown in Figure 1.3c. P1 and P2 represent the locations of the bridge piers shown in Figure 1.3b. The lateral axis shows longitudinal location where the sensors are equipped. The curves in those diagrams are depicted by connecting the estimated values of the mode vectors. Apparently, those diagrams schematically describes bending modal deformations. Those observations demonstrate that the extracted modal properties represent the mechanical characteristics of the actual bridge.

3.4 Summary

This chapter reviewed modal analysis methods for the discussions in the following chapters. Two well-known time domain modal analysis methods, namely Yule-Walker (YW) method and stochastic subspace identification (SSI), were introduced. For advanced investigation given in Chapter 4, frequency domain analysis method which is so-called Bayesian operational modal analysis is promptly introduced. Brief case studies for the YW method and the SSI are provided for the target bridge mentioned in Section 1.4.

Information criteria, which is widely used for model selection, are examined for the regressive time domain models through the case study. For AR model, slope of the Bayesian information criteria (BIC) promptly demonstrates informative model order. However, it is difficult to find a reasonable AR model only from the information criteria since the mathematical assumptions mentioned in Chapter 2 require excessively high order AR models to describe bridge vibrations. For SSI, the information criteria appears useful to find suitable size of the Hankel matrix before the model reduction.

The stabilization diagram provides feature extraction procedure to identify the physically meaningful poles. For the dominant bending modes, namely the 1st, 2nd, and 3rd modes are stably extracted by both of the YW method and SSI. On the other hand, for the higher modes, namely the 4th and 5th bending modes, the SSI produced more stable results than the YW method. This observation demonstrates that the singular value decomposition given in the SSI enables model reduction to extract the physically meaningful modes especially for the higher modes. Thus, for precise modal identification for the higher modes, the SSI is more helpful than the YW method. For the identification of the dominant modes, the YW method is still useful in practice because of its prompt numerical procedure.

Especially for precise modal identification including the higher modes, the procedure for operational modal identification in time domain is summarized as the following three steps:

Model selection: According to the information criteria, determine the size of the Hankel matrix for the SSI.

Feature extraction: Estimate system poles for several singular value orders, and then extract stable modal properties by observing a stabilization diagram.

Validation: Observe the extracted modal properties and verify their physical meanings. The estimated mode shapes will be helpful to examine their validity.

The above three-step modal identification procedure is applied again in Chapter 4. This procedure also provides further application for damage detection, which is mentioned in Chapter 6.

Chapter 4

Modal Analysis of a Cable-Stayed Bridge

4.1 Introduction

Aiming at preparation for the damage detection mentioned in Chapter 5 and Chapter 6, this chapter introduces an applicative case study. Hereafter, the uncertainty involved in mode identification of a multi-span cable-stayed bridge is investigated through a benchmark study. Especially, efficacy of the feature extraction utilizing stochastic subspace identification (SSI) and Bayesian operational modal analysis (BAYOMA) mentioned in Chapter 3 are investigated.

Among many applications used for real bridge monitoring, Ni et al. [53] reported that the modal shape of the second mode (deficient mode) of a cable-stayed bridge named Ting Kau Bridge is not identifiable under weak wind conditions, although it can be identified clearly under typhoon conditions. The second mode was also observed in a FE model analysis. Prof. Y.Q. Ni of Hong Kong Polytechnic University has proposed a benchmark study in which bridge vibration data under different find conditions were offered. Investigations were conducted to assess the mode identifiability of operational modal analysis methods.

This study was conducted to investigate the mode identifiability of a cable-stayed bridge, particularly addressing its linear system model. On Ting Kau Bridge, the Yule-Walker method mentioned in Section 3.2.1 is not applicable to this investigation because the number of the measurement locations are higher and the disturbance from uncertain ambient effects is severer than the case study given in Section 3.3. This chapter thus utilizes the SSI and BAYOMA to investigate the mode identifiability. For SSI, stabilization diagrams and cumulative contribution ratios (CCRs) [49] are particularly addressed. The use of CCRs enables to describe how much information is included in each singular value. This study adopts CCR to investigate the quantity of modal information included in the identified linear system model. For BAYOMA, the signal to noise ratio and posterior distributions for the modal properties are particularly examined to assess uncertainty involved in modal identification.

4.2 Target Bridge and Benchmark Data

Ting Kau Bridge is a three-tower cable-stayed bridge with two main spans of 448 m and 475 m, respectively, and two side spans of 127 m each as presented in Figure 4.1 [53], [70]. The bridge deck is separated respectively into two carriageways with a width of 18.8 m each. Between them are three slender single-leg towers with heights of 170 m, 194 m, and 158 m. Each carriageway comprises two longitudinal steel girders along the deck edges with steel cross girders at 4.5 m intervals, with a concrete slab on top. The two carriageways and their intervening 5.2 m gap are linked at 13.5 m intervals by connecting cross girders. The deck is supported by 384 stay cables in four cable planes. As part of a long-term health monitoring system devised by the Hong Kong Special Administrative Region Government Highways Department, more than 230 sensors were installed permanently on the Ting Kau Bridge after completing bridge construction in 1999 [71]. The detailed information about the sensor deployment and monitoring is available in [72]–[74].

The layout of the sensors at eight deck sections on Ting Kau Bridge is presented in Figure 4.2. In each section, two accelerometers were installed on the east side and the west side of the longitudinal steel girders respectively to measure the vertical acceleration. One accelerometer was installed on the central cross girder to measure the transverse acceleration. The sampling frequency of accelerometers was 25.6 Hz. Data acquired by the accelerometers deployed on the bridge deck are considered in the benchmark study.

This study investigates 10 samples given in the Benchmark study. Table 4.1 presents the time duration and wind conditions of the benchmark data. Data from Sample 1 to Sample 6 were measured under weak

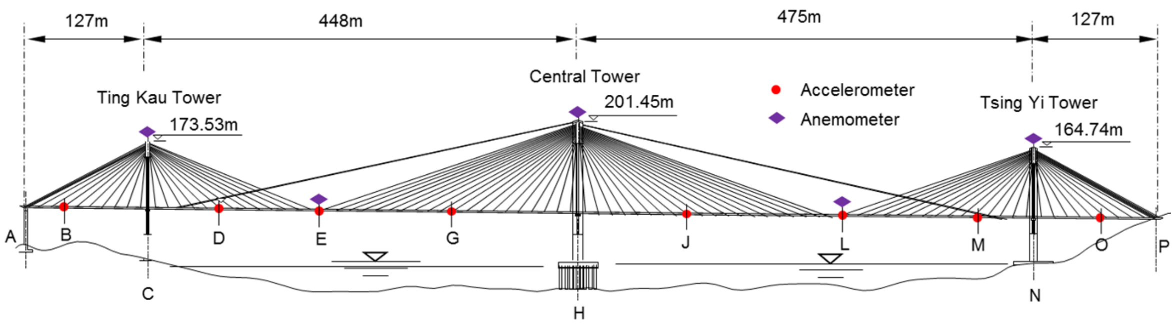

Figure 4.1 Deployment of Accelerometers and Anemometers on Ting Kau Bridge [53].

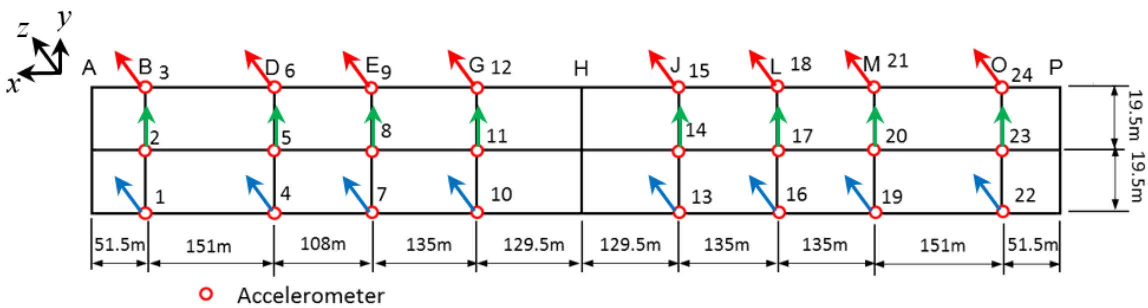

Figure 4.2 Geometry configuration of accelerometers on the bridge deck [53].

Table 4.1 Benchmark data.

Sample	Time duration	Mean hourly wind speed (m/s)	Remarks
Sample 1	15:00–16:00, 28 Dec. 1999	2.00	
Sample 2	15:00–16:00, 18 Feb. 1999	3.40	
Sample 3	15:00–16:00, 01 Mar. 1999	3.34	
Sample 4	15:00–16:00, 21 June 1999	3.41	
Sample 5	15:00–16:00, 24 July 1999	6.17	
Sample 6	15:00–16:00, 12 Aug. 1999	4.20	
Sample 7	03:00–04:00, 07 June 1999	12.11	Typhoon: Maggie
Sample 8	02:00–03:00, 23 Aug. 1999	15.62	Typhoon: Sam
Sample 9	06:00–07:00, 16 Sep. 1999	21.72	Typhoon: York
Sample 10	15:00–16:00, 16 Sep. 1999	15.91	Typhoon: York

wind conditions. Data from Sample 7 to Sample 10 were measured under typhoon conditions. Traffic was blocked during the typhoons.

4.3 Preliminary Analysis

4.3.1 Stochastic subspace identification

As discussed in [53], the frequency range of interest of Ting Kau Bridge is below 0.5 Hz. A concern related to modal identification below 0.5 Hz is that higher-frequency information interferes with it because of the white noise assumption mentioned in Section 2.3.2. To avoid the effects of high-frequency vibration to the time domain data, this study thus adopts a decimation filter [75] and each of the time series was down-sampled by following procedure: Firstly, the lowpass Chebyshev type1 infinite impulse response filter of order 8 [76] was used with cut-off frequency 0.924 Hz and passband ripple 0.05 dB. Secondly, the time series were resampled by every 20-th point from the interior of the filtered signal.

For quantitative evaluation of the optimal size of the block Hankel matrix, this study considered the Akaike information criterion (AIC). The AICs of each system model estimated from the time series of Sample 1 to Sample 10 are presented in Figure 4.3 with respect to the block Hankel matrix size, in which the optimal model order providing the best estimation of each measurement is marked with a circle. No clear correlation between AIC and wind condition was found from Figure 4.3. The order p=9, which is the mean value of the optimal size of the block Hankel matrix of 10 samples, was obtained from Figure 4.3, and used throughout this study.

The stabilization diagram is adopted to extract stable modes as described in Section 3.3.1. To avoid the spurious system poles, this study adopted a strict rule to extract the stable modes: they must satisfy all the stability criteria in Eqs. 3.54–3.56 with thresholds as $f_{th} = 0.005$ Hz, $\xi_{th} = 0.5$ %, $\mathrm{MAC}_{th} = 0.95$, and $\kappa_{th} = 3$. The results for the stabilization diagrams are given in Section 4.5.

4.3.2 Bayesian operational modal analysis

As mentioned in Section 3.2.3 the BAYOMA requires preliminary analysis to find the frequency band of the FFT data to be analyzed in advance to the modal analysis. This study provides singular value spectrum (SVS) [77], which is defined as singular values of the cross power spectral density matrices, calculated from the time series of the measured acceleration. Each of the cross power spectrum densities for calculating the SVS is estimated as the Welch's overlapped segment averaging estimator [58], where

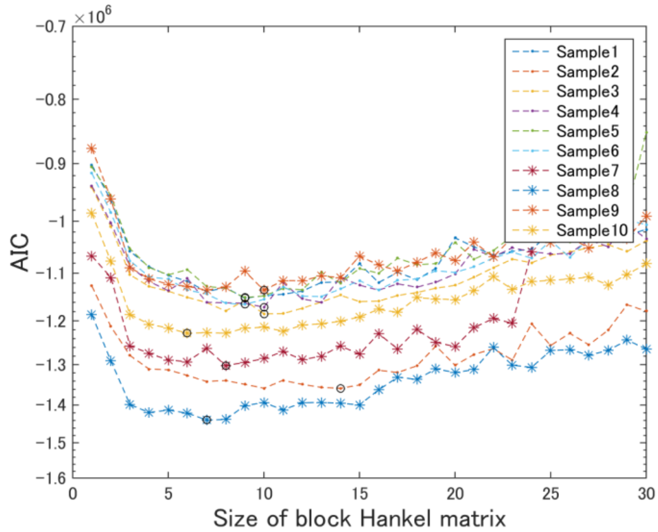

Figure 4.3 AIC with respect to size of the block Hankel matrix.

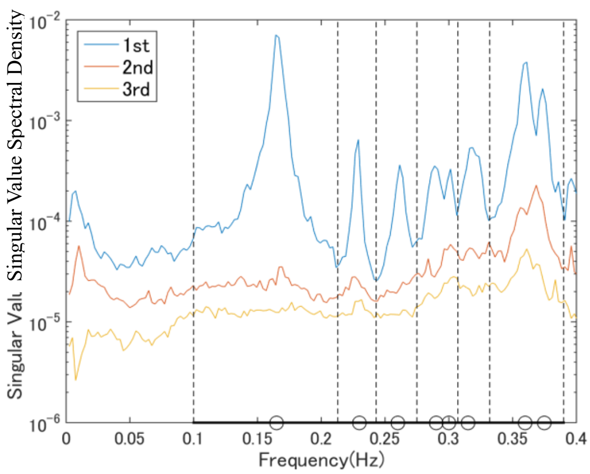

Figure 4.4 Averaged SVS and the frequency bands for identification

the time series are divided into 400 sec segments with 50% overlap, and windowed with the Hamming window. Figure 4.4 shows the SVS averaged for the every 10 samples. From the first to third SVS curves are depicted in Figure 4.4 to examine existence of close modes. Figure 4.4 shows that 8 peaks are observed in the first SVS curve, and no predominant peaks are observed in the second or third SVS. This study therefore adopt 8 initial values of natural frequencies for BAYOMA, which are depicted as black circles on the horizontal axis in Figure 4.4. The frequency bands for the optimization is selected as their ranges

Table 4.2 Identified natural frequencies (Hz) and coefficient of variance (%)

Mode no.	Method		Weak wind						Typhoon			
			S1	**S2**	**S3**	**S4**	**S5**	**S6**	**S7**	**S8**	**S9**	**S10**
1	BYOMA	MPV	0.159	0.158	0.158	0.160	0.156	0.158	0.165	0.162	0.160	0.163
		c.o.v.	0.3	0.3	0.3	0.4	0.5	0.4	0.3	0.3	0.4	0.3
	SSI		0.161	0.161	0.162	0.163	0.162	0.164	0.167	0.164	0.165	0.165
2	BYOMA	MPV	0.227	0.227	0.221	0.230	0.231	0.224	0.227	0.227	0.227	0.226
		c.o.v.	0.2	0.5	1.7	2.3	1.5	0.7	0.1	0.1	0.1	0.1
	SSI		-	-	-	-	-	-	0.227	0.227	0.227	0.226
3	BYOMA	MPV	0.257	0.259	0.259	0.258	0.258	0.260	0.263	0.264	0.259	0.260
		c.o.v.	0.2	0.2	0.1	0.1	0.3	0.1	0.1	0.1	0.3	0.2
	SSI		0.255	0.255	0.258	0.257	0.258	0.260	0.263	0.264	0.257	0.260
4	BYOMA	MPV	0.288	0.290	0.288	0.288	0.285	0.287	0.290	0.292	0.287	0.290
		c.o.v.	0.2	0.1	0.2	0.1	0.2	0.5	0.2	0.2	0.2	0.2
	SSI		0.287	0.287	0.284	0.286	0.282	0.285	0.289	0.292	0.287	0.289
5	BYOMA	MPV	0.303	0.300	0.299	0.298	0.299	0.297	0.301	0.298	0.300	-
		c.o.v.	0.1	0.2	0.2	0.2	0.2	0.2	0.2	0.2	0.2	-
	SSI		-	0.294	-	-	-	0.293	0.297	0.301	0.300	0.300
6	BYOMA	MPV	0.310	0.314	0.311	0.316	0.313	0.319	0.322	0.323	0.319	0.317
		c.o.v.	0.1	0.1	0.2	0.1	0.2	0.2	0.2	0.2	0.2	0
	SSI		0.307	0.310	0.308	0.315	0.312	0.318	0.323	0.324	0.319	0.317
7	BYOMA	MPV	0.357	0.362	0.363	0.357	0.357	0.359	0.363	0.362	0.364	0.359
		c.o.v.	0.2	0.2	0.2	0.1	0.2	0.2	0.1	0.1	0.3	0.1
	SSI		0.358	0.364	0.360	0.358	0.357	0.358	0.361	0.368	0.358	0.359
8	BYOMA	MPV	0.370	0.370	0.368	0.371	0.368	0.371	0.369	0.372	0.367	0.373
		c.o.v.	0.1	0.1	0.1	0.1	0.1	0.1	0.2	0.1	0.3	0.1
	SSI		0.373	0.374	0.374	0.372	0.372	0.374	0.374	0.373	0.374	0.372

*S1, Sample 1; … S10, Sample 10; c.o.v., coefficient of variance cover the peaks. If the natural frequencies are close to each other, the modal responses can be affected to the other one [46], [78]. Thus, the close modes are optimized in a same frequency band. This study adopts 6 frequency bands as the black thick lines on the horizontal axis separated into the 6 parts by the vertical dashed lines in Figure 4.4.

Table 4.3 Identified damping ratios (%) and coefficient of variance (%)

Mode no.	Method		Weak wind						Typhoon			
			S1	**S2**	**S3**	**S4**	**S5**	**S6**	**S7**	**S8**	**S9**	**S10**
1	BYOMA	MPV	1.90	2.39	2.94	3.61	5.67	4.76	2.22	2.24	5.26	2.92
		c.o.v.	13.9	13.1	12.0	11.0	10.0	10.6	12.5	12.5	9.4	11.4
	SSI		0.82	0.69	1.01	0.93	0.95	1.10	1.57	1.72	3.38	1.54
2	BYOMA	MPV	0.92	3.03	5.55	10.27	6.40	3.28	0.60	0.50	0.37	0.62
		c.o.v.	46.5	23.4	35.6	61.6	41.5	26.8	21.2	22.8	25.7	21.0
	SSI		-	-	-	-	-	-	0.81	0.51	0.62	0.71
3	BYOMA	MPV	1.12	1.16	0.83	0.76	2.42	0.58	0.87	0.73	2.46	1.14
		c.o.v.	17.8	18.3	19.6	19.3	18.2	21.3	18.0	19.0	17.4	17.2
	SSI		1.75	1.83	1.43	1.37	3.76	1.30	0.82	0.74	3.12	1.39
4	BYOMA	MPV	0.91	0.72	1.01	0.76	1.35	3.55	1.04	1.55	1.38	1.71
		c.o.v.	18.5	19.5	18.1	18.8	17.4	21.3	17.0	16.6	16.7	16.3
	SSI		1.95	1.76	2.85	1.94	3.15	4.14	1.19	1.47	1.35	1.59
5	BYOMA	MPV	0.65	0.97	0.73	1.38	0.89	1.34	1.13	1.28	1.39	-
		c.o.v.	24.3	25.5	25.2	20.8	25.2	21.3	19.4	17.7	19.6	-
	SSI		-	0.67	-	-	-	1.95	1.68	1.08	0.90	1.58
6	BYOMA	MPV	0.45	0.64	0.84	0.85	1.24	1.02	0.70	0.87	2.00	0.94
		c.o.v.	23.5	20.7	20.5	19.5	19.3	19.1	19.2	19.0	20.4	18.3
	SSI		2.34	2.36	3.26	2.30	2.62	2.08	0.91	0.87	1.18	0.89
7	BYOMA	MPV	1.43	1.74	2.10	0.72	1.47	0.54	2.00	0.71	1.17	0.66
		c.o.v.	11.2	9.4	9.2	17.2	0.94	28.9	8.5	15.6	17.0	16.1
	SSI		0.82	1.21	0.95	0.96	0.77	0.81	1.20	2.51	1.04	0.91
8	BYOMA	MPV	0.46	0.50	0.63	0.50	0.66	1.10	1.09	0.97	2.12	0.66
		c.o.v.	19.7	19.7	21.1	17.9	14.8	17.5	15.1	13.8	10.7	17.1
	SSI		1.16	1.52	1.25	0.99	1.34	1.13	1.90	0.87	1.43	0.84

*S1, Sample 1; … S10, Sample 10; c.o.v., coefficient of variance

4.4 Identified Modal Properties

Identified natural frequencies are presented in Table 4.2. The identified damping ratios are presented in Table 4.3. For BAYOMA, the coefficient of variance (c.o.v.), which is defined as the expectation divided by its standard deviation, is also calculated based on the posterior distribution. The mode with blanks in Table 4.2 and Table 4.3 were not identified by the SSI or BAYOMA. That is, for SSI, the poles of these modes are too unstable to satisfy the stability criteria, and thus they are expelled from the identification. The identified results are comparable to results reported in [53], i.e. the second mode (0.23 Hz) is not identified under weak wind conditions. The fifth modes for Sample 1 and Samples 3–5 were not identified for SSI. For BAYOMA, the fifth mode for Sample10 was not identified because of the objective function was not converged in the numerical analysis.

The identified frequencies showed similar results between the SSI and BAYOMA except the deficient second mode. The identified damping ratios did not agree to each other, though both of the results describes low damping such that the damping ratios are around 1% or 2%. In fact, this observation is reasonable since the precise identification of the damping ratios are difficult only from ambient vibration [50], [51]. Most of the coefficients of variance are lower than 1 % for the natural frequencies identified

Mode No.	BAYOMA	SSI
1	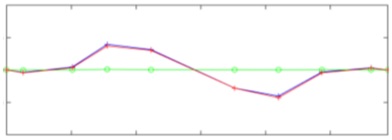	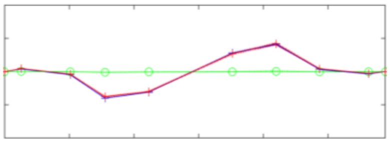
2	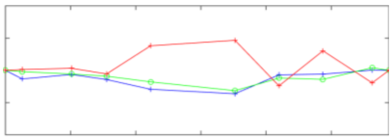	Not Identified
3	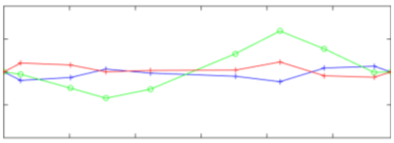	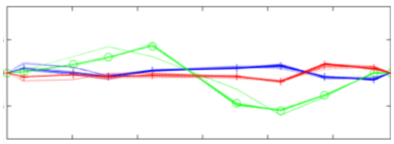
4	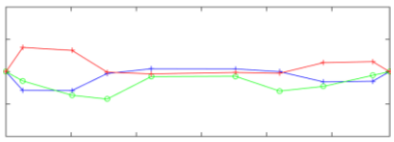	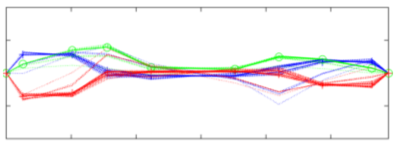

Figure 4.5 Example of identified mode shapes under weak wind (Sample 1)

by BAYOMA except the second mode, whereas the coefficients of variance for the damping ratios are around 10% or 20%. These results describe that the identified natural frequencies are more likely than the damping ratio. This observation also shows that the variance of the posterior distribution provides a scale to measure how reliable the identified results are.

Mode shapes from the first to the fourth modes obtained from Sample 1 (weak wind condition), and Sample 7 (typhoon condition), are respectively presented in Figure 4.5 andFigure 4.6 for instance. In each of the diagram, the horizontal axis represent the longitudinal sensor locations and the vertical axis represent the modal displacements. The color of those lines are relevant to the colors of the arrows depicted in Figure 4.2. For SSI, the dotted lines show the identified modal shapes obtained by the stability criteria. The solid lines show their mean values. The mode shape of the deficient second mode under weak wind condition resulted in vague shape even for BAYOMA. Actually, the identified modal properties of deficient mode were less reliable from the viewpoint of the Bayesian statistics as discussed later. The other mode shapes in Figure 4.5 and 4.6 provide similar results as well as the natural frequencies. The further discussion about the mode shapes of higher modes are given in [49].

Mode No.	BAYOMA	SSI
1	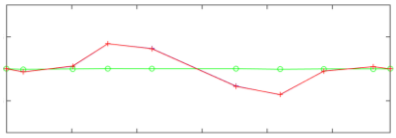	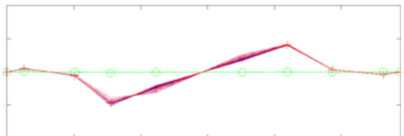
2	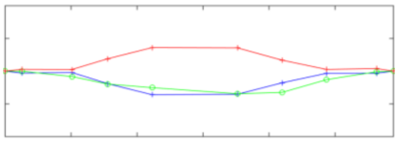	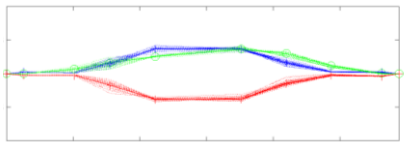
3	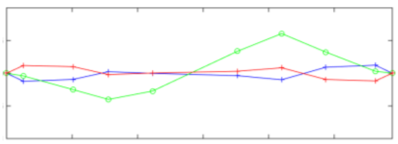	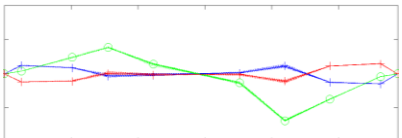
4	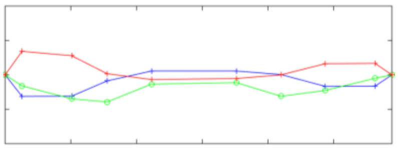	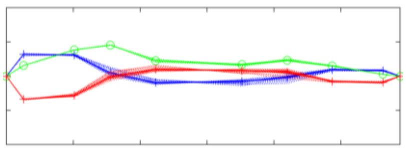

Figure 4.6 Example of identified mode shapes under typhoon (Sample7)

4.5 Investigation of the Uncertainty

Here, further investigations are provided to examine how to describe uncertainty involved in modal identification, especially in the feature extraction process. The stabilization diagrams for the SSI are examined at first. Figure 4.7 and 4.8 respectively portray stabilization diagrams of data obtained under weak wind, and typhoon conditions. The model order for the singular value decomposition is considered from 1 to 80 for each of the diagrams.

The stabilization diagrams portrayed in Figure 4.7 demonstrate that the second mode (at 0.23 Hz) was

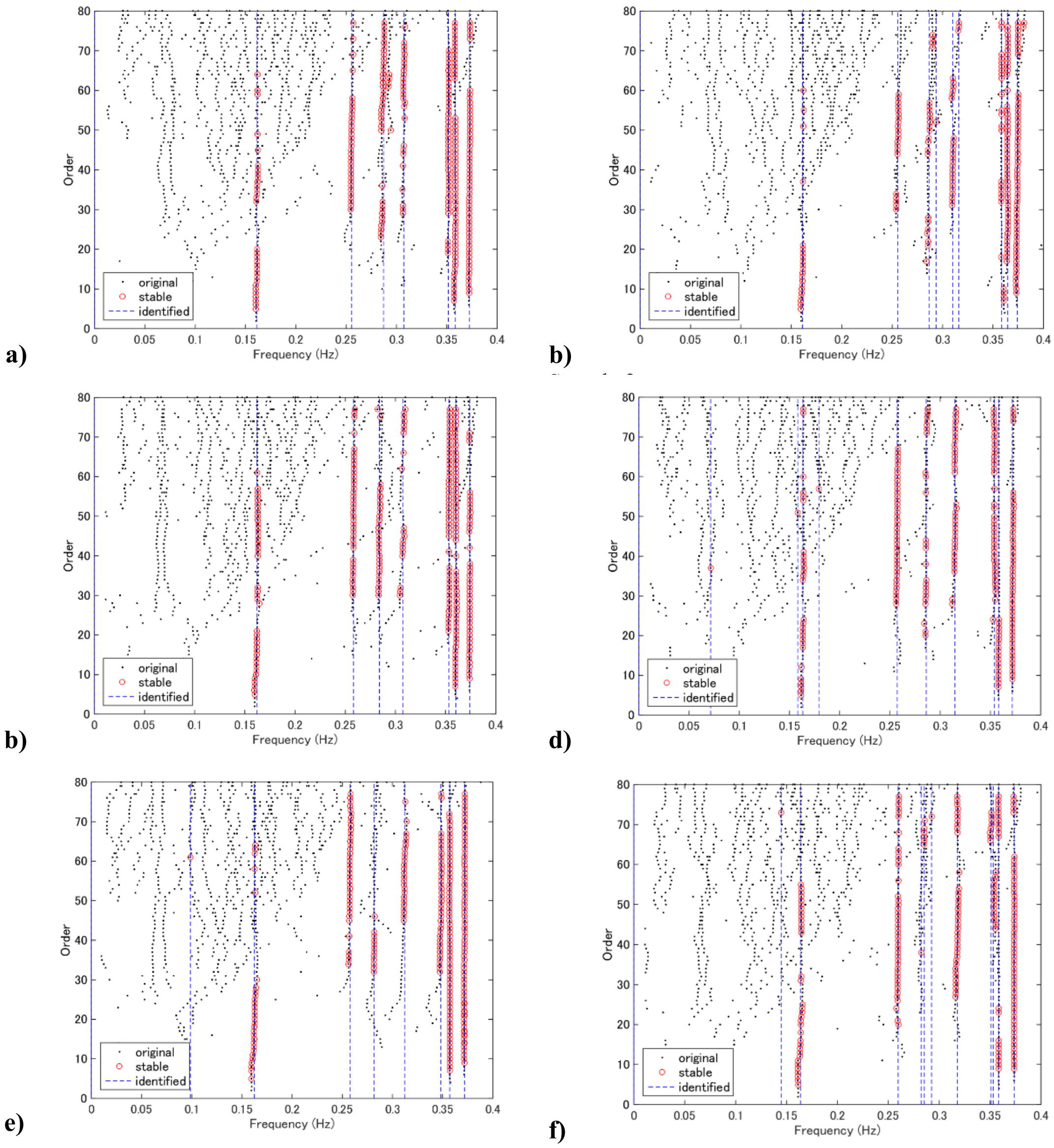

Figure 4.7 Stabilization diagrams under the weak wind conditions:

a) Sample 1; b) Sample 2; c) Sample 3; d) Sample 4; e) Sample 5; f) Sample 6.

not identified under weak wind conditions. The diagrams show that unstable poles are scattered widely in the frequency band below 0.23 Hz. No clear stable poles were observed on the frequency of the second mode (0.23 Hz). However, under typhoon conditions, fewer unstable poles were observed in the frequency

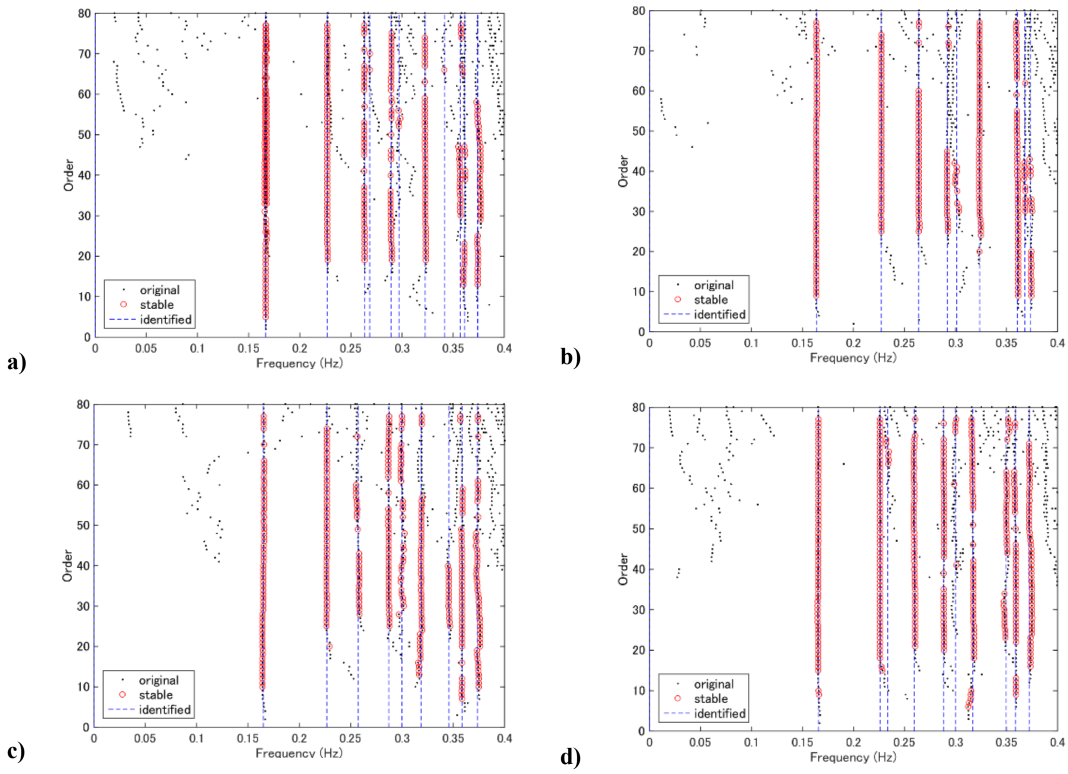

Figure 4.8 Stabilization diagrams under the typhoon conditions:

a) Sample 7; b) Sample 8; c) Sample 9; d) Sample 10

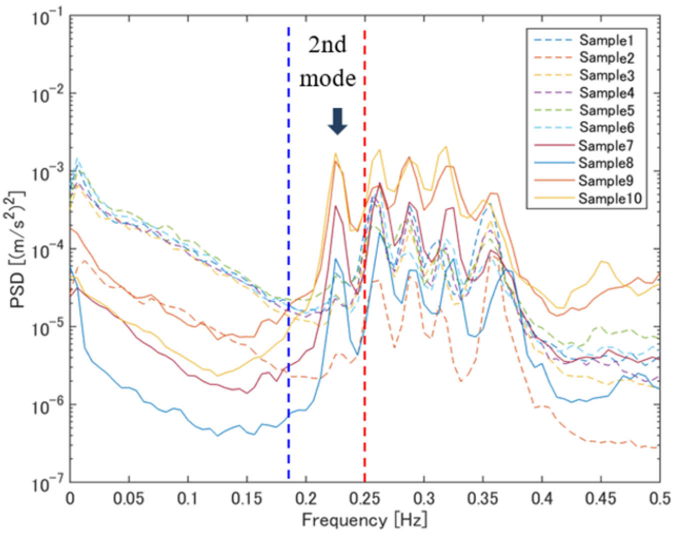

Figure 4.9 Mean value of the lateral acceleration PSD

band below 0.23 Hz as presented in Figure 4.8. In other words, the typhoon condition led to stable poles related to the second mode. The observation described above from the stabilization diagrams in Figure 4.7 and 4.8 demonstrated that lower modes were contaminated easily by unknown noise under weak wind conditions. However, under typhoon conditions, structural modes were well excited.

The mean values of the PSD of lateral accelerations for each sample are presented in Figure 4.9, where each of the PSD is estimated by the Welch's method as used in Figure 4.4. Those PSD curves show that the bridge vibrations of the frequency band below 0.23 Hz in the transverse direction under weak wind conditions showed higher PSD than those under typhoon or critical conditions. Especially for the lower frequency band below 0.18 Hz, most PSDs of the transverse accelerations under the weak winds exceed the PSDs of the typhoon and critical conditions, even though the exciting wind speed is less than that in typhoon conditions. A possible reason might be the influence of traffic that was controlled during the typhoon.

To investigate differences of identified systems under different wind conditions, the CCR of singular values of the system is considered. The CCR of model order n is defined as

$$CCR = \frac{\sum_{i=1}^{q} s_i}{\sum_{i=1}^{mp} s_i} \tag{4.1}$$

Therein, s_i is the i-th singular value obtained by the singular value decomposition in Eq. 3.23. q is the number of the singular values adopted to the estimation of the state space model. The CCR estimated from all samples is shown with respect to the model order as presented in Figure 4.8. The results show that, in considering the same model order, the typhoon condition led to higher CCR than the weak wind condition did. In other words, in considering same model order, the CCR under the typhoon condition

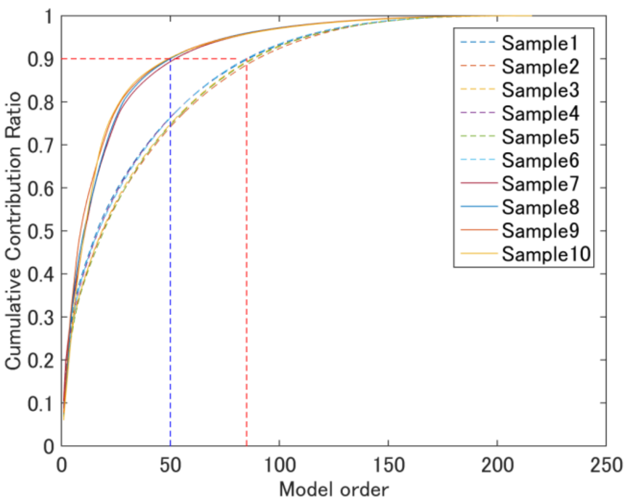

Figure 4.8 Cumulative contribution ratios of singular values calculated in SSI.

includes more information about the system than that under the weak wind condition. Therefore, vibrations of the bridge under typhoon conditions can be modeled as a dynamic system with lower model order. For example, a system model containing 90% of the measurement information can be described by the model order of 50 under a typhoon condition (see the vertical broken lines at the model order of 50 in Figure 4.8). However, a model order of 85 is necessary to include 90% of the system information under weak wind conditions (see vertical broken lines near the model order of 90 in Figure 4.8). The observation described above implies that the spurious poles observed in Figure 4.7 disturb the effective model reduction by means of the SSI.

The feature extraction process for the modal properties are numerically realized in the Bayesian inference. The coefficients of variances of the identified natural frequencies and damping ratios are summarized in Figure 4.9. The results show that the variances of natural frequencies and damping ratios of the second mode are higher under the weak wind condition comparing to the other modes. This observation describes the uncertainty of the identified model is quantified through the posterior distribution.

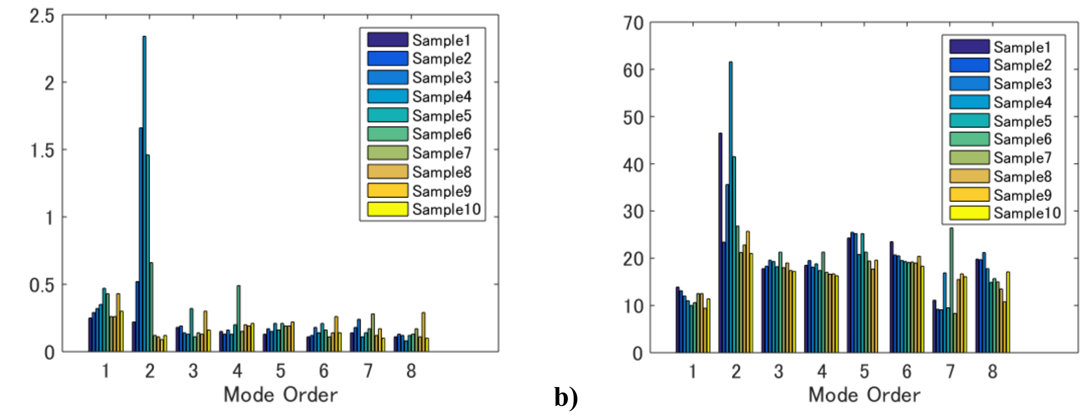

a) b)

Figure 4.9 Coefficient of variance (%): a) For natural frequencies; b) For damping ratios.

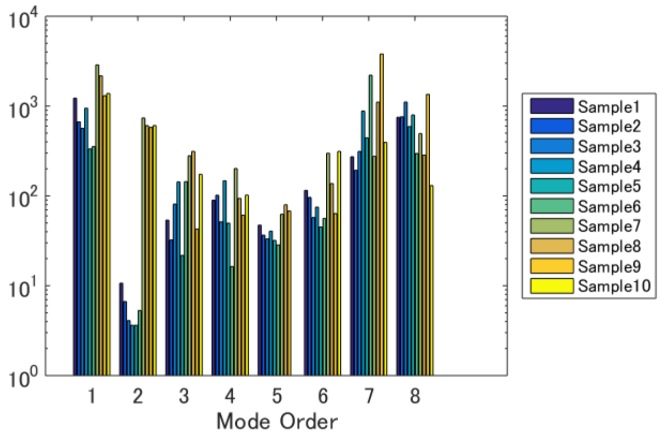

Figure 4.10 Signal to noise ratios of the modal responses.

Furthermore, the BAYOMA enables to quantify the PSD matrix modal responses as $\mathbf{H}_k$ in Eq. 3.37. A signal to noise ratio is thus definable as a ratio of the PSD of the modal response to the PSD of the estimated measurement error. The diagonal elements of $\mathbf{H}_k$ are simplified at the resonant frequencies of the i-th mode as

$$\mathbf{H}_k(i,i) = |h_{ik}|^2 S_{ii} = \frac{S_{ii}}{4\xi_i^2} \tag{4.2}$$

where S_{ii} is the i,i elements of the PSD matrix of modal forces $\mathbf{S}$. Accordingly, the signal to noise ratio [44] is generated as

$$\gamma_i = \frac{S_{ii}}{4S_e\xi_i^2} \tag{4.3}$$

Since most provable values of S_{ii}, S_e and ξ_i are identified through the Bayesian inference, the signal to noise ratios are also identified from those values. Figure 4.10 summarizes the identified signal to noise ratios for the modal responses. The results show the signal to noise ratios of the second mode under the weak wind condition are lower than the other modes as well as the coefficient of variables. Thus, the signal noise ratio also provides a scale to quantify the uncertainty of identified modes.

4.6 Summary

The uncertainty involved in mode identification of a multi-span cable-stayed bridge under different wind conditions was investigated as a benchmark study. To investigate the complex dynamic behavior of the target bridge, multiple measurements with 24 accelerometers are operated. In this case, Yule-Walker method, which is one of well-known time domain analysis method introduced in Chapter 3, is not suitable for modal analysis since the multiple measurements with higher degree of freedom produce many spurious poles in the estimated mechanical model. This chapter therefore adopted stochastic subspace identification (SSI) and Bayesian operational modal analysis (BAYOMA) to identify modal properties. Stabilization diagrams of given data were examined to extract stable modes for the SSI. For the BAYOMA, the posterior distributions of the modal properties were briefly investigated through their coefficients of variance.

Identified modal properties compared with results of earlier studies: a deficient second mode whose identifiability depends on wind conditions was observed. The stabilization diagrams of data measured under weak wind conditions showed widely scattered unstable poles in the frequency band below 0.23 Hz, but no clear stable pole at the frequency of the second mode (0.23 Hz). However, under typhoon conditions, less unstable poles were observed in the frequency band below 0.23 Hz; stable poles were observed on the frequency of the second mode. In other words, lower modes might be contaminated easily by unknown noise under weak wind conditions. Under a typhoon, structural modes were well excited and the system matrix was dominated by modal response rather than noise, which might link with the mode identifiability of the second mode.

Observations from PSD curves of lateral acceleration showed that, especially in the low frequency band below 0.18 Hz, most PSDs of the lateral accelerations under weak winds exceed the PSDs of the typhoon condition, even though the exciting wind speed is less than that under typhoon conditions. A reason for stronger PSDs appearing under the weaker wind conditions than those of a typhoon below the frequency range of 0.18 Hz might be the influence of traffic. Observations also demonstrated that the cumulative contribution ratio reaches a higher ratio with less model order under typhoon conditions than under weak wind. This observation implies that spurious poles observed in stabilization diagrams reduced the quantity of the information contained in the identified system models.

The posterior distribution obtained by BAYOMA briefly provided relevant results to the above observations. The coefficient of variances of the natural frequency and damping ratio showed that the most probable values of those properties are less reliable for the second mode under weak wind condition than the other modes. This observation demonstrates feasibility of the posterior distribution to quantify uncertainty involved in modal identification. Signal to noize ratio, which is defined as a ratio of a modal response to measurement error, also quantify how reliable the identified modal properties. Although Bayesian inference can be a way to describe modal properties as uncertain random valiables, BAYOMA requires preliminaly analysis in frequency domain to extract proper frequency band to be analysed. Aiming at practical uses, more concise Bayesian analysis method is desiable. The further discussion about Bayesian inference for structural health monitoring is given in Chapter 6.

Chapter 5

Damage Sensitive Features

5.1 Introduction

This chapter mainly aims to improve existing damage indicators by investigating damage sensitive features involved in the system models. Several existing studies have investigated feasibility of the autoregressive (AR) coefficients as damage sensitive features since they are easily obtained from the observed time series. For instance, Nair [55] proposed so-called Nair's damage sensitive feature (NDSF), which consists of univariate AR coefficients. NDSF was investigated as a damage indicator for a model building. A laboratory experiment conducted on a model bridge shows the feasibility of NDSF for health monitoring of bridges based on traffic-induced vibrations [56]. In that laboratory experiment, a damage detection method evaluating stochastic distance by the Mahalanobis distance (MD) [79], [80] was proposed to evaluate the statistical distance between groups of samples of NDSF. The validity of this damage detection method has also been verified from results of field experiments conducted on real steel truss bridges with artificial damage to its truss members [51]. It is noteworthy that the NDSF includes information about vibrations of each sensor, but information about relationship between the measurement locations is not included because it is derived from the univariate AR model.

Chang and Kim [50] investigated the MD sensitivity to modal parameters attributable to damage. They concluded that considering all the modal parameters including modal frequency, damping ratio, and the modal assurance criterion from the mode vector demonstrated that the inclusion of the more parameters in outlier analysis might engender the more sensitive features. That is because any statistical change in those features would be reflected in the MD, which indicates that the mode vector, which is a kind of correlation between sensors, would provide useful information related to the bridge health condition. However, it is not straightforward to decide damage sensitive modes as well as relevant mode vectors for healthy bridges. Therefore, aiming at a pattern recognition approach to estimate damage sensitive modes or damage locations, a novel damage indicator is derived directly from a multivariate linear system to include spatial information between sensors.

This chapter thus proposes a damage indicator based on the MD of damage sensitive features that are extracted directly from a multivariate AR model using principal component analysis (PCA) [81]. The proposed damage indicator evaluates stochastic changes in modal information contained in the multivariate AR model, whereas the NSDF is merely based on univariate AR model. Therefore, the damage indicator is expected to detect changes in modal properties related to correlation among measurement points and improve damage detection performance. This study also proposes a damage detection approach based on the hypothesis test to enable stochastically appropriate decision-making. Acceleration data from the field experiment in Section 1.4 is examined to validate the feasibility of the proposed method. This study investigates the efficacy of the presented damage indicator and hypothesis testing for three damage patterns considered in the experiment. The NDSF is also examined using the field experiment data and compared to the proposed damage indicator.

5.2 Damage Indicator from Multivariate Linear System

5.2.1 Damage detection flow

This study investigates an unsupervised change detection method for changes between a reference dataset obtained from a bridge under healthy condition and a newly observed dataset monitored from the same bridge under artificial damage. The former dataset is designated as the “reference set”, and the latter is as the “test set.” An outline of the calculation of the novel damage indicator and damage detection is presented in Figure 5.1. Outline of each process is as follows.

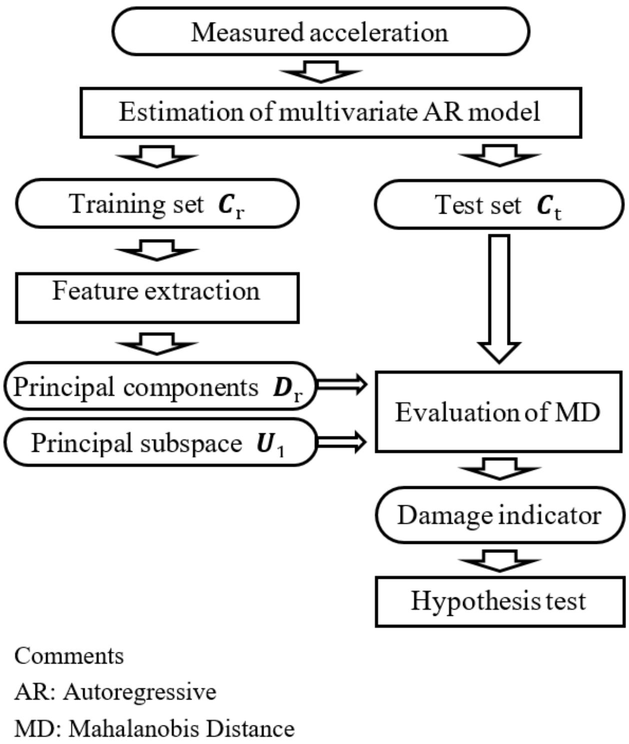

Figure 5.1 Flow of damage detection utilizing the proposed damage indicator

- Parameter vectors related to modal properties of the structure are estimated from measured acceleration data using the multivariate AR model (see Section 5.2.2).
- Damage sensitive features and the corresponding subspace are extracted by application of the PCA to the reference set (see Section 5.2.2).
- The proposed damage indicator is defined using MD between the reference set and the test set with respect to the damage-sensitive features (see Section 5.2.3).
- Damage detection is formulated as a hypothesis testing based on the probability distribution of the damage indicator (see Section 5.2.3).

5.2.2 Feature extraction

Let $\boldsymbol{y}_k$ denote a column vector of the discrete time series of measured acceleration data whose components respectively correspond to m measurement locations. As mentioned in Section 2.2.3, the time series obtained from a linear structural system excited by white noise can be modeled as an (multivariate) AR model of sufficient model order p.

$$\boldsymbol{y}_k = \sum_{i=1}^{p} \boldsymbol{\alpha}_i \boldsymbol{y}_{k-i} + \boldsymbol{e}_k. \tag{5.1}$$

The system poles of the transfer function of the above linear system are obtainable by solving the eigenvalue problem represented by the following characteristic equation with respect to z

$$\left| \boldsymbol{I}\boldsymbol{z} - \acute{\boldsymbol{A}} \right| = 0 \tag{5.2}$$

$$\acute{\boldsymbol{A}} = \begin{bmatrix} \boldsymbol{O} & \boldsymbol{I} & \cdots & \boldsymbol{O} \\ \vdots & \vdots & \ddots & \vdots \\ \boldsymbol{O} & \boldsymbol{O} & \cdots & \boldsymbol{I} \\ \boldsymbol{\alpha}_p & \boldsymbol{\alpha}_{p-1} & \cdots & \boldsymbol{\alpha}_1 \end{bmatrix}. \tag{5.3}$$

The AR coefficient matrices appearing in Eq. 5.3 is obtainable by means of the Yule-Walker method (See Section 3.2.1). The characteristic equation in Eq. 5.2 can be rearranged to the following polynomial equation with the appropriate polynomial coefficients c_i:

$$z^l + c_1 z^{l-1} + \cdots + c_{l-1} z^1 + c_l = 0 \tag{5.4}$$

where $l = mp$. Since the roots of the above polynomial are equivalent to eigenvalues of $\acute{\boldsymbol{A}}$, each of the polynomial coefficients has the following relationship with system poles [55].

$$c_1 = \sum_{r_1=1}^{l} z_{r_1}^{\text{pole}} \tag{5.5}$$

$$c_2 = \sum_{r_1=1}^{l} \sum_{r_2=r_1+1}^{l} z_{r_1}^{\text{pole}} z_{r_2}^{\text{pole}} \tag{5.6}$$

$$c_3 = \sum_{r_1=1}^{l} \sum_{r_2=r_1+1}^{l} \sum_{r_3=r_2+1}^{l} z_{r_1}^{\text{pole}} z_{r_2}^{\text{pole}} z_{r_3}^{\text{pole}} \tag{5.7}$$

$$\vdots$$

where z_r^{pole} $(r = 1 \dots l)$ corresponds to any of the eigenvalues of $\acute{\boldsymbol{A}}$, i.e.,

$$z_r^{\text{pole}} = \exp\left[\left(-\xi_i\omega_i \pm j\sqrt{1-\xi_i^2}\omega_i\right)\Delta t\right] \tag{5.8}$$

where ω_i and ξ_i are respectively angular natural frequencies and damping ratios mentioned in Section 2.3.1. Therefore, changes in modal properties of the structure alter the polynomial coefficients. The transformation from the time series of acceleration to the AR coefficients easily realized by the Yule-Walker method mentioned in Section 3.2.1, and transformation from the AR coefficients to polynomial coefficients is realized in the characteristic equation. Thus, each of the polynomial coefficients can be regarded as random variables, namely, mapping of random events onto a real value. This study assumes a coefficient vector $\boldsymbol{c} = [c_1\ \ c_2 \dots c_l]^{\mathrm{T}}$ is a vector consisting of random variables that follow a multivariate Gaussian distribution produced from an independent observation of the bridge vibration. These coefficients presumably change their statistical characteristics when damage on a structure causes any change in the modal properties. Therefore, the proposed damage detection method is formulated to detect changes in these coefficients.

To formulate the change detection method, the coefficient vectors $\boldsymbol{c}$ obtained from measurement data are classified into a reference set and a test set. Let $\boldsymbol{c}_i$ $(i = 1, 2 \dots, n_{\mathrm{r}})$ and $\boldsymbol{c}'_i$ $(i = 1, 2 \dots, n_{\mathrm{t}})$ respectively denote the reference samples and the test samples of the coefficient vectors. Each of the sets is described as a matrix comprising the sample vectors, i.e. the reference set and the test set are described as follows.

$$\boldsymbol{C}_{\mathrm{r}} = [\boldsymbol{c}_1\ \ \boldsymbol{c}_2 \dots \boldsymbol{c}_{n_{\mathrm{r}}}] \tag{5.9}$$

$$\boldsymbol{C}_{\mathrm{t}} = [\boldsymbol{c}'_1\ \ \boldsymbol{c}'_2 \dots \boldsymbol{c}'_{n_t}] \tag{5.10}$$

Damage-sensitive features are extracted using the PCA with respect to the reference set. The PCA is definable as the orthogonal projection of the data onto a lower dimensional linear space, known as the principal subspace, such that the variance of the projected data is maximized [81]. Kim et al. [82] reported that the damage sensitivity of the NDSF is improved by application of the PCA to the estimated AR coefficients of a univariate AR model. The polynomial coefficients are relevant to the AR coefficients in univariate case, and thus the PCA is expected to extract damage-sensitive features from the reference set. For the reference set, the PCA provides a lower order orthogonal vector space in which variances among the samples contained in reference set are maximized. The orthogonal space, which is referred as principal subspace, thus represents feature on the reference set. The sample vectors projected onto the principal subspace are referred as principal components. This study presumes that the principal components represent damage-sensitive features. The orthonormal basis of the principal subspace is defined by the q eigenvectors corresponding to the q largest eigenvalues of the data covariance matrix. The PCA is performed by means of the singular value decomposition (SVD) to a matrix comprising deviation vectors of the reference samples as

$$\boldsymbol{C}_{\mathrm{dev}} = [\tilde{\boldsymbol{c}}_1 \quad \tilde{\boldsymbol{c}}_2 \quad \dots \quad \tilde{\boldsymbol{c}}_n]. \tag{5.11}$$

where, $\tilde{\boldsymbol{c}}_i$ represents the deviation vectors defined as

$$\tilde{\boldsymbol{c}}_i = \boldsymbol{c}_i - \frac{1}{n}\sum_{k=1}^{n}\boldsymbol{c}_k \quad (i = 1,2,\dots,n). \tag{5.12}$$

The basis of the principal subspace is provided as the sub-matrix $\boldsymbol{U}_1$ using the SVD.

$$\boldsymbol{C}_{\mathrm{dev}} = \boldsymbol{U}\boldsymbol{S}\boldsymbol{V}^{\mathrm{T}} = [\boldsymbol{U}_1 \;\; \boldsymbol{U}_2]\boldsymbol{S}\boldsymbol{V}^{\mathrm{T}} \tag{5.13}$$

Therein, $\boldsymbol{S} \in \mathbb{R}^{l \times n_r}$ denotes diagonal matrix whose diagonal entries are non-negative real numbers listed in descending order. $\boldsymbol{U} \in \mathbb{R}^{l \times l}$ and $\boldsymbol{V} \in \mathbb{R}^{n_r \times n_r}$ stand for the corresponding orthogonal matrices. $\boldsymbol{U}_1 \in \mathbb{R}^{l \times q}$ represents the sub-matrix which consists of the first q columns of $\boldsymbol{U}$, and $\boldsymbol{U}_2$ represents the sub-matrix excluded $\boldsymbol{U}_1$ from $\boldsymbol{U}$.

Using the basis of the principal subspace $\boldsymbol{U}_1$, the principal components of a vector composed of polynomial coefficients $\boldsymbol{c}$ is given as

$$\boldsymbol{d} = {\boldsymbol{U}_1}^{\mathrm{T}}\boldsymbol{c}. \tag{5.14}$$

Thus, the principal components of the reference and the test sets are respectively given as following matrices.

$$\boldsymbol{D}_{\mathrm{r}} = \boldsymbol{U}_1^{\mathrm{T}}\boldsymbol{C}_{\mathrm{r}} = [\boldsymbol{d}_1 \;\; \boldsymbol{d}_2 \dots \;\; \boldsymbol{d}_{n_{\mathrm{r}}}] \tag{5.15}$$

$$\boldsymbol{D}_{\mathrm{t}} = \boldsymbol{U}_1^{\mathrm{T}}\boldsymbol{C}_{\mathrm{t}} = [\boldsymbol{d}'_1 \;\; \boldsymbol{d}'_2 \dots \;\; \boldsymbol{d}'_{n_{\mathrm{t}}}] \tag{5.16}$$

In the above equation, each of the column vectors included in $\boldsymbol{D}_{\mathrm{r}}$ and $\boldsymbol{D}_{\mathrm{t}}$ respectively corresponds to principal components of the reference data in $\boldsymbol{C}_{\mathrm{r}}$ and $\boldsymbol{C}_{\mathrm{t}}$.

5.2.3 Damage indicator and hypothesis testing

Let $\boldsymbol{d}_1, \boldsymbol{d}_2, \dots, \boldsymbol{d}_{n_{\mathrm{r}}}$ independently follow Gaussian distribution with expectation $\boldsymbol{\mu}_{\mathrm{r}}$ and covariance matrix $\boldsymbol{\Sigma}$, where the true values of the parameters are supposed to be unknown. Similaly, let $\boldsymbol{d}'_1, \boldsymbol{d}'_2, \dots, \boldsymbol{d}'_{n_{\mathrm{t}}}$ independently follow Gaussian distribution with expectation $\boldsymbol{\mu}_{\mathrm{t}}$ and covariance matrix $\boldsymbol{\Sigma}$. Supposing that the reference dataset $\{\boldsymbol{d}_1, \boldsymbol{d}_2, \dots, \boldsymbol{d}_{n_{\mathrm{r}}}\}$ and one of the test sample $\boldsymbol{d}'_i$ are given, this study provides hypothesis testing to assess whether $\boldsymbol{\mu}_{\mathrm{r}} = \boldsymbol{\mu}_{\mathrm{t}}$ or $\boldsymbol{\mu}_{\mathrm{r}} \neq \boldsymbol{\mu}_{\mathrm{t}}$. The following (normalized) MD is traditionally used to detect an anomalous sample referring to a set of normal samples [79], [80].

$$MD(\boldsymbol{d}_i') = \frac{1}{q}(\boldsymbol{d}_i' - \widehat{\boldsymbol{\mu}}_\mathrm{r})^\mathrm{T}\widehat{\boldsymbol{\Sigma}}^{-1}(\boldsymbol{d}_i' - \widehat{\boldsymbol{\mu}}_\mathrm{r}), \tag{5.17}$$

where $\widehat{\boldsymbol{\mu}}_\mathrm{r}$ and $\widehat{\boldsymbol{\Sigma}}$ respectively signify the most likelihood estimators of the expectation and the covariance matrix estimated from $\boldsymbol{X}$ as defined as follows.

$$\widehat{\boldsymbol{\mu}}_\mathrm{r} = \frac{1}{n_\mathrm{r}}\sum_{i=1}^{n_\mathrm{r}} \boldsymbol{d}_i \tag{5.18}$$

$$\widehat{\boldsymbol{\Sigma}} = \frac{1}{n_\mathrm{r}}\sum_{i=1}^{n_\mathrm{r}}(\boldsymbol{d}_i - \widehat{\boldsymbol{\mu}}_\mathrm{r})\,(\boldsymbol{d}_i - \widehat{\boldsymbol{\mu}}_\mathrm{r})^\mathrm{T}. \tag{5.19}$$

The MD given in Eq. 5.17 evaluates a sort of ‘distance’ between the reference dataset and the test sample. If the hypothesis $\boldsymbol{\mu}_\mathrm{r} = \boldsymbol{\mu}_\mathrm{t}$ is satisfied, and if a sufficient number of the reference samples is available, the expectation of the MD asymptotically converges to 1 [80]. Otherwise, the stochastic distance between the reference dataset and test sample is scaled onto the MD. Several existing studies thus adopt the MD to find anomalies among damage sensitive features [50], [56], [82].

The hypothesis testing is formulated by means of the likelihood ratio test of null hypothesis $\boldsymbol{\mu}_\mathrm{r} = \boldsymbol{\mu}_\mathrm{t}$ against alternative hypothesis $\boldsymbol{\mu}_\mathrm{r} \neq \boldsymbol{\mu}_\mathrm{t}$. The following T^2 statistic proposed by Hotelling [83] provides hypothesis testing for the expectations of multivariate random variables.

$$T^2 = \frac{n_\mathrm{r}-q}{(n_\mathrm{r}+1)} MD(\boldsymbol{d}_i'). \tag{5.20}$$

This study proposes T^2 given in Eq. 5.20 as a damage indicator. According to the assumptions, the likelihood ratio test with significance value α is given by following rejection region [84].

$$T^2 \geq F^*_{q,n_\mathrm{r}-q}(\alpha) \tag{5.21}$$

where $F^*_{q,n_\mathrm{r}-q}(\alpha)$ denotes the upper 100α % point of the F distribution of $(q, n_\mathrm{r} - q)$ degree of freedom. The PDF of the F distribution is defined as follows.

$$F_{q,n_\mathrm{r}-q}(x) = \frac{1}{B\left(\frac{q}{2}, \frac{n_\mathrm{r}-q}{2}\right)}\left(\frac{qx}{qx+n_\mathrm{r}-q}\right)^{\frac{q}{2}}\left(1 - \frac{qx}{qx+n_\mathrm{r}-q}\right)^{\frac{n_\mathrm{r}-q}{2}} x^{-1} \tag{5.22}$$

where $B(\cdot,\cdot)$ denotes the Beta function. The expectation of the F distribution is given as

$$\mathbb{E}_x\left[F_{q,n_\mathrm{r}-q}(x)\right] = \frac{n_\mathrm{r}-q}{n_\mathrm{r}-q-2}. \tag{5.23}$$

Eq. 5.21 provides the critical value for the hypothesis testing as $F^*_{q,n_\mathrm{r}-q}(\alpha)$, which is relevant to the predefined significance value α.

Note that this chapter only provides hypothesis testing with respect to the reference dataset

$\{\boldsymbol{d}_1, \boldsymbol{d}_2, \ldots, \boldsymbol{d}_{n_\mathrm{r}}\}$ and one of the test sample $\boldsymbol{d}'_i$ for simplicity, though the Hoteling's T^2 statistics even enables the comparison between the datasets $\{\boldsymbol{d}_1, \boldsymbol{d}_2, \ldots, \boldsymbol{d}_{n_\mathrm{r}}\}$ and $\{\boldsymbol{d}'_1, \boldsymbol{d}'_2, \ldots, \boldsymbol{d}'_{n_\mathrm{t}}\}$ by means of the likelihood ratio testing. Assuming that sufficient number of reference samples are available, the comparison between the two datasets are easily formulated as hypothesis testing using the χ^2 distribution. Damage detection using this approximated hypothesis testing is discussed in [85] by the author.

5.3 Case Studies

Here, validity of the proposed method is examined with the target bridge mentioned in Section 1.4. This chapter only investigates the scenarios where the vehicle passes over the bridge by 40km/h. Further studies with unsteady vehicle speed are given in Chapter 6.

Considering over-fitting in statistical models, the performance of a stochastic model on the reference set does not always satisfy predictive performance on newly observed data. One effective approach adopted to confirm the validity of the stochastic model is the use of validation samples, which are independent from a reference dataset and have identical stochastic properties to the reference dataset. However, in this experiment, the number of the samples is limited, so leave-one-out cross validation (CV) technique [57] is applied to assess the validity of the damage indicators. For example, letting a set containing n_r samples of time series of target variables $\{\boldsymbol{t}_1, \boldsymbol{t}_2, \ldots, \boldsymbol{t}_{n_\mathrm{r}}\}$ be obtained from a bridge without damage, take one of the time series (e.g., $\boldsymbol{t}_1$) out from this set as a test data, and then refer the set excluded the test sample $\{\boldsymbol{t}_2, \ldots, \boldsymbol{t}_{n_\mathrm{r}}\}$ as the reference dataset. The n_r damage indicators are thus calculable only from the n_r samples of time series. In this study, the CV samples are checked if they are not in the rejection region to ensure the validity of damage detection.

5.3.1 Preliminary investigation

Before starting damage detection, the order of the AR model should be ascertained because the higher AR order is the more precise the dynamical model would be, but requires more parameters to describe the model. Especially when the number of reference samples is limited, a feature extraction by the PCA will be difficult for a higher order AR model as the dimension of the vector space to be investigated is higher than that of the reference samples. Nevertheless, finding the suitable AR order before monitoring the bridge is troublesome. In this study, sensitivity analysis with respect to the AR order is carried out first. However, it is difficult to extend this approach to other bridges without information about damage. Therefore, for the practical health monitoring, it is recommended to examine several damage indicators according to different AR orders.

Figure 5.2 presents the sample means of the MD of the test samples and the CV samples obtained from the FV data of each scenario with respect to the AR order. Here, the dimension of the principal subspace

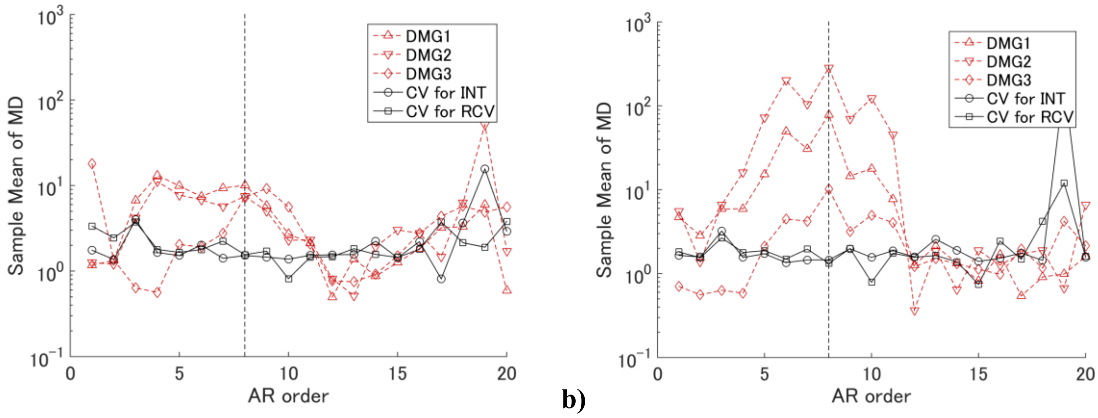

Figure 5.2 Sample means of MD with respect to AR orders: a) For WV data; b) For FV data.

q was fixed to 2, and demonstrated that the AR model that comprises 5 to 11 order is suitable for the damage detection. Therefore, in the following discussions, the AR order is fixed to 8, which gives maximum sample means of MDs for every damage scenario (see the vertical dashed lines in Figure 5.2). Note that this model selection procedure may introduce bias to the following hypothesis testing procedure since the AR order producing larger MDs is arbitrarily picked up. Unfortunately, the information criteria or stabilization diagrams mentioned in Chapter 3 are not feasible. That is because the AR orders sensitive to damage are not high enough for modal identification. This problem is possibly solved if sufficient amount of reference data is available since the PCA allows feature extraction on a subspace with higher degree of freedom so that anomalies in higher order AR models can be investigated.

5.3.2 Hypothesis testing

Plots of the T^2 statistics of the CV samples and test samples and their sample means in a logarithmic scale are depicted in Figure 5.3, where q is fixed to 2. For simplicity, the T^2 statistics lower than 0.1 are expelled from the diagrams in Figure 5.3. The expectation given as Eq. 5.23 and the critical values of the rejection regions given as Eq. 5.21 are also presented in the figure for the hypothesis test, where significance level α is set to 5%. That is, when the bridge is not damaged, only 5% of the T^2 statistics expected to exceed the critical value. Note that the critical values and expectations are slightly different between the CV samples and the test samples because of the number of the samples in their reference datasets. For every damage scenario, more than 5% of the T^2 statistics exceed the critical values and the sample means are located in the rejection region. On the other hand, for both scenarios of INT and RCV, no CV samples are in the rejection region. These results show the stochastic changes in the modal properties caused by damage are successfully detected by the proposed damage indicator. Figure 5.3b shows that the sensitivity of the T^2 statistics for DMG1 and DMG2 was improved considerably comparing to the results from WV data in Figure 5.3a. The sensitivity for DMG3 was also improved slightly. This observation showed that using free vibration data improves performance of the proposed damage detection method.

The first and second principal components of the polynomial coefficients that are obtained from both of WV and FV data are shown as presented in Figure 5.4, where the dataset obtained from the INT scenario is referred as the reference set and the dataset from the other scenarios are referred as the test set. Apparently, the principal components of each scenario formed groups. For example, the blue circles plotted in Figure 5.4, which is relevant to INT scenario were distinguished from every other scenario for both of WV data and FV data, which demonstrated that the changes in the modal properties attributable to severing and recovering the members of the bridge are well extracted using the AR model and PCA. Especially, the FV data caused smaller variation of the principal components from the INT scenario and more sensitive T^2 statistics for DMG1 and DMG2 than the WV data. Furthermore, apparently, the sample groups are mutually separated, especially in the FV data. It is noteworthy that the data measured from bridges under traffic during testing is still useful to detect damage even though the free vibration

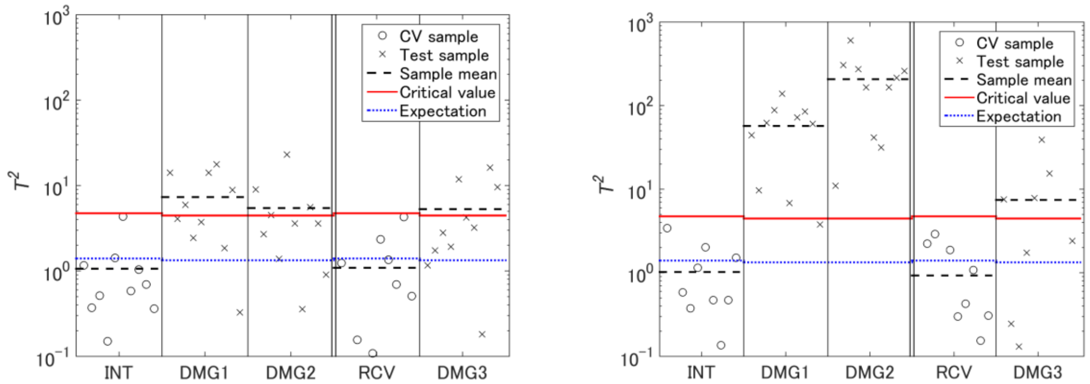

a) b)

Figure 5.3 The T^2 statistics: a) From WV data; b) From FV data.

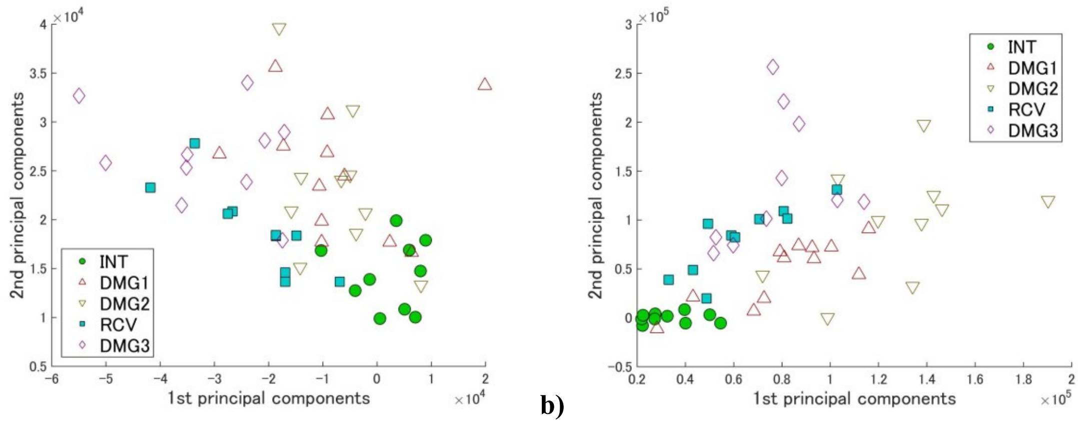

a) b)

Figure 5.4 The obtained principal components: a) From WV data; b) From FV data.

will provide better accuracy.

5.3.3 Comparison with existing studies

A brief description about the NDSF is given as follows in advance of making a comparison between the proposed damage indicator and NDSF. Let $y_k^{(l)}$ denote time series of local acceleration at l-th measurement point. Vibration data can be modeled using a univariate AR model described as the following equation, which is a univariate version of Eq. 5.1.

$$y_k^{(l)} = \sum_{i=1}^{p} a_i^{(l)} y_{k-i}^{(l)} + e_k^{(l)} \tag{5.24}$$

In that equation, $a_i^{(l)}$ denotes the i-th AR coefficient with respect to the l-th measurement point. Also, $e_k^{(l)}$ represents a white-noise time series. The AR coefficients are identified by solving the Yule–Walker equations derived from the univariate AR model. Each of the AR coefficients, especially the lower order AR coefficients, are presumed to include the modal information of the target structure. The following NDSF has therefore been investigated to detect bridge damage [55], [56].

$$d_l = \mathrm{abs}(a_1^{(l)}) / \sqrt{\sum_{i=1}^{3} a_i^{(l)}}. \tag{5.25}$$

Therein, d_l stands for the NDSF with respect to the l-th measurement point. The AR order p is determined by minimizing the following Akaike information criteria for the univariate AR model.

$$AIC = N\ln\left(2\pi\hat{\sigma}_p^2\right) + N + 2(p+1) \tag{5.26}$$

where $\hat{\sigma}_p^2$ is the variance of the noise term $e_k^{(l)}$ for AR model with p order.

Kim et al. [56] proposed to use MD to evaluate changes in NDSFs monitored on multiple measurement location. The feasibility of this MD is examined through damage experiment using an actual bridge in field [51]. In that experiment the measurement locations for producing MDs are divided into small groups to avoid bias appearing in MD with high degree of freedom. To compare NDSF with the proposed one,

Table 5.1 Sensor groups to calculate MD.

	A	B	C	D	E	F
Measurement Locations	A1 & A2	A2 & A3	A3 & A4	A4 & A5	A6 & A7	A7 & A8

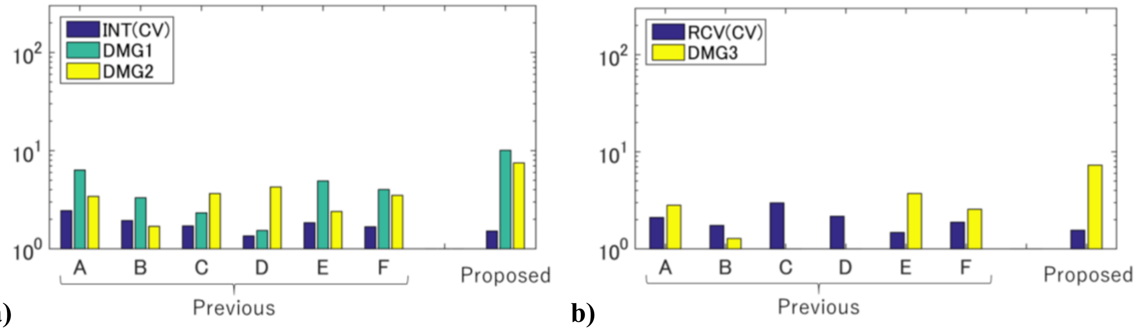

a) b)

Figure 5.5 Mean values of MDs for WV data: a) INT, DMG1, and DMG2; b) RCV and DMG3.

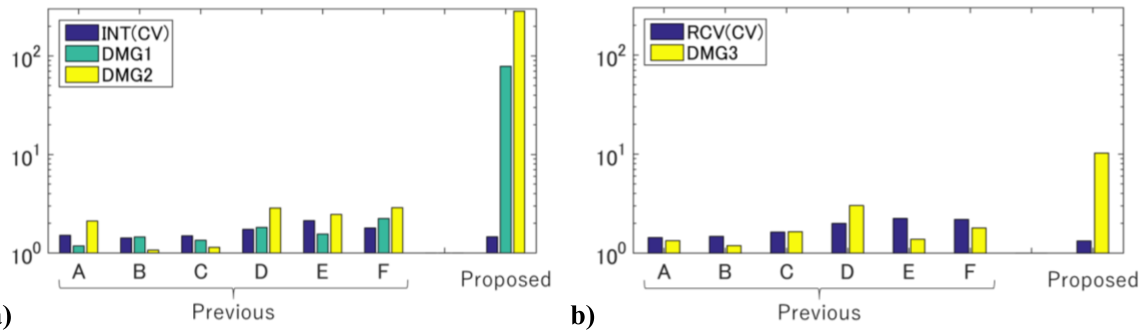

a) b)

Figure 5.6 Mean values of MDs for FV data: a) INT, DMG1, and DMG2; b) RCV and DMG3.

the measurement locations are divided into the six groups consisting of two locations as listed in Table 5.1 such as the existing study. Therein, the A1 to A8 represents sensor numbers in Figure 1.3c.

Figure 5.5 shows the mean values of the MDs calculated from the WV data both for the NDSFs and for the proposed damage sensitive features, where the results are depicted in a log scale and the values lower than 1 are ignored. Figure 5.6 shows the mean values of the MDs calculated from the FV data in the same way. Those diagrams show that the proposed method improves damage detection performance of the damage sensitive features for every damage scenario. For reference scenario, namely for INT and RCV, the proposed damage indicator stably produces low values. Especially, the FV shows considerable improvement for DMG1 and DMG2. Those observations demonstrate that the multivariate AR model enabled more reasonable feature extraction than univariate AR model. That is possibly because the multivariate model enables to describe spatial relationship between the measurement locations through the estimated modal response. The troubles involved in the sensor grouping also can be avoided in the proposed method. Although the proposed method shows advantages in multipoint measurement, the previous method appears still useful to single point measurement in practice.

5.4 Summary

This study proposed a damage detection method for a bridge structure using the novel damage indicator obtained from ambient vibrations of bridges. The damage indicator was derived from a multivariate autoregressive (AR) model to evaluate the stochastic distance between a set of reference samples obtained from healthy bridge and unknown test samples using the Mahalanobis distance (MD). Principal component analysis (PCA) was also applied to extract damage sensitive features from the AR model. Statistical hypothesis testing based on a probability distribution of the damage sensitive features was applied for damage detection using Hotelling's T^2 statistics. Field experiments were conducted on an actual steel truss bridge with truss members that were severed artificially to investigate feasibility of the proposed damage detection method.

Observations from sensitivity analysis showed that performance of the MD for damage detection depends on the AR order. The proposed damage detection method enabled detection of three damage patterns clearly. Especially using the free vibration data after the vehicle exits the bridge improved damage detection performance of the T^2 statistics. However, the forced vibration data are still useful because damage was also detected. The presented damage sensitive features were compared with the existing ones, named Nair's damage sensitive feature. The comparison demonstrated that the modal information included in a multivariate system might help to improve damage detection performance by the proposed method.

Although the proposed method shows advantages in multipoint measurement, the previous method appears still useful to single point measurement in practice. The proposed method also involve disadvantage in model selection, i.e., information criteria are not helpful to choose sensitive features. That is, the proposed method only enables to extract feature from roughly estimated mechanical model. This problem is tackled in Chapter 6 using Bayesian statistics.

Chapter 6

Bayes Factors

6.1 Introduction

The damage indicator mentioned in Chapter 5 requires feature extraction from the roughly estimated regressive parameters to reduce their uncertainties. Bayesian approach introduced in Chapter 2 possibly enables to handle those uncertainties directly by adopting a probability distribution function (PDF) for the parameters, according to the results given in Chapter 4. This chapter therefore introduces Bayesian statistics to investigate feasible damage indicator for bridge health monitoring. Furthermore, a more reasonable feature extraction method can be investigated based on the PDF for the parameters is investigated.

The multivariate autoregressive (AR) models spontaneously provide the expansion toward the Bayesian approach. This chapter thus investigates damage detection method by means of Bayesian statistics as follows: Firstly, the AR model provides a likelihood function for observed bridge accelerations, and thus the Bayesian inference method for the AR model provides the posterior distribution for the parameters composing the AR model. Accordingly, time series of acceleration acquired from a healthy bridge statistically provide a reference model describing the vibration of the healthy bridge. Secondly, Bayesian hypothesis test is formulated to distinguish whether a newly observed time series is acquired from healthy bridge or not. As a novel damage indicator, this study investigates a Bayes factor [86], that is, a ratio of marginal likelihood of two different hypotheses. One of the hypotheses represents the reference AR model produced from the vibration of the healthy bridge, and another one represents an uncertain AR model. When the modal properties of the bridge are changed due to damage, the Bayes factor will produce anomalies compared to the healthy condition.

This study provides two types of Bayes factors, namely, with and without feature extraction. The features are extracted as independent random variables based on the posterior distribution, which are presumably related to the modal properties of the bridge. Feasibility of the proposed method is discussed utilizing field experiment data mentioned in Section 1.4. The damage indicator investigated in Chapter 5 is also compared with the proposed Bayes factors.

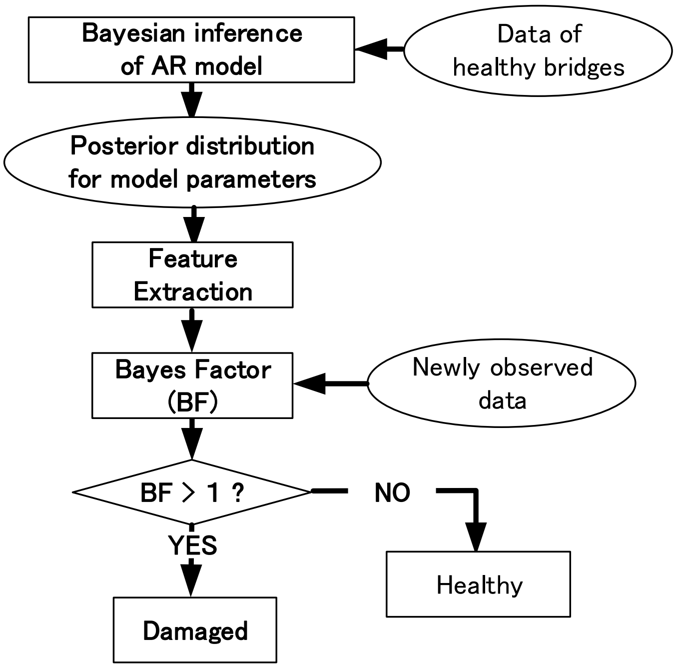

Figure 6.1 Flow of the Bayesian damage detection

6.2 Methodology

This study proposes a damage detection method with following two steps: Firstly, the posterior distribution for model parameters composing an AR model is determined by means of the Bayesian inference, by using dataset obtained from a bridge without damage. Secondly, Bayes factors calculated from newly observed data provide an indicator for damage detection according to the Bayesian hypothesis testing. Figure 6.1 shows the outline of the proposed damage detection method.

6.2.1 Bayesian inference

Suppose that synchronized time series of the acceleration are measured on a bridge at m measurement points. As discussed in Chapter 3 and Chapter 5, letting $\boldsymbol{y}_k \in \mathbb{R}^m$ denote a column vector at k-th time step of the discrete time series of measured acceleration, the following AR model with model order p approximates the time series obtained from a linear structural system excited by white noise.

$$\boldsymbol{y}_k = \sum_{i=1}^{p} \boldsymbol{\alpha}_i \boldsymbol{y}_{k-i} + \boldsymbol{e}_k \tag{6.1}$$

where, $\boldsymbol{\alpha}_i \in \mathbb{R}^{m\times m}$ denotes the i-th AR coefficient matrix and $\boldsymbol{e}_k \in \mathbb{R}^{m\times 1}$ denotes a white noise vector. Focusing on j-th row in Eq. 6.1, the following regressive model is obtained.

$$y_k^{(j)} = \sum_{i=1}^{p} \boldsymbol{\alpha}_i^{\{j\}} \boldsymbol{y}_{\boldsymbol{k-i}} + e_k^{(j)} \tag{6.2}$$

where, $y_k^{(j)}, e_k^{(j)} \in \mathbb{R}^1$ respectively represent j-th element of $\boldsymbol{y}_k$ and $\boldsymbol{e}_k$, and $\boldsymbol{\alpha}_i^{\{j\}} \in \mathbb{R}^{1\times m}$ represents j-th row of $\boldsymbol{\alpha}_i$. Assuming that elements in $\boldsymbol{e}_k$ are statistically independent each other and following the Gaussian distribution with expectation 0, $y_k^{(j)}$ also follows the Gaussian distribution with expectation $\sum_{i=1}^{p} \boldsymbol{\alpha}_i^{\{j\}} \boldsymbol{y}_{\boldsymbol{k-i}}$. Letting $t_k = y_k^{(j)}$, $\boldsymbol{w} = [\boldsymbol{\alpha}_1^{\{j\}}, \dots, \boldsymbol{\alpha}_P^{\{j\}}]^{\mathrm{T}} \in \mathbb{R}^{mP\times 1}$ and $\boldsymbol{x}_k = [\boldsymbol{y}_{k-1}{}^{\mathrm{T}}, \dots, \boldsymbol{y}_{k-p}{}^{\mathrm{T}}]^{\mathrm{T}} \in \mathbb{R}^{mp\times 1}$ for simplicity, probability distribution function (PDF) of t is given as follows.

$$\mathrm{p}(t_k|\boldsymbol{x}_k, \boldsymbol{w}, \beta) = \mathcal{N}(t_k|\boldsymbol{w}^T\boldsymbol{x}_k, \beta^{-1}) = \left(\frac{\beta}{2\pi}\right)^{\frac{1}{2}} \exp\left\{-\frac{\beta}{2}(t_k - \boldsymbol{w}^{\mathrm{T}}\boldsymbol{x}_k)^2\right\} \tag{6.3}$$

where, β represent the precision parameter of the regression, which is the inverse of the variance of the noise term $e_k^{(j)}$.

According to Eq. 6.3, the sequential algorithm using Bayesian inference for $\boldsymbol{w}$ and β is formulated as mentioned in Section 2.2.3. The discussion in Section 2.2.3 is summarized as follows. Assuming that independent and identically distributed (*iid*) n samples of $\boldsymbol{t}_k$ and $\boldsymbol{x}_k$ are observed and letting $\boldsymbol{t} = [t_1, \dots, t_n] \in \mathbb{R}^{n\times 1}$ and $\boldsymbol{X} = [\boldsymbol{x}_1 \ \dots \boldsymbol{x}_n]^{\mathrm{T}} \in \mathbb{R}^{n\times mp}$, the likelihood function for the parameters $\boldsymbol{w}$ and β is given as

$$\mathrm{p}(\boldsymbol{t}|\boldsymbol{w}, \beta) = \prod_{k=1}^{n} \mathcal{N}(t_k|\boldsymbol{w}^T\boldsymbol{x}_k, \beta^{-1}). \tag{6.4}$$

With the observed $\boldsymbol{t}$, the Bayes theorem provides the posterior joint PDF for $\boldsymbol{w}$ and β in the form of the following conditional PDF.

$$\mathrm{p}(\boldsymbol{w}, \beta|\boldsymbol{t}) = \mathrm{p}(\boldsymbol{t}|\boldsymbol{w}, \beta)\mathrm{p}(\boldsymbol{w}, \beta)\mathrm{p}(\boldsymbol{t})^{-1} \tag{6.5}$$

where $\mathrm{p}(\boldsymbol{w}, \beta)$ stands for a prior joint PDF for $\boldsymbol{w}$ and β. $\mathrm{p}(\boldsymbol{t})$ is a constant in manner of Bayesian inference, and therefore the posterior PDF $\mathrm{p}(\boldsymbol{w}, \beta|\boldsymbol{t})$ is obtained only from the observed data $\boldsymbol{t}$ and the prior PDF $\mathrm{p}(\boldsymbol{w}, \beta)$. The prior PDF is formulated as the following conjugate prior as mentioned in Section 2.2.3.

$$\mathrm{p}(\boldsymbol{w}, \beta) = \mathcal{N}(\boldsymbol{w}|\boldsymbol{m}, (\beta\boldsymbol{L})^{-1})Gam(\beta|a, b) \tag{6.6}$$

where, $\boldsymbol{L} \in \mathbb{R}^{D\times D}$ is a symmetric and positive definite matrix, $a > 0$ and $b > 0$. The parameters $\boldsymbol{m}$, $\boldsymbol{L}$, a and b are referred as hyperparameters, which determine the form of the PDF for the parameters $\boldsymbol{w}$ and β. According to the Bayes theorem given in Eq. 6.5, the following posterior PDF is obtained.

$$p(\boldsymbol{w}, \beta) = \mathcal{N}(\boldsymbol{w}|\boldsymbol{m}', (\beta\boldsymbol{L}')^{-1})Gam(\beta|a', b') \tag{6.7}$$

where,

$$\boldsymbol{L}' = \boldsymbol{L} + \boldsymbol{X}^{\mathrm{T}}\boldsymbol{X} \tag{6.8}$$

$$\boldsymbol{m}' = \boldsymbol{L}'^{-1}(\boldsymbol{L}\boldsymbol{m} + \boldsymbol{X}^{\mathrm{T}}\boldsymbol{t}) \tag{6.9}$$

$$a' = a + \frac{N}{2} \tag{6.10}$$

$$b' = b + \frac{1}{2}\|\boldsymbol{t} - \boldsymbol{X}\boldsymbol{m}'\|^2 + \frac{1}{2}(\boldsymbol{m}' - \boldsymbol{m})^{\mathrm{T}}\boldsymbol{L}(\boldsymbol{m}' - \boldsymbol{m}) \tag{6.11}$$

The sequential algorithm can be numerically realized by sequentially calculating hyperparameters given in Eqs. 6.8–6.11. In the first step of the sequential algorithm, the posterior PDF relevant to the non-informative prior is produced by substituting $[\boldsymbol{L}]_{ij} = 0\ \ (i, j = 1 \dots mp\ ), a = 0$ and $b = 0$ to Eqs. 6.8–6.11.

6.2.2 Hypothesis testing

Bayesian hypothesis test is conducted by assessing the Bayes factor, which is defined by a ratio of marginal likelihoods [57], [86], [87]. Assuming that dataset $\mathcal{D}$ is obtained from statistical hypothesis $\mathcal{H}$, the marginal likelihood for the hypothesis $\mathcal{H}$ is produced as

$$\mathrm{p}(\mathcal{D}|\mathcal{H}) = \int \mathrm{p}(\mathcal{D}|\boldsymbol{\theta}, \mathcal{H})\mathrm{p}(\boldsymbol{\theta}|\mathcal{H})\mathrm{d}\boldsymbol{\theta} \tag{6.12}$$

where $\boldsymbol{\theta}$ is a vector composed of parameters comprising the parametric model given by the hypothesis. Thus, $\mathrm{p}(\mathcal{D}|\boldsymbol{\theta}, \mathcal{H})$ and $\mathrm{p}(\boldsymbol{\theta}|\mathcal{H})$ respectively represents likelihood function for $\boldsymbol{\theta}$ under given dataset $\mathcal{D}$ and hypothesis $\mathcal{H}$ and prior distribution for $\boldsymbol{\theta}$ under hypothesis $\mathcal{H}$. According to the Bayes theorem, the posterior probability of the hypothesis is obtained as follows.

$$\Pr[\mathcal{H}|\mathcal{D}] = \mathrm{p}(\mathcal{D}|\mathcal{H})\Pr[\mathcal{H}]\,\mathrm{p}(\mathcal{D})^{-1} \tag{6.13}$$

where probabilities are denoted as $\Pr[\cdot]$ to distinguish from the PDFs, which are denoted as $\mathrm{p}(\cdot)$. Letting $\mathcal{H}_0$ and $\mathcal{H}_1$ are possible hypotheses, the odds is defined as $\Pr[\mathcal{H}_1]/\Pr[\mathcal{H}_0]$, i.e., the ratio of probabilities for the two hypotheses. Eq. 6.13 produces following relationship concerning the odds.

$$\frac{\Pr[\mathcal{H}_1|\mathcal{D}]}{\Pr[\mathcal{H}_0|\mathcal{D}]} = \frac{\Pr[\mathcal{H}_1]}{\Pr[\mathcal{H}_0]}B \tag{6.14}$$

where, B is the Bayes factor defined as a ratio of the marginal likelihoods, i.e.,

$$B = \frac{\mathrm{p}(\mathcal{D}|\mathcal{H}_1)}{\mathrm{p}(\mathcal{D}|\mathcal{H}_0)} \tag{6.15}$$

The relationship given in Eq. 6.14 enables to update the odds using dataset $\mathcal{D}$ to the odds posterior to observing the dataset. Assuming the prior probabilities are equivalent (i.e., $\Pr[\mathcal{H}_0] = \Pr[\mathcal{H}_1]$), the Bayes factor is correspond to the updated posterior odds. Therefore, the Bayes factor provides the indicator assessing whether observed data $\mathcal{D}$ supports the hypothesis $\mathcal{H}_0$ or the hypothesis $\mathcal{H}_1$.

Bayes factor for the AR model of vibrating bridges can be formulated based on the proposed Bayesian inference method. Let $\boldsymbol{t}_t$ represent a test sample of the time series of the target variables, which is observed for the hypothesis testing. From now on, let the set $\{\boldsymbol{t}_t, \boldsymbol{X}_t\}$ be referred as a test dataset where $\boldsymbol{X}_t$ represents input variables corresponding to the $\boldsymbol{t}_t$ as discussed in Section 6.2.1. Substituting Eq. 6.12 into Eq. 6.15 provides the following Bayes factor.

$$B = \frac{\mathrm{p}(\boldsymbol{t}_t|\mathcal{H}_1)}{\mathrm{p}(\boldsymbol{t}_t|\mathcal{H}_0)} = \frac{\iint \mathrm{p}(\boldsymbol{t}_t|\boldsymbol{w},\beta)\mathrm{p}(\boldsymbol{w},\beta|\mathcal{H}_1)\mathrm{d}\boldsymbol{w}\mathrm{d}\beta}{\iint \mathrm{p}(\boldsymbol{t}_t|\boldsymbol{w},\beta)\mathrm{p}(\boldsymbol{w},\beta|\mathcal{H}_0)\mathrm{d}\boldsymbol{w}\mathrm{d}\beta} \tag{6.16}$$

where, intervals of the integrals are whole domains for $\boldsymbol{w}$ and β. The likelihood function $\mathrm{p}(\boldsymbol{t}_t|\boldsymbol{w},\beta)$ is given in Eq 6.4. $\mathcal{H}_0$ denotes null hypothesis that provides undamaged evidence, and $\mathcal{H}_1$ denotes alternative hypothesis that provides damaged evidence. Kass and Raftery [86] suggested interpreting the Bayes factor on the natural logarithm scale. For example, if $2\ln B$ is over 10, then the evidence against null hypothesis H_0 is interpreted to be '*very strong*'. According to the scale suggested by Kass and Raftery, this study adopts $2\ln B$ as an evidence assessment index for anomaly detection.

Let $\mathcal{D}_r$ represents a reference dataset consisting of time series of acceleration observed from a bridge under healthy condition. That is, a set consisting of time series of target variables $\{\boldsymbol{t}_1, \boldsymbol{t}_2, \dots\}$ and the corresponding input variables $\{\boldsymbol{X}_1, \boldsymbol{X}_2, \dots\}$ are given as the reference dataset representing the healthy bridge. Accordingly, the hyperparameters $\boldsymbol{m}_r, \boldsymbol{L}_r, a_r$ and b_r composing the posterior distribution $\mathrm{p}(\boldsymbol{w},\beta|\mathcal{D}_r)$ are determined by Eqs. 6.8–6.11 and the non-informative prior. To formulate a hypothesis testing for damage detection, it is reasonable to adopt stochastic model of the bridge for the null hypothesis. The PDF complying with the null hypothesis is therefore modelled with respect to the reference dataset as

$$\mathrm{p}(\boldsymbol{w},\beta|\mathcal{H}_0) = \mathrm{p}(\boldsymbol{w},\beta|\mathcal{D}_r) = \mathcal{N}(\boldsymbol{w}|\boldsymbol{m}_r, \beta^{-1}\boldsymbol{L}_r^{-1})Gam(\beta|a_r, b_r) \tag{6.17}$$

Eqs. 6.4 and 6.17 lead to the marginal likelihood for $\mathcal{H}_0$ as follows in log scale (see also Appendix).

$$\begin{aligned} \ln p(\boldsymbol{t}_t|\mathcal{H}_0) &= \ln \iint p(\boldsymbol{t}_t|\boldsymbol{w},\beta)p(\boldsymbol{w},\beta|\mathcal{D}_r)\mathrm{d}\boldsymbol{w}\mathrm{d}\beta \\ &= \frac{1}{2}\ln\frac{|\boldsymbol{L}_r|}{|\boldsymbol{L}_r'|} - a_r' \ln b_r' + a_r \ln b_r + \ln\frac{\Gamma(a_r')}{\Gamma(a_r)} - \frac{n_t}{2}\ln 2\pi \end{aligned} \tag{6.18}$$

where, n_t stands for the sample size of the time series $\boldsymbol{t}_\mathrm{t}$, and $\boldsymbol{L}_r'$, a_r' and b_r' are hyperparameters representing $\mathrm{p}(\boldsymbol{w},\beta|\mathcal{D}_r, \boldsymbol{t}_\mathrm{t})$, i.e., the posterior PDF updated by the $\boldsymbol{t}_\mathrm{t}$ from the prior PDF $\mathrm{p}(\boldsymbol{w},\beta|\mathcal{D}_r)$ using Eqs. 6.8–6.11. Supposing a_r is large enough, Eq. 6.18 is asymptotically approximated as follows (see also Section 6.2.3).

$$\ln p(\boldsymbol{t}_t|\mathcal{H}_0) = \frac{1}{2}\ln\frac{|\boldsymbol{L}_r|}{|\boldsymbol{L}_r'|} + a_r' \ln\frac{a_r'}{b_r'} - a_r \ln\frac{a_r}{b_r} - \frac{1}{2}\ln\frac{a_r'}{a_r} - \frac{n_t}{2}\ln 2\pi e + O\left(\frac{1}{a_r}\right) \tag{6.19}$$

Bayes factor without feature extraction

An exact PDF for the parameters representing damaged bridge is undefinable because of uncertainty of damage itself. It is reasonable to adopt a broad prior PDF to describe uncertain changes in the parameters. Kass and Raftery [86], [87] mentioned that the Schwarz criterion [57], [88] can be applied as a standard procedure when the priors are hard to predefined precisely, since the Schwarz criterion can be formulated as roughly-approximated marginal likelihood according to the broad prior PDF. If all of the parameters are assumed uncertain under the alternative hypothesis, then natural logarithm of the marginal likelihood for $\mathcal{H}_1$ is approximated by the Schwarz criterion as follows.

$$\begin{aligned}\ln \mathrm{p}(\boldsymbol{t}_t|\mathcal{H}_1) &\cong \ln \mathrm{p}\left(\boldsymbol{t}_t\middle|\widehat{\boldsymbol{w}}_t,\hat{\beta}_t\right) - \frac{1}{2}(mp+1)\ln n_t \\ &= \frac{n_t}{2}(\ln \hat{\beta}_t - \ln 2\pi - 1) - \frac{1}{2}(mp+1)\ln n_t\end{aligned} \tag{6.20}$$

where $\widehat{\boldsymbol{w}}_t$ and $\hat{\beta}_{\mathrm{t}}$ represent maximum likelihood estimators with respect to the test dataset. Thus, the scaled Bayes factor is given as

$$2\ln B = n_t \ln \hat{\beta}_t - \ln\frac{|\boldsymbol{L}_r|}{|\boldsymbol{L}'_r|} - 2a'_r \ln\frac{a'_r}{b'_r} + 2a_r \ln\frac{a_r}{b_r} - \ln\frac{a'_r}{a_r} - (mp+1)\ln n_t \tag{6.21}$$

Note that the Bayes factor is numerically obtainable only from the reference and test datasets. The computation is realized only by means of basic algebraic operations (see also Section 6.2.3). Let the Bayes factor provided as Eq. 6.21 be named as "BFver.1".

From one time series, *m* Bayes factors are obtainable since each of the measurement points provides their regressive models (see Eq. 6.2). Assuming each of the Bayes factors is independent, the product of those Bayes factors represents the Bayes factor for the whole observation. That is, letting $B^{(j)}$ represent Bayes factors obtained from the *j*-th measurement point the Bayes factor for whole observation B_w is defined as

$$2\ln B_w = \sum_{j=1}^{m} 2\ln B^{(j)} \ . \tag{6.22}$$

Hereafter B_w given in Eq. 6.22 is named as the "global Bayes factor", and let $B^{(j)}$ relevant to each of the measurement points is named as the "local Bayes factor" to avoid confusion.

Bayes factor with feature extraction

The Bayes factor defined in Eq. 6.22 will indicates the stochastic changes in any of the parameters. However, some of the AR coefficients are composed of parameters irrelevant to modal properties of the bridges as discussed in Chapter 3 and Chapter 4. Thus, it is desirable that the alternative hypothesis is related to damage sensitive features of a bridge. This study proposes damage sensitive features based on the posterior distribution for the reference dataset $\mathcal{D}_r$.

Since the matrix $\boldsymbol{L}_r$ is real, symmetric and positive definite, its singular value decomposition (SVD) is given as

$$\boldsymbol{L}_r = \boldsymbol{U}\tilde{\boldsymbol{L}}\boldsymbol{U}^{\mathrm{T}} = [\boldsymbol{U}_1 \ \ \boldsymbol{U}_2]\begin{bmatrix} \tilde{\boldsymbol{L}}_1 & \boldsymbol{O} \\ \boldsymbol{O} & \tilde{\boldsymbol{L}}_2 \end{bmatrix}\begin{bmatrix} \boldsymbol{U}_1^{\mathrm{T}} \\ \boldsymbol{U}_2^{\mathrm{T}} \end{bmatrix} \tag{6.23}$$

where, $\tilde{\boldsymbol{L}} \in \mathbb{R}^{mp\times mp}$ is the diagonal matrix consisting of the singular values in a descending order and $\boldsymbol{U} \in \mathbb{R}^{mp\times mp}$ is the orthogonal matrix consisting of the singular vectors. $\tilde{\boldsymbol{L}}_1 \in \mathbb{R}^{q\times q}$ and $\boldsymbol{U}_1 \in \mathbb{R}^{mp\times q}$ respectively represent the q largest singular values and the corresponding singular vectors; $\tilde{\boldsymbol{L}}_2$ and $\boldsymbol{U}_2$ represent the other singular values and singular vectors. Let $\tilde{\boldsymbol{w}}$ denote the orthogonal transformation of $\boldsymbol{w}$ such that $\tilde{\boldsymbol{w}} = \boldsymbol{U}^{\mathrm{T}}\boldsymbol{w}$, and let $\tilde{\boldsymbol{w}}_1$ and $\tilde{\boldsymbol{w}}_2$ respectively denote components of $\tilde{\boldsymbol{w}}$ such that $\tilde{\boldsymbol{w}}_1 = \boldsymbol{U}_1^{\mathrm{T}}\boldsymbol{w}$ and $\tilde{\boldsymbol{w}}_2 = \boldsymbol{U}_2^{\mathrm{T}}\boldsymbol{w}$. Then Eq. 6.17 can be rewritten in the form of the posterior distribution of $\tilde{\boldsymbol{w}}_1, \tilde{\boldsymbol{w}}_2$ and β as follows.

$$\begin{aligned} \mathrm{p}(\tilde{\boldsymbol{w}}, \beta|\mathcal{D}_r) &= \mathcal{N}\left(\tilde{\boldsymbol{w}}\middle|\tilde{\boldsymbol{m}}, \beta^{-1}\tilde{\boldsymbol{L}}^{-1}\right)\mathrm{Gam}(\beta|a_r, b_r) \\ &= \mathcal{N}\left(\tilde{\boldsymbol{w}}_1\middle|\tilde{\boldsymbol{m}}_1, \beta^{-1}\tilde{\boldsymbol{L}}_1^{-1}\right)\mathcal{N}\left(\tilde{\boldsymbol{w}}_2\middle|\tilde{\boldsymbol{m}}_2, \beta^{-1}\tilde{\boldsymbol{L}}_2^{-1}\right)\mathrm{Gam}(\beta|a_r, b_r) \end{aligned} \tag{6.24}$$

where, $\tilde{\boldsymbol{m}} = \boldsymbol{U}^{\mathrm{T}}\boldsymbol{m}_r$, $\tilde{\boldsymbol{m}}_1 = \boldsymbol{U}_1^{\mathrm{T}}\boldsymbol{m}_r$ and $\tilde{\boldsymbol{m}}_2 = \boldsymbol{U}_2^{\mathrm{T}}\boldsymbol{m}_r$. From the Bayesian viewpoint, the uncertainty of the parameters is expressed through the posterior distribution. In the posterior distribution, the parameter $\tilde{\boldsymbol{w}}_1$ has less variances than the $\tilde{\boldsymbol{w}}_2$, hence the $\tilde{\boldsymbol{w}}_1$ represents the parametric subspace that is certainly inferable from the observation. This study presumes the $\tilde{\boldsymbol{w}}_1$ is related to modal properties of bridges and conducts hypothesis testing to detect stochastic changes in the $\tilde{\boldsymbol{w}}_1$.

The alternative hypothesis represents that the parameters contained in $\tilde{\boldsymbol{w}}_1$ change due to damage, by adopting a broad prior PDF for $\tilde{\boldsymbol{w}}_1$. This study adopts covariance matrix $n_r\beta^{-1}\boldsymbol{S}_1^{-1}$ for $\tilde{\boldsymbol{w}}_1$ to describe the broad prior. Therein n_r denotes number of the target variables in the reference dataset. The other parameters except $\tilde{\boldsymbol{w}}_1$ are not altered from the null hypothesis. In this case, the prior can be formulated as following PDF.

$$\mathrm{p}(\tilde{\boldsymbol{w}}, \beta|\mathcal{H}_1) = \mathcal{N}\left(\tilde{\boldsymbol{w}}_1\middle|\tilde{\boldsymbol{m}}_1, n_r\beta^{-1}\tilde{\boldsymbol{L}}_1^{-1}\right)\mathcal{N}\left(\tilde{\boldsymbol{w}}_2\middle|\tilde{\boldsymbol{m}}_2, \beta^{-1}\tilde{\boldsymbol{L}}_2^{-1}\right)\mathrm{Gam}(\beta|a_r, b_r) \tag{6.25}$$

Note that the formulation in Eq. 6.25 does not require any approximation such as the Schwarz criterion. According to Eq. 6.25, the marginal likelihood is given as

$$\ln p(\boldsymbol{t}_t|\mathcal{H}_1) = \frac{1}{2}\ln\frac{|\boldsymbol{L}_{alt}|}{|\boldsymbol{L}'_{alt}|} + a_r \ln b_r - a'_r \ln b'_{alt} + \ln\frac{\Gamma(a'_r)}{\Gamma(a_r)} - \frac{n_t}{2}\ln 2\pi \tag{6.26}$$

where

$$\tilde{\boldsymbol{L}}_{alt} = \begin{bmatrix} \frac{1}{n_r}\tilde{\boldsymbol{L}}_1 & \boldsymbol{O} \\ \boldsymbol{O} & \tilde{\boldsymbol{L}}_2 \end{bmatrix} \tag{6.27}$$

$$\tilde{\boldsymbol{L}}'_{alt} = \tilde{\boldsymbol{L}}_{alt} + \boldsymbol{U}^{\mathrm{T}}\boldsymbol{X}_t^{\mathrm{T}}\boldsymbol{X}_t\boldsymbol{U} \tag{6.28}$$

$$\tilde{\boldsymbol{m}}' = \tilde{\boldsymbol{L}}'^{-1}_{alt}(\tilde{\boldsymbol{L}}_{alt}\tilde{\boldsymbol{m}} + \boldsymbol{U}^{\mathrm{T}}\boldsymbol{X}_t^{\mathrm{T}}\boldsymbol{t}_t) \tag{6.29}$$

$$b'_{alt} = b_r + \frac{1}{2}\|\boldsymbol{t}_t - \boldsymbol{X}_t\boldsymbol{U}\tilde{\boldsymbol{m}}'\|^2 + \frac{1}{2}(\tilde{\boldsymbol{m}}' - \tilde{\boldsymbol{m}})^{\mathrm{T}}\tilde{\boldsymbol{L}}_{alt}(\tilde{\boldsymbol{m}}' - \tilde{\boldsymbol{m}}). \tag{6.30}$$

Thus, the scaled local Bayes factors are given as

$$2\ln B = \ln\frac{|\boldsymbol{L}'_r|}{|\tilde{\boldsymbol{L}}'_{alt}|} + 2a'_r\ln\frac{b'_r}{b'_{alt}} - q\ln n_r \tag{6.31}$$

The Bayes factor provided as Eq. 6.31 is named as "BFver.2". The global Bayes factor for BFver.2 can be defined just in the same way as Eq. 6.22.

6.2.3 Computational strategies

Aiming at fast and robust computation, auto-correlation functions are introduced for the Bayesian inference. Letting $R(s)$ denotes estimator of auto-correlation function of $\boldsymbol{y}_k$ $(k = 1, \ldots, n)$, i.e.,

$$\boldsymbol{R}(s) = \frac{1}{n}\Sigma_{k=1+s}^{n}(\boldsymbol{y}_k\boldsymbol{y}_{k-s}{}^{\mathrm{T}}) \ \ (s > 0) \tag{6.32}$$

Assuming $\boldsymbol{y}_k = 0$ for $k < 0$ and $n < k$, following relationships are obtained.

$$\boldsymbol{X}^{\mathrm{T}}\boldsymbol{X} = \sum_{k=1}^{n}\begin{bmatrix}\boldsymbol{y}_{k-1}\\ \vdots \\ \boldsymbol{y}_{k-p}\end{bmatrix}\left[\boldsymbol{y}_{k-1}{}^{\mathrm{T}}, \ldots, \boldsymbol{y}_{k-p}{}^{\mathrm{T}}\right] \tag{6.33}$$

$$= n\begin{bmatrix}\boldsymbol{R}(0) & \boldsymbol{R}(1) & \cdots & \boldsymbol{R}(p-1)\\ \boldsymbol{R}(1)^{\mathrm{T}} & \boldsymbol{R}(0) & \cdots & \boldsymbol{R}(p-2)\\ \vdots & \vdots & \ddots & \vdots \\ \boldsymbol{R}(p-1)^{\mathrm{T}} & \boldsymbol{R}(p-2)^{\mathrm{T}} & \cdots & \boldsymbol{R}(0)\end{bmatrix}$$

$$\boldsymbol{X}^{\mathrm{T}}\boldsymbol{T} = \sum_{k=1}^{n}\begin{bmatrix}\boldsymbol{y}_{k-1}\\ \vdots \\ \boldsymbol{y}_{k-p}\end{bmatrix}\boldsymbol{y}_k{}^{\mathrm{T}} = n\begin{bmatrix}\boldsymbol{R}(1)^{\mathrm{T}}\\ \boldsymbol{R}(2)^{\mathrm{T}}\\ \vdots \\ \boldsymbol{R}(p)^{\mathrm{T}}\end{bmatrix} \tag{6.34}$$

$$\boldsymbol{T}^{\mathrm{T}}\boldsymbol{T} = \sum_{k=1}^{n}\boldsymbol{y}_k\boldsymbol{y}_k{}^{\mathrm{T}} = n\boldsymbol{R}(0) \tag{6.35}$$

where $\boldsymbol{T} = [\boldsymbol{y}_1, \ldots, \boldsymbol{y}_n]^{\mathrm{T}}$, i.e., a matrix composed of target variables on all measurement points. Letting the reference dataset contain target variables $\{\boldsymbol{T}_1, \boldsymbol{T}_2, \ldots, \boldsymbol{T}_l\}$ and input variables $\{\boldsymbol{X}_1, \boldsymbol{X}_2, \ldots, \boldsymbol{X}_l\}$, and letting $n_1, \ldots, n_l$ denote the data length of the each samples, Eqs. 6.8-6.11 and the noninformative prior lead the following hyperparameters.

$$\boldsymbol{L}_r = \Sigma_{i=1}^{l}\boldsymbol{X}_i^{\mathrm{T}}\boldsymbol{X}_i \tag{6.36}$$

$$\boldsymbol{M}_r = \boldsymbol{L}_r^{-1}\ (\Sigma_{i=1}^{l}\boldsymbol{X}_i^{\mathrm{T}}\boldsymbol{T}_i) \tag{6.37}$$

$$a_r = \frac{1}{2}\Sigma_{i=1}^{l}n_i = \frac{1}{2}n_r \tag{6.38}$$

$$\boldsymbol{b}_r = \frac{1}{2}\left(\mathrm{diag}\left(\Sigma_{i=1}^{l}\boldsymbol{T}_i^{\mathrm{T}}\boldsymbol{T}_i\right) - \mathrm{diag}(\boldsymbol{M}_r^{\mathrm{T}}\boldsymbol{L}_r\boldsymbol{M}_r)\right) \tag{6.39}$$

where $\boldsymbol{M}_r \in \mathbb{R}^{mp\times m}$ and $\boldsymbol{b}_r \in \mathbb{R}^{m}$ respectively represent a matrix whose column vectors are consisting of $\boldsymbol{m}_r$ and a vector consisting of b_r relevant to each of the measurement points. Eq. 6.36 shows that the SVD given in Eq. 6.23 provides principal component analysis for the vectors $\boldsymbol{x}$ contained in reference dataset because $\boldsymbol{L}_r$ is related to the covariance matrix of $\boldsymbol{x}$. Accordingly, the updated hyperparameters are given just adding the newly observed $\boldsymbol{X}_t^{\mathrm{T}}\boldsymbol{X}_t$, $\boldsymbol{X}_t^{\mathrm{T}}\boldsymbol{T}_t$, $\boldsymbol{T}_t^{\mathrm{T}}\boldsymbol{T}_t$ and n_t to the summation part appearing in Eqs. 6.36-6.39.

To compute the Bayes factors, the gamma functions and the determinants should be properly manipulated since they are sometimes so huge that it can lead to the arithmetic overflows. Fortunately, the log scale enables robust computation as follows. Firstly, the log-scaled gamma function $\ln\Gamma(\cdot)$ is given for large x as

$$\ln\Gamma(x) = \left(x - \frac{1}{2}\right)\ln x - x + \frac{1}{2}\ln 2\pi + O\left(\frac{1}{x}\right) \tag{6.40}$$

where x is a positive real number, and $O(\cdot)$ denotes the asymptotic notation [89]. In this study, the hyperparameter a_r is presumably large enough since the sample size of the reference dataset corresponds to the sample size of the measured time series as the reference. Thus, the gamma functions appearing in Eq. 6.21 are approximated as

$$\ln\frac{\Gamma(a_r')}{\Gamma(a_r)} = a_r'\ln a_r' - a_r\ln a_r - \frac{1}{2}\ln\frac{a_r'}{a_r} - \frac{1}{2}n_t + O\left(\frac{1}{a_r}\right) \tag{6.41}$$

Secondly, the determinant of a matrix can be expanded as the product of eigenvalues consisting the matrix. Thus, the determinant part appearing in Eq. 6.21 is expanded as

$$\begin{aligned} -\ln\frac{|\boldsymbol{L}_r|}{|\boldsymbol{L}_r'|} &= \ln\left|\boldsymbol{L}_r'\boldsymbol{L}_r^{-1}\right| = \ln\left|\boldsymbol{I} + \boldsymbol{X}_t^{\mathrm{T}}\boldsymbol{X}_t\boldsymbol{L}_r^{-1}\right| = \ln\prod_{i=1}^{mp}\mathrm{eig}_i(\boldsymbol{I} + \boldsymbol{X}_t^{\mathrm{T}}\boldsymbol{X}_t\boldsymbol{L}_r^{-1}) \\ &= \sum_{i=1}^{mp}\ln\mathrm{eig}_i(\boldsymbol{I} + \boldsymbol{X}_t^{\mathrm{T}}\boldsymbol{X}_t\boldsymbol{L}_r^{-1}) = \sum_{i=1}^{mp}\ln\left(1 + \mathrm{eig}_i(\boldsymbol{X}_t^{\mathrm{T}}\boldsymbol{X}_t\boldsymbol{L}_r^{-1})\right) \end{aligned} \tag{6.42}$$

where $\mathrm{eig}_i(\cdot)$ denotes i-th eigenvalue of a matrix. For Eq. 6.31, the determinant part is given as follows considering q eigenvalues relevant to the feature extraction.

$$\begin{aligned} \ln\frac{|\boldsymbol{L}_r'|}{|\tilde{\boldsymbol{L}}_{alt}'|} &= \ln\left|\boldsymbol{L}_r'\tilde{\boldsymbol{L}}_{alt}'^{-1}\right| = \ln\left|\left(\frac{n_r-1}{n_r}\begin{bmatrix}\tilde{\boldsymbol{L}}_1 & \boldsymbol{O}\\ \boldsymbol{O} & \boldsymbol{O}\end{bmatrix} + \tilde{\boldsymbol{L}}_{alt}'\right)\tilde{\boldsymbol{L}}_{alt}'^{-1}\right| \\ &\approx \ln\left|\begin{bmatrix}\boldsymbol{I}_q\\ \boldsymbol{O}\end{bmatrix}\tilde{\boldsymbol{L}}_1[\boldsymbol{I}_q \quad \boldsymbol{O}]\tilde{\boldsymbol{L}}_{alt}'^{-1} + \boldsymbol{I}_{mp}\right| = \ln\left|\tilde{\boldsymbol{L}}_1[\boldsymbol{I}_q \quad \boldsymbol{O}]\tilde{\boldsymbol{L}}_{alt}'^{-1}\begin{bmatrix}\boldsymbol{I}_q\\ \boldsymbol{O}\end{bmatrix} + \boldsymbol{I}_q\right| \end{aligned} \tag{6.43}$$

$$= \sum_{i=1}^{q} \ln\left(1 + \mathrm{eig}_i\left(\tilde{\boldsymbol{L}}_1[\boldsymbol{I}_q \quad \boldsymbol{O}]\tilde{\boldsymbol{L}}_{alt}'^{-1}\begin{bmatrix}\boldsymbol{I}_q \\ \boldsymbol{O}\end{bmatrix}\right)\right)$$

6.3 Relationship with Existing Methodologies

The proposed Bayes factors are compared to a conventional hypothesis testing. Suppose that infinite sample size is given in the reference dataset, i.e., a limit such that $n_r \to \infty$ is under consideration. Now, assume that the input variables are *iid* for both of the reference and the test datasets, and that the following covariance matrix is exists.

$$\boldsymbol{\Sigma}_x = \mathrm{Cov}[\boldsymbol{x}]. \tag{6.44}$$

The central limit theorem justifies following asymptotic approximations.

$$\boldsymbol{L}_r = \Sigma_{i=1}^{\boldsymbol{l}} \boldsymbol{X}_i^{\mathrm{T}}\boldsymbol{X}_i \approx n_r \boldsymbol{\Sigma}_x \tag{6.45}$$

$$\boldsymbol{X}_t^{\mathrm{T}}\boldsymbol{X}_t \approx n_t \boldsymbol{\Sigma}_x. \tag{6.46}$$

Accordingly, the updated hyperparameter $\boldsymbol{m}_r'$ is approximated as

$$\boldsymbol{m}_r' = \boldsymbol{L}_r'^{-1}(\boldsymbol{L}_r\boldsymbol{m}_r + \boldsymbol{X}_r^{\mathrm{T}}\boldsymbol{t}_r) = \boldsymbol{m}_r + \ O\left(\frac{n_t}{n_r}\right). \tag{6.47}$$

As $n_r \to \infty$, the $O(n_t/n_r)$ is supposed to be ignored. Thus,

$$b_r' \approx b_r + \frac{1}{2}E(\boldsymbol{m}_r). \tag{6.48}$$

Since $\ln\frac{|\boldsymbol{L}_r|}{|\boldsymbol{L}_r'|} = O\left(\frac{n_t}{n_r}\right)$ and $\ln\frac{a_r'}{a_r} = O\left(\frac{n_t}{n_r}\right)$, Eq. 6.19 leads to the following approximation.

$$\begin{aligned}\ln p(\boldsymbol{t}_t|\mathcal{H}_0) &\approx a_r' \ln\frac{a_r'}{b_r'} - a_r \ln\frac{a_r}{b_r} - \frac{n_t}{2}\ln 2\pi e \\ &\approx a_r' \ln\hat{\beta}_r - a_r \ln\hat{\beta}_r - \frac{n_t}{2}\ln 2\pi + a_r' \ln\frac{a_r'}{a_r + 1/2\hat{\beta}_r E(\boldsymbol{m}_r)} - \frac{n_t}{2} \\ &\approx \frac{n_t}{2}\ln\frac{\hat{\beta}_r}{2\pi} - \frac{1}{2}\hat{\beta}_r E(\boldsymbol{m}_r) = \ln p\big(\boldsymbol{t}_t|\boldsymbol{m}_r, \hat{\beta}_r\big)\end{aligned} \tag{6.49}$$

where $\hat{\beta}_r = a_r/b_r$ corresponds to the maximum likelihood estimator of the precision parameter with respect to the reference data. Eq. 6.49 shows that the limit $n_r \to \infty$ provides the null hypothesis whose parameters are exactly fixed to the maximum likelihood estimators derived from the reference dataset. Note that $\boldsymbol{m}_r$ is the maximum likelihood of $\boldsymbol{w}$.

Here, the BFver.1 is considered for simplicity. then Eq. 6.49 leads the Bayes factor to the following relationship.

$$2 \ln B \approx 2 \ln \Lambda - (mp + 1) \ln n_t \tag{6.50}$$

Here, Λ denotes the following likelihood ratio

$$\Lambda = \frac{p(\boldsymbol{t}_t | \widehat{\boldsymbol{w}}_t, \widehat{\beta}_t)}{p(\boldsymbol{t}_t | \boldsymbol{m}_r, \widehat{\beta}_r\ )} = \frac{\sup_{\boldsymbol{w},\beta}\{p(\boldsymbol{t}_t | \boldsymbol{w}, \beta)\}}{p(\boldsymbol{t}_t | \boldsymbol{m}_r, \widehat{\beta}_r\ )} \tag{6.51}$$

According to the Wilks' theorem [90], the PDF of the statistic $(2 \ln \Lambda)$ asymptotically equals to χ^2 distribution as the test dataset $\{\boldsymbol{t}_t, \boldsymbol{X}_t\}$ is *iid* to the reference dataset and the sample size n_t approaches ∞. The degrees of freedom of the χ^2 distribution equal to the difference in dimensions of the free parameters in the likelihood function. For instance, the likelihood ratio in Eq. 6.51 provides $(2 \ln \Lambda)$ which follows χ^2 distribution of $(mp + 1)$ degree of freedom. The statistic $(2 \ln \Lambda)$ is therefore classically regarded as a test statistic for a hypothesis testing to find whether each of the samples of the $\boldsymbol{t}_t$ follows $p(t | \boldsymbol{m}_r, \hat{\beta}_r)$; this hypothesis testing is referred as likelihood ratio test. The Neyman-Pearson lemma states that the likelihood ratio test provides the most powerful test among for any significance levels on which probability of the Type I error is considered tolerable. However, in practice, the likelihood ratio test often leads to the Type I error rather than the given significance level. That is because the hypothesis test requires that the parameter $\boldsymbol{w}$ and β are fixed to the specific constants, though it is almost impossible to find exact parameters only from an estimation. Thus, the significance level does not always ensure a reliable rejection of the null hypothesis. This problem causes practical difficulties on decision-making; false alert may occur more frequently than the designed significance level even though the bridge is not damaged.

The proposed Bayes factors therefore provide following two benefits: Firstly, the Bayes factors possibly provide results such that support the null hypothesis when the bridge is not damaged. For instance, the asymptotical relationship given in Eq. 6.50 leads following expectation according to the Wilks' theorem.

$$\mathbb{E}[2 \ln B] \approx \mathbb{E}[2 \ln \Lambda] - (mp + 1) \ln n_t = -(mp + 1) \ln \frac{n_t}{e} \tag{6.52}$$

In other words, supposing the test dataset exactly follows $p(t | \boldsymbol{m}_r, \hat{\beta}_r)$, the Bayes factor is expected to support the null hypothesis. Secondly, the proposed Bayes factors enable to handle the uncertainty of the parameters. The null hypothesis does not require infinite reference samples to give an exact estimation of the parameters, and thus the proposed method presumably considers the uncertainty involved in the reference data.

6.4 Case Studies

Here, the target bridge introduced in Section 1.4 is investigated as in Chapter 5. For simplicity, only the WV data is under investigated in the following discussion. This chapter also considers a case such that passing vehicle speed is altered, i.e., not only INT40 scenario but also INT30 and INT50 scenarios are investigated.

6.4.1 Preliminary investigation

In advance of the hypothesis testing, the AR order p and the number of the damage sensitive features q should be predefined. The orders are determined by following steps: Firstly, assuming all of the parameters are uncertain, the Schwarz criterion evaluates the relevant AR orders using the reference dataset. The AR order providing the highest Schwarz criterion is adopted as the p for the hypothesis testing. The Schwarz criterion is easily calculated using hyperparameters of the posterior PDF $\mathrm{p}(\boldsymbol{w}, \beta|\mathcal{D}_r)$ as

$$\begin{aligned}\ln \mathrm{p}(\mathcal{D}_r) &\cong \ln \mathrm{p}\left(\mathcal{D}_r \middle| \boldsymbol{m}_r, \hat{\beta}_r\right) - \frac{1}{2}(mp+1)\ln n_r \\ &= \frac{n_r}{2}\left(\ln \frac{n_r}{2b_r} - \ln 2\pi e\right) - \frac{1}{2}(mp+1)\ln n_r.\end{aligned} \tag{6.53}$$

Here, b_r is derived from the auto-correlation functions. Secondly, using the hyperparameters reproduced by the AR model with the p-th order, the q is determined by stabilization diagram.

From now on, supposing the INT40 scenario provides reference dataset, the p and the q are investigated. Figure 6.2 shows Schwarz criteria for every measurement points. Note that those Schwarz criteria correspond to the inverse of Bayesian information criteria given in Figure 3.1. Thus, according to the discussion given in Chapter 3, the proper model order is determined by observing the slope of the Schwarz criteria. The criteria appear almost converged with p=20. However, they slightly increase while they approach to around p=150. This observation shows that most of the signal can be explained by the 20 order model, although the higher order model gives more precise regression. The discussions in Chapter 3

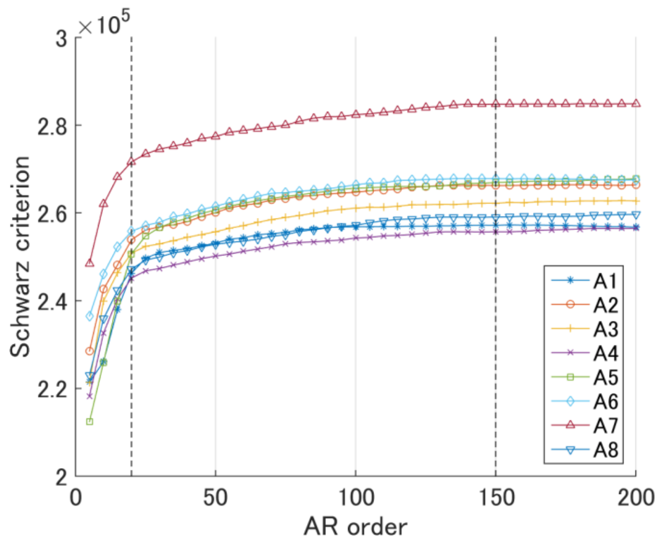

Figure 6.2 The Schwarz criteria with respect to the AR orders.

indicate that the higher order AR model contains unwanted spurious poles in their transfer function coefficients such that identification of the modal properties is getting troublesome. However, the higher order model is still worth to be investigated for the feature extraction. That is because a precise model are expected to lead reliable features as well as the stochastic subspace identification (SSI). Therefore, this study investigate both of the lower order model (p=20) and the higher order model (p=150). The AR orders p=20 and p=150 are respectively depicted by the dashed line in Figure 6.2.

To find reasonable singular value order q for the feature extraction, this study proposes following procedure using stabilization diagrams: Firstly, find the posterior distribution from reference dataset for a specific AR order. Secondly, reproduce the AR model consisting of only most probable values of the damage sensitive features for each of the singular value order. Thirdly, estimate modal properties from each of the reproduced AR models respectively relevant to the singular value order. Fourthly, depict the stabilization diagram and find the reasonable model representing actual modal properties of the bridge. Though the fourth step requires an experience in modal identification, this procedure is possibly much concise than the conventional modal identification methods. That is because the proposed feature extraction method automatically provides reasonable choice of a model to describe bridge vibrations observed as reference dataset.

The AR model in Eq. 6.2 is representable as follows according to its definition.

$$\boldsymbol{x}_{k+2} = \boldsymbol{A}'\boldsymbol{x}_{k+1} + \boldsymbol{e}'_k \tag{6.54}$$

$$\boldsymbol{y}_k = [\boldsymbol{I} \quad \boldsymbol{O} \quad \cdots \quad \boldsymbol{O}]\boldsymbol{x}_{k+1} \tag{6.55}$$

where $\boldsymbol{e}'_k \in \mathbb{R}^{mp\times 1}$ and $\boldsymbol{A}' \in \mathbb{R}^{mp\times mp}$ respectively represent following matrices.

$$\boldsymbol{A}' = \begin{bmatrix} \boldsymbol{\alpha}_1 & \boldsymbol{\alpha}_2 & \cdots & \boldsymbol{\alpha}_{p-1} & \boldsymbol{\alpha}_p \\ \boldsymbol{I} & \boldsymbol{O} & \cdots & \boldsymbol{O} & \boldsymbol{O} \\ \boldsymbol{O} & \boldsymbol{I} & \ddots & \vdots & \vdots \\ \vdots & \vdots & \ddots & \vdots & \vdots \\ \boldsymbol{O} & \boldsymbol{O} & \cdots & \boldsymbol{I} & \boldsymbol{O} \end{bmatrix} \tag{6.56}$$

$$\boldsymbol{e}'_k = \begin{bmatrix} \boldsymbol{e}_{k+1} \\ \boldsymbol{0} \\ \vdots \\ \boldsymbol{0} \end{bmatrix}. \tag{6.57}$$

Note that the matrix $\boldsymbol{A}'$ given in Eq. 6.56 has same eigenvalues as the matrix $\acute{\boldsymbol{A}}$ in Eq. 2.86, and thus the eigenvalues are relevant to the modal properties of a structure. The regressive model consisting of the damage sensitive features is derived from the following relationship according to the AR model given in Eq. 6.2.

$$\begin{aligned} y_k^{(j)} &= \textstyle\sum_{i=1}^{p} \boldsymbol{\alpha}_i^{\{j\}} \boldsymbol{y}_{k-i} + e_k^{(j)} = \boldsymbol{w}^T \boldsymbol{x}_k + e_k^{(j)} \\ &= \widetilde{\boldsymbol{w}}_1{}^T \boldsymbol{U}_1^{\mathrm{T}} \boldsymbol{x}_k + \widetilde{\boldsymbol{w}}_2{}^T \boldsymbol{U}_2^{\mathrm{T}} \boldsymbol{x}_k + e_k^{(j)} \end{aligned} \tag{6.58}$$

In the above relationship, the term $\tilde{\boldsymbol{w}}_1{}^T \boldsymbol{U}_1^{\mathrm{T}} \boldsymbol{x}_k$ represents the regression term relevant to the damage sensitive features. Supposing $\boldsymbol{U}_2^{\mathrm{T}} \boldsymbol{x}_k \approx \boldsymbol{0}$ such as the SSI mentioned in Chapter 3, the AR model given in Eqs. 6.54 and 6.55 is approximately simplified to the following relationship.

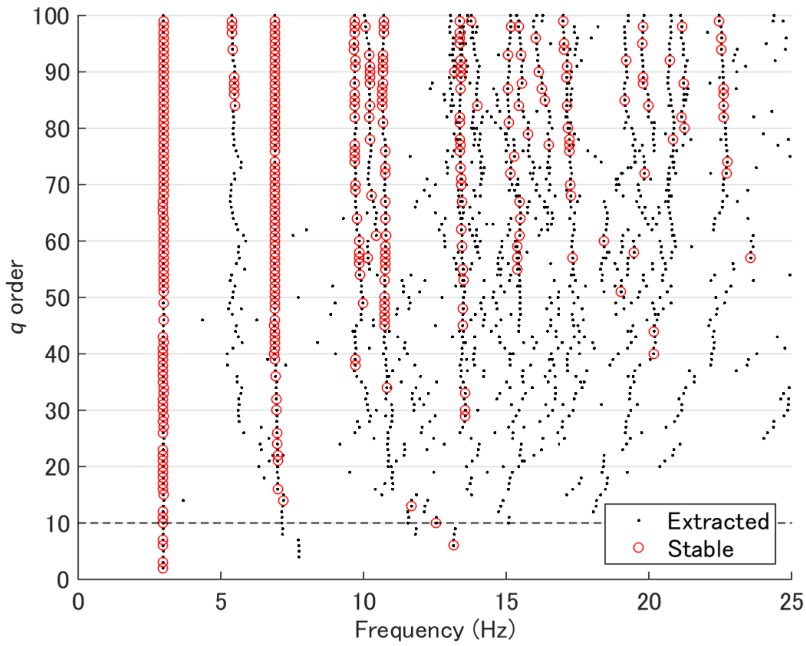

a)

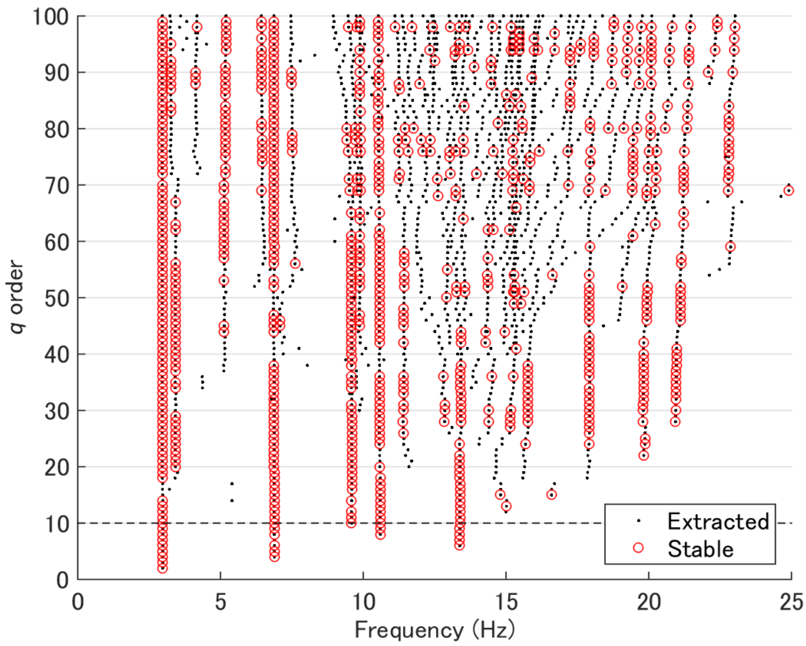

b)

Figure 6.3 Stabilization diagrams with respect to the *q* order:

a) for low order AR model (*p*=20); b) for higher order AR model (*p*=150).

$$\widetilde{\boldsymbol{x}}_{k+1} = \widetilde{\boldsymbol{A}}\widetilde{\boldsymbol{x}}_k + \widetilde{\boldsymbol{e}}_k \quad (6.59)$$

$$\boldsymbol{y}_k = \widetilde{\boldsymbol{C}}\widetilde{\boldsymbol{x}}_k \quad (6.60)$$

where $\widetilde{\boldsymbol{x}}_k = \boldsymbol{U}_1^{\mathrm{T}}\boldsymbol{x}_{k+1}$, $\widetilde{\boldsymbol{A}} = \boldsymbol{U}_1^{\mathrm{T}}\boldsymbol{A}'\boldsymbol{U}_1$, $\widetilde{\boldsymbol{C}} = [\boldsymbol{I} \quad \boldsymbol{O} \quad \cdots \quad \boldsymbol{O}]\boldsymbol{U}_1$, and $\widetilde{\boldsymbol{e}}_k = \boldsymbol{U}_1^{\mathrm{T}}\boldsymbol{e}'_k$. The matrices $\widetilde{\boldsymbol{A}}$ and $\widetilde{\boldsymbol{C}}$ appearing in Eqs. 6.59 and 6.60 provide estimators of modal properties as well as the SSI. The most provable values of the modal properties with respect to the reference dataset are approximately obtained by substituting $\boldsymbol{m}_r$, wich is the most probable values of AR coefficients given in the posterior distribution, to $\boldsymbol{A}'$ in Eq. 6.56.

Figure 6.3 shows the stabilization diagrams derived from the lower and higher AR order models. The vertical axis represents the q order for the proposed feature extraction, and the horizontal axis shows the modal frequencies estimated from each of the AR model reproduced from the features. Aiming at practical use, in this chapter, the stability criteria are simplified as follows instead of Eqs. 3.54−3.56.

$$\mathrm{abs}\left(f_q - f_{q-1}\right) < f_{th} \quad (6.61)$$

$$\mathrm{abs}\left(\xi_q - \xi_{q-1}\right) < \xi_{th} \quad (6.62)$$

$$\mathrm{MAC}\left(\boldsymbol{\phi}_q, \boldsymbol{\phi}_{q-1}\right) > MAC_{th} \quad (6.63)$$

where f_q, ξ_q, and $\boldsymbol{\phi}_q \in \mathbb{R}^{m\times 1}$ respectively represent any of modal frequencies, damping ratio, and modal vectors estimated from the feature extraction with q order. f_{th}, ξ_{th}, and MAC_{th} are predefined thresholds. The stable modes satisfying Eqs. 6.61−6.63 are depicted as red circles in the diagrams. The thresholds f_{th}, ξ_{th}, and MAC_{th} indicates the modal properties that are stably estimated regardless the order q. That is, the red circles standing in lines in the stabilization diagrams shows the physically meaningful modes. Note that the thresholds have to be defined manually in advance. In this study, $f_{th} = 0.005$ Hz, $\xi_{th} = 0.005$, and $MAC_{th} = 0.99$ are respectively adopted. Apparently, Figure 6.3 shows that the proposed feature extraction method succeeds to extract some stable modes from the AR coefficient. Figure 6.3b especially describes stable feature extraction; the five stable modes appearing on q =10 correspond to the physically meaningful modes identified in Chapter 3. This study therefore adopt q =10, which is depicted as dashed horizontal lines in Figure 6.3, in the following discussions. Comparison in Figure 6.3 demonstrates it is beneficial to use higher AR order model for the proposed feature extraction method.

6.4.2 Damage detection

The INT scenario and RCV scenario are regarded as reference scenarios for DMG1 and DMG2 scenarios and DMG3 scenario, respectively. Especially, the RCV scenario is adopted as the reference scenario for DMG3 as the modal characteristics of the bridge might be changed after repairing the damaged member. The vehicle speed can also affects the estimated AR coefficients. Thus, following two cases are considered: For Case 1, INT40 is adopted as a reference scenario for DMG1 and DMG2; and RCV is adopted as a reference scenario for DMG3. For Case 2, INT30, INT40 and INT50 are adopted as a reference dataset for DMG1 and DMG2. Note that RCV scenario was conducted only under speed of 40 km/h, and is not investigated for Case2. Table 6.1 summarizes the conditions mentioned above.

According to the suggestion of Kass and Raftery mentioned in Section 6.2.2, this study adopts $2\ln B$ as a test statistic, and a pre-defined threshold for the hypothesis testing is fixed to $2\ln B = 0$, where the model evidences for the null and the alternative hypotheses are equivalent. From now on, let the threshold $2\ln B = 0$ be referred as 'critical value' for the hypothesis testing. Leave-one-out cross validation (CV) technique is applied to assess the validity of the Bayes factors. For example, letting a set containing l samples of time series of target variables $\{\boldsymbol{t}_1, \boldsymbol{t}_2, \dots, \boldsymbol{t}_l\}$ are obtained from a bridge without damage, take one of the time series (e.g., $\boldsymbol{t}_1$) out from this set as a test data, and then refer the set excluded the test sample $\{\boldsymbol{t}_2, \dots, \boldsymbol{t}_l\}$ as the reference dataset. The l Bayes factors are thus calculable only from the l samples of time series. From now on, the Bayes factors calculated by CV technique are referred as CV samples of the Bayes factors. The validity of the Bayes factors is confirmed by checking whether the CV samples support null or alternative hypothesis.

To begin with, the global Bayes facotrs for BF ver.1 provide general view to grasp feasibility of the proposed method. Figure 6.4 shows the global Bayes factors respectively for Case 1 and Case 2. Each of

Table 6.1 Cases considered for the damage detection.

	Reference Scenarios	Damage Scenarios
Case1	INT40	DMG1 and DMG2
	RCV	DMG3
Case2	INT30, INT40 and INT50	DMG1 and DMG2

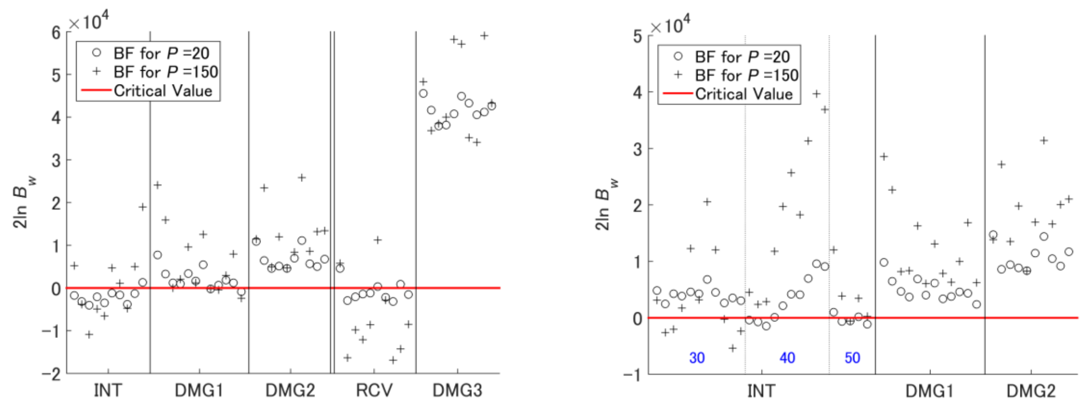

a) b)

Figure 6.4 Global Bayes factors for BF ver.1:

a) for Case1; b) for Case 2 (30, 40 and 50 denote vehicle speed in km/h).

the depicted plots are relevant to each of the samples of vehicle loading tests. Both of the results calculated from the lower AR order (p=20) and the higher AR order (p=150) models are provided on the diagrams. Figure 6.4 shows that BF ver.1 appears to detect anomalies on the AR model since most of the Bayes factors exceed the critical values for damage scenarios (i.e., DMG1, DMG2 and DMG3). The figures also suggest that the Bayes factors indicate severity of the damage since the Bayes factors given under the full-cut scenario (DMG2 and DMG3) are tend to provide higher values than under the half-cut scenario (DMG1). Most of the Bayes factors even exceed $2\ln B = 10$ for damage scenarios, which represents 'very strong' evidence against the null hypothesis according to the interpretation of Kass and Raftery.

However, especially for Case 2, the Bayes factors tend to exceed the critical value even for INT scenario, and thus they are not reliable as a damage indicator. That is possibly because the vehicle speed affects the AR coefficients. As mentioned in Section 6.2.2, some of the AR coefficients are composed of parameters irrelevant to modal properties of the bridges, the anomalies appearing in Case 2 are possibly caused by those spurious coefficients. This observation suggests that BF ver.1 is likely to lead a false alert in practice such that the speed of passing vehicle is not constant. For Case 1, the Bayes factors are tend to be lower than the critical values, and thus BF ver.1 is still useful when the vehicle speed is constant. Comparing the lower and higher AR order model, the numerical results from the lower order model seems to be more stable. For instance in Figure 6.4a, variances appearing in the reference scenarios (INT and RCV) are smaller for the lower order model. Thus, for BF ver.1, the lower order model provides more practical to damage detection since its stable numerical result is expected to enable trustworthy interpretation of the condition of the bridge. This observation is also due to the spurious parameters contained in the higher order model because the higher order AR coefficients tend to be contaminated by unexpected noise.

Similarly, the global Bayes factors for BF ver.2 are given as Figure 6.5. Figure 6.5a shows each of the Bayes factors are more stable compared to BF ver.1. Those results show that BF ver.2 also indicates

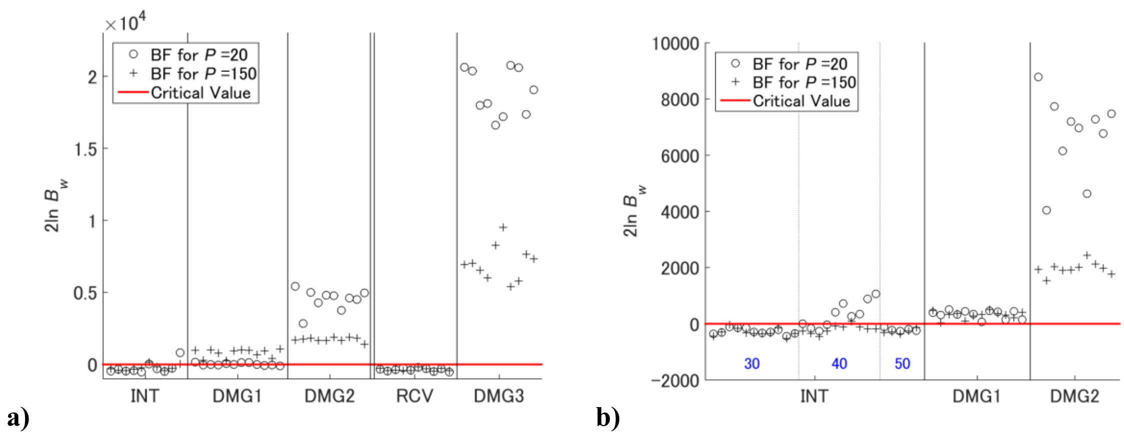

Figure 6.5 Global Bayes factors for BF ver.2:

a) for Case1; b) for Case 2 (30, 40 and 50 denote vehicle speed in km/h).

damage severity for the damage scenarios. It is noteworthy that damage detection for scenario DMG1 is more effective for the higher order model than the lower order model. That is possibly because the higher order model reproduced by the proposed feature extraction method describes more reasonable model of the vibrating bridge. According to Figure 6.3, the reproduced higher order model enables to identify not only the dominant modes but also the higher order modes. Thus, the improvement appeared in Figure 6.5a for DMG1 is possibly contribution of the higher order modes described in the reproduced higher AR order model. Generally, it is more difficult to identify the higher order modes than the dominant ones. The proposed feature extraction method therefore expected to be one of effective ways to identify modal properties. Figure 6.5b shows the stability of the Bayes factors resulting from INT scenario is considerably improved, comparing to Figure 6.4b. It is also noteworthy that the higher order model gives more stable results than the lower order model. That is possibly because the proposed feature extraction method reduces unexpected effect caused by the vehicle speed and reproduces the AR models to reasonable models purely describing the vibrating bridge. The above observation shows the higher AR model is more practical for BF ver.2.

Table 6.2 summarizes the percentages of the correct answers with respect to the global Bayes factors mentioned above, namely, Bayes factors satisfying $2\ln B_w < 0$ are regarded as correct answers for the reference scenarios; Bayes factors satisfying $2\ln B_w > 0$ are regarded as correct answers for the damage scenarios. The greyed out cells in Table 6.2 represents the scenarios whose ratios of correct answers are less than 50 %, and thus the grey area briefly shows unreliable Bayes factors with respect to each of the scenarios. As mentioned above paragraphs, BF ver.1 with lower AR model and BF ver.2 with higher AR model are respectively reasonable for Case1. For Case2 where the vehicle speed is altered, BF ver.1 provides unstable results on INT scenario, whereas BF ver.2 provides stable results. Aiming at practical use, since traffic load is not induced by vehicles passing at a constant speed, BF ver.2 can gives a more reliable way for damage detection if a reasonable q order is given according to stabilization diagrams as Figure 6.3b. Note that the reasonable choice of the q order however requires interpretation owing to experienced engineers. From now on, the discussions are given only for BF ver.1 with the lower order AR model and for BF ver.2 with the higher order AR model, which are respectively noted in boldfaced type

Table 6.2 The ratios of correct answers for the global Bayes factors (%).

	AR order	Case 1					Case 2		
		INT	DMG1	DMG2	RCV	DMG3	INT	DMG1	DMG2
BF ver.1	***p* =20**	**90**	**83**	**100**	**70**	**100**	**23**	**100**	**100**
	p =150	50	67	100	80	100	23	100	100
BF ver.2	*p* =20	80	42	100	100	100	73	100	100
	***p* =150**	**80**	**100**	**100**	**100**	**100**	**96**	**100**	**100**

in Table 6.2.

Figure 6.6 gives the local Bayes factors for BF ver1, and similarly, Figure 6.7 gives the local Bayes factors for BF ver2. The points depicted in the figures relevant to the measurement points appearing in Figure 1.3c. Each of those figures shows that the local Bayes factors have significance values that are considerably higher than the Bayes factors of the other measurement points for DMG2 and DMG3. For DMG2, the significance values appear at the measurement point A3 in every cases. For DMG3, on the

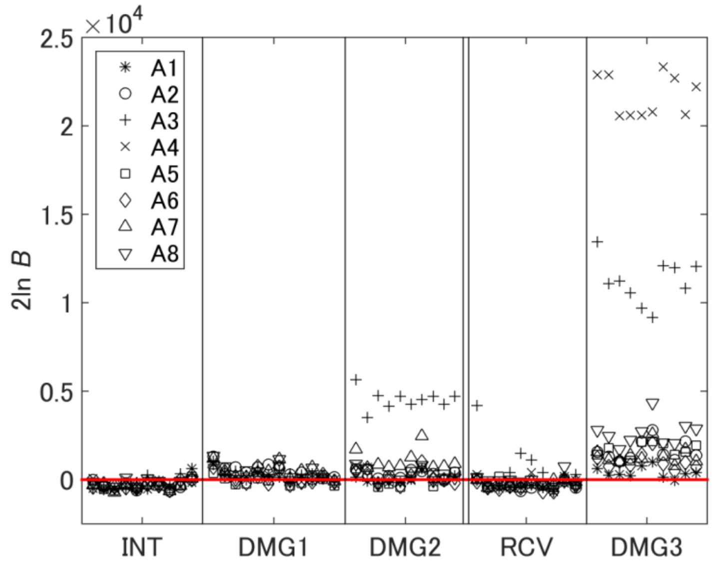

a)

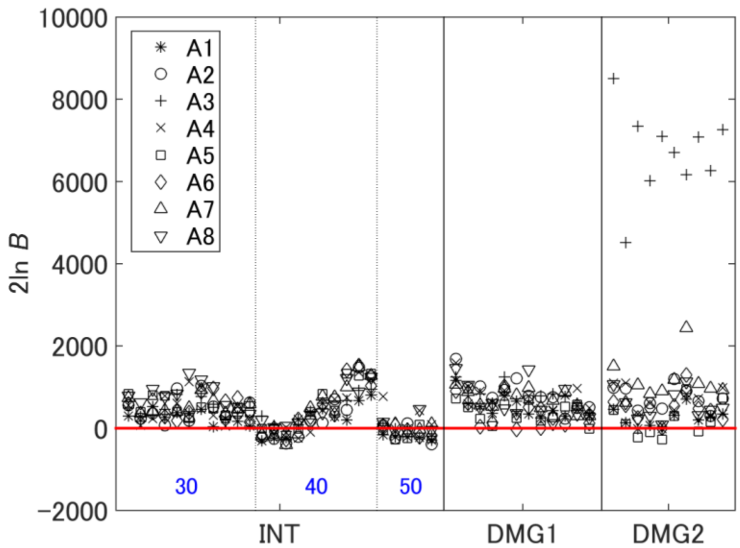

b)

Figure 6.6 Local Bayes factors for BF ver.1 (P=20):

a) for Case1; b) for Case 2 (30, 40 and 50 denote vehicle speed in km/h).

other hand, the significance values appear at A4. The A3 and A4 are the closest measurement points to the damaged member respectively for scenarios DMG2 and DMG3. For the half-cut scenario, significant values do not appear. Those observations suggest that the local Bayes factors indicates the severity of damage at each of the measurement points if the damage is considerably serious such that one of the members thoroughly ruptures. Therefore, the proposed local Bayes factors can be one of feasible indicators to localize damage for severe damage.

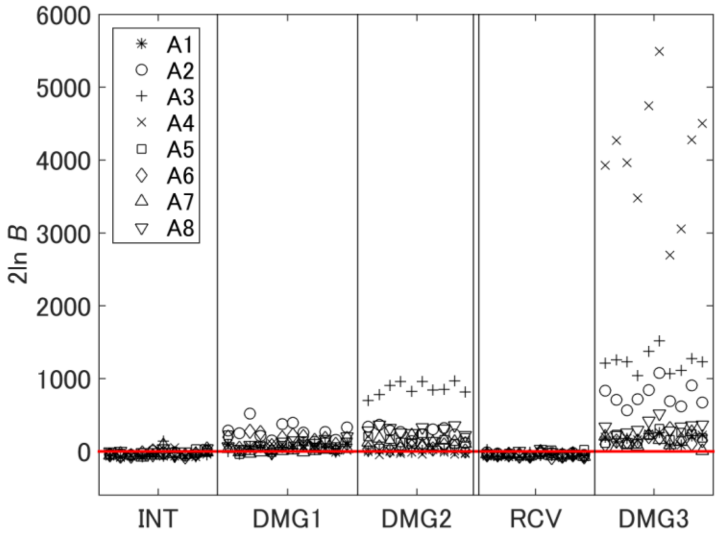

a)

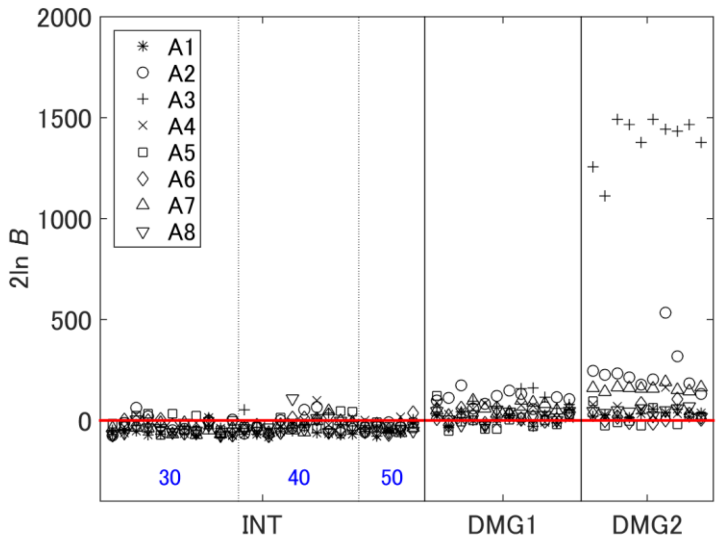

b)

Figure 6.7 Local Bayes factors for BF ver.2 (P=150):

a) for Case1; b) for Case 2 (30, 40 and 50 denote vehicle speed in km/h).

6.4.3 Comparison to the previous damage indicator

This section provide comparison of this study to the damage indicator (DI) investigated in Chapter 5. In the hypothesis testing, the null and alternative hypothesis respectively represent healthy and damaged bridge as well as the proposed method in this chapter. The hypothesis testing accordingly provides damage detection method based on Mahalanobis distance, which evaluates a stochastic distance among damage sensitive features extracted from estimated AR model coefficients. Here, the damage detection performance of the DIs considerably affected by the AR coefficients contaminated by unexpected noise, and thus the AR order should be carefully predefined. In fact, the previous study showed p=8 is suitable AR order for the hypothesis testing as mentioned in Section 5.3.1. That AR order is less sufficient to describe the vibrating bridge.

Figure 6.8 shows the results of the previous method, where the order of the principal subspace is fixed to 2 and the significance value for the hypothesis testing is fixed to 5%. The red horizontal line represents the critical value of the hypothesis testing. The sample means are depicted as the black dashed horizontal lines. The sample means and the critical values are also evaluated for the CV samples derived from the reference scenario (INT and RCV). Figure 6.8a shows that the previous method succeeds to detect damage for Case1, though each of the DI is not so stable comparing to the results appearing in Figure 6.4a and Figure 6.5a for the full-cut scenarios. However, Figure 6.8b shows the previous method is not helpful for Case2. That observation suggests it is difficult to avoid uncertainty resulting from unexpected noise affecting on the estimated AR coefficients by means of the previous feature extraction method. It is noteworthy that the feature extraction method provided in this study enabled to avoid the unexpected noise. That is presumably because the singular values decomposition, which is relevant to the principal component analysis for the vectors $\boldsymbol{x}$, results in more reliable feature extraction than the principal component analysis onto the evaluated coefficients.

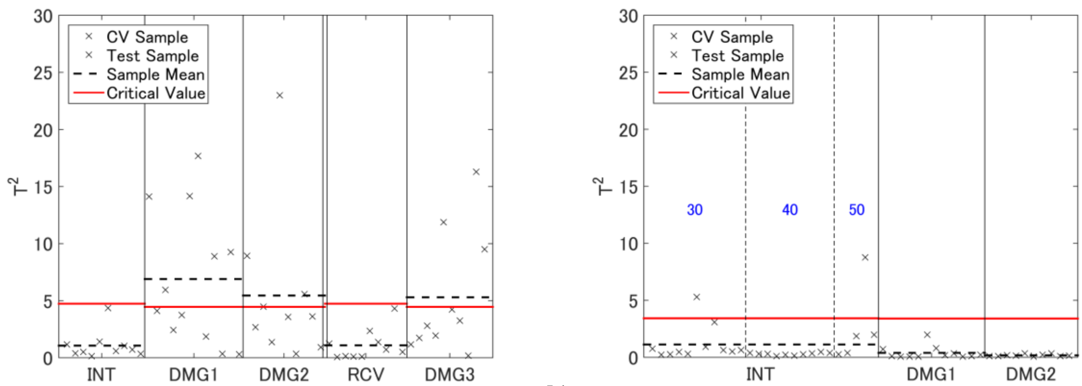

a) b)

Figure 6.8 Previously investigated damage indicators:

a) for Case1; b) for Case2 (30, 40 and 50 denote vehicle speed in km/h).

Therefore, the proposed methods provide following three advantages comparing to the previous method:

- The AR order can be easily determined with the Schwarz criterion. That is, the degree of freedom of the parametric model can be determined based on the quantified information.
- Using the proposed feature extraction method, the unexpected noise affecting the AR coefficient can be reduced. The reproduced AR model enables reasonable choice of damage sensitive features by means of the stabilization diagram.
- It is expectable that the Bayes factors demonstrate severity of damage. The local Bayes factors even enable to localize damage for serious damage such as ruptures on a member.

6.5 Summary

This study investigates damage detection method for bridges based on traffic-induced vibration to cope with difficulties in decision-making for bridge maintenance. The Bayesian hypothesis testing is adopted to detect subtle changes in modal properties caused by damage.

A time series of actually observed accelerations of a bridge provides a likelihood function of a multivariate autoregressive (AR) model. The likelihood function and the non-informative prior computationally produce the posterior distribution of the regressive parameters composing the AR model. Using accelerations measured from a bridge under healthy condition, the posterior distribution provides a stochastic reference model representing healthy bridge vibrations. Based on the posterior distribution, the Bayes factor is formulated for anomaly detection. This study proposes two types of Bayes factors: one evaluates anomaly appearing on the AR model, and the other evaluates anomaly on damage sensitive feature extracted by means of the singular value decomposition onto one of the hyperparameters composing the posterior distribution. The extracted features reproduce the AR model to a relevant state space model in which unexpected noise derived from environmental effects is eliminated. Bayesian hypothesis test for damage detection is conducted utilizing the Bayes factors.

To investigate feasibility of the proposed approach for damage detection, this study examined experimental data on an actual steel truss bridge whose truss members were artificially severed. The efficacy of the model selection and feature extraction mentioned in Chapter 3 are experimentally investigated. The AR order is statistically determined referring the Schwarz criterion, which is relevant to the Bayesian information criterion. The feature extraction enables model reduction as well as the stochastic subspace identification. A stabilization diagram composed from the AR models reproduced by the extracted features helps reasonable choice of the features.

The two types of the proposed Bayes factors detected three different damage levels successfully when the given reference data is derived from vehicles passing by a constant speed. Although the Bayes factor without feature extraction provides unstable results if the vehicles are passing by various speed, the Bayes factor with feature extraction succeeds to reduce the effect from unexpected noise caused by the vehicle speed and to provide stable results for the hypothesis testing. Both of the proposed Bayes factors appear to evaluate severity of the damage. For serious damage scenarios, where the truss members were thoroughly ruptured, the Bayes factors showed significant values at the measurement points that are closest to the damaged members. This result suggests possibility of damage localization for severely damaged members.

Compared to the damage detection method investigated in Chapter 5, the newly proposed methods show advantages in practical use. Especially, the proposed feature extraction method enables to reduce the unexpected noise effect, whereas it is not possible in the previously proposed feature extraction method. It is therefore expectable that the proposed method provides effective strategy enabling reliable health monitoring for bridges.

Chapter 7

Application to a Steel Plate Girder Bridge

7.1 Introduction

The above discussions enable to detect change in modal properties directly from the monitored acceleration. Especially, the Bayes factor with feature extraction possibly gives reliable damage indicator to make decision for bridge maintenance if the modal properties of bridges are not altered in their healthy condition. However, the modal properties of bridges in field are actually changed by the seasonal temperature fluctuation. In fact, how to handle the temperature fluctuation is one of the challenging tasks on which many existing studies have tackled (e.g., see [30], [52], [91]). The proposed method in this thesis does not completely solve those problems at this moment since the regressive model presented in Chapter 6 does not consider the temperature fluctuation. For further studies, it is desired to establish a regressive model describing the seasonal fluctuation in the modal properties to realize a more practical damage indicator. Although this ideal regressive model requires further investigations on much more monitoring data from actual bridges through years, it is worth to describe the present stage of the study to lay the foundation for the further practical studies. Especially, experimental studies investigating how to process the monitored data are expected for practical applications.

This chapter therefore presents a case study utilizing one-year monitoring data on a plate girder bridge. Accelerations and strains on the bridge girders are monitored. In addition to the dynamic response of the bridge, static changes in its boundary condition are also monitored to investigate influences of the seasonal fluctuation to the modal properties. Finite element (FE) model of the target bridge is established through an experimental model update to investigate its modal properties. One-year monitoring data is investigated utilizing a damage indicator developed in Chapter 6. The seasonal fluctuation of the boundary condition is also discussed. Additionally, the feasibility of the damage detection method is examined through artificial damages after the one-year monitoring. The artificial damage imitate a fatigue clack propagating on one of the main girder. Changes in the natural frequencies due to damage is also examined through stochastic subspace identification (SSI) and eigenvalue analysis of utilizing the updated FE model.

7.2 Target Bridge and Finite Element Model

7.2.1 Target bridge

The field experiment was conducted on a single span steel plate girder bridge shown in Figure 7.1. The span length is around 40m. Figure 7.2 shows the photographs of the supports. The plate shoes fixed onto

a)

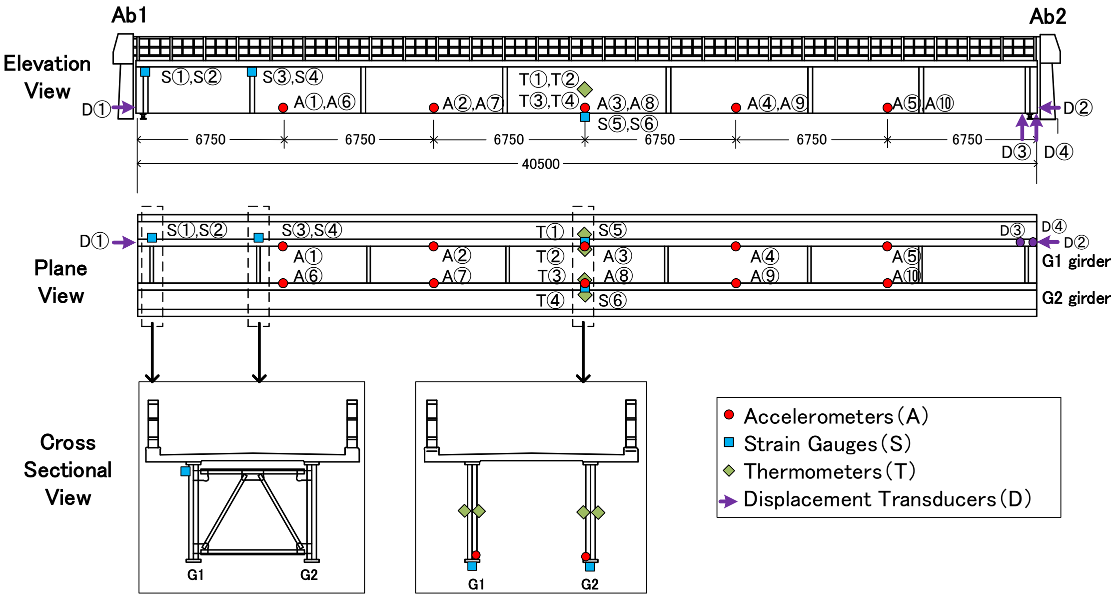

b)

Figure 7.1 The target bridge: a) photograph; b) sensor deployment.

a)

b)

Figure 7.2 Photographs of the supports: a) on Ab1 abutment; b) on Ab2 abutment.

the Ab1 abutment shown in Figure 7.2a. On the other hand, the Ab2 abutment has cantilever-like supports as shown in Figure 7.2b. This member allows longitudinal deformation of the bridge caused by thermal expansion as will be discussed later.

On the bridge, 10 accelerometers, 6 strain gauges, 4 thermometers and 4 displacement transducers were installed as shown in Figure 7.1b. Each of the accelerometers and strain gauges monitors dynamic response of the bridge at sampling rate 200 Hz. The thermometers and the displacement transducers record the static changes every 30 minutes. Each of the accelerometers measures vertical acceleration. The strain gauges settled on the middle of the span, namely S5 and S6 measure longitudinal strain on the bottom of the lower flange. The arrows in Figure 7.1b demonstrate the directions of measuring displacement. The monitoring is operated from September 2016 to August 2017. The ordinary traffic was blocked at 28th March 2017 as new bridge was opened. After the stoppage of traffic, only vehicles for a tunnel construction were permitted on the bridge. The acquired time series are stocked into data loggers equipped nearby the bridge. The dynamic data for the measured acceleration and strains were collected from the data loggers around every two weeks because of the limitation of the data storage.

After the one-year monitoring, artificial fatigue cracks (hereafter called artificial damage) at the girder end near the base plate of supports on the Ab1 abutment are considered in the experiment by severing the lower flange and the web plate by an Oxyacetylene cutting torch. The location of the artificial damage is at the lower flange and the web plate of the east main girder (the G1 girder) on the Ab1 abutment as shown in Figure 7.3. The artificial damage comprises two damage levels. One is the lower flange cut (hereafter called DMG1) and another one is the web plate cut (hereafter called DMG2) as shown in Figure 7.3. To prevent any possible bridge collapse due to the artificial damage on the girder, a protection device was installed near the damage location before introducing the artificial damage. In addition, a stop hole was drilled to prevent the crack propagation. The bridge condition before introducing the artificial damage is

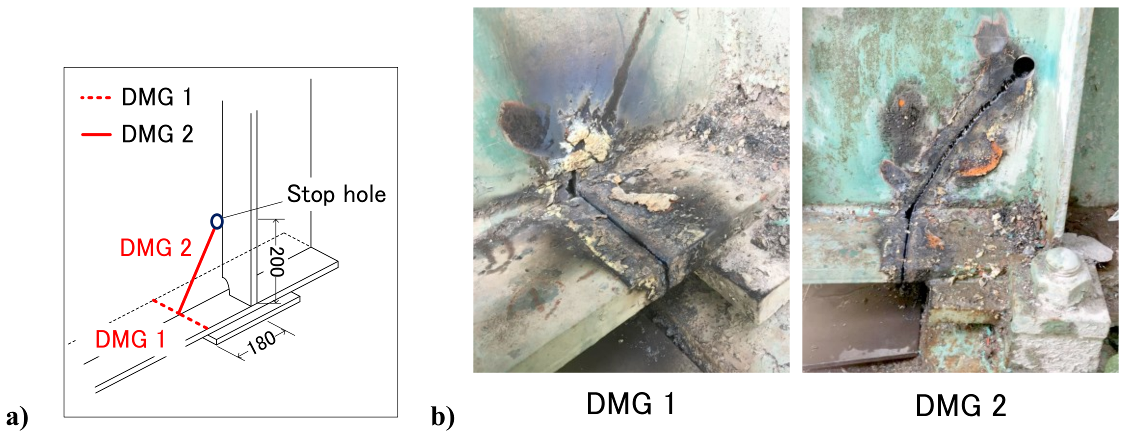

Figure 7.3 Artificial damages on the G1 girder near the base plate of Ab1: a) Schematic diagram; b) photographs.

assumed as the intact condition (hereafter called INT).

The vehicle used for the moving vehicle test was a passenger car and the speed of car is about 20km/h. Higher speeds were not considered since the accelerating and decelerating distances were too short to increase the vehicle speed. The vibration test is conducted 60 times (30 round trips) for the intact condition, and 30 times (15 round trips) for each of the damage conditions. Sampling rate and length of the vibration data set were 200Hz and 15s, respectively.

7.2.2 Finite element model

To investigate the structural characteristics of the bridge, the eigenvalue analysis using the FE model of the bridge was conducted by utilizing ABAQUS 6.14. The bridge model, shown in Figure 7.4, was built based on the documents of periodic inspection and information obtained from the field experiment as the design documents of this bridge were not available. The bridge consists of concrete deck, main girders, vertical stiffeners, cross frames and lateral bracings. The concrete deck, main girder and vertical stiffener were modeled with shell element, and cross frame and lateral bracing were modeled with beam element. For the boundary condition, fixed support was assumed for the support at the Ab1 abutment and roller support was assumed for the support at the Ab2 abutment. Specific gravity of steel and concrete are 7.85 and 2.40, respectively. Young's modulus of steel was assumed as 210 GPa. The Young's modulus of concrete was assumed as 22.02 GPa that was obtained from compression test of the concrete core.

Since the bridge model has some differences from the actual bridge due to deterioration, lack of design documents and so on, the bridge model needs model updating for calibrating parameters of the bridge model. The cross entropy (CE) method was applied to update the bridge model so that the natural frequencies of the bridge model become comparable to those of the actual bridge. The CE method involves an iterative procedure where each iteration is divided into two steps [92]. First step is to generate a random

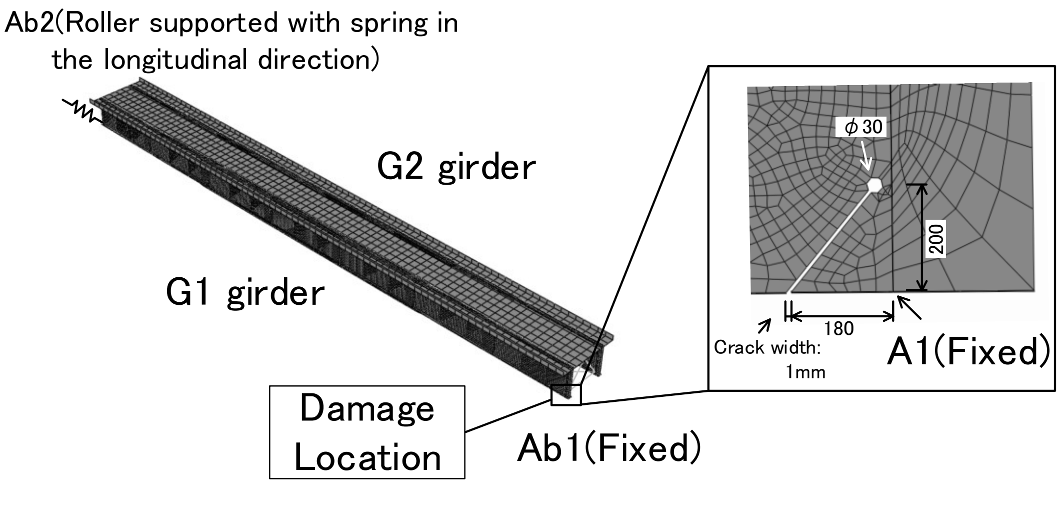

Figure 7.4 FE model of the bridge and pseudo cracks on plate girder.

data sample according to a certain probability distribution. Second step is to update the parameters of the probability distribution based on the data generated in the first step in order to produce better samples in the next iteration.

The structural characteristics of the bridge was slightly different from those before the damage experiment because of the protection device installed on the bridge for the damage experiment as previously stated. However, any possible influence caused by the protection devices was not considered in the model. To update the bridge model, an elastic spring in the longitudinal direction was introduced into the roller support, and the spring stiffness was calibrated by the model update. In addition, to investigate the change in structural characteristics, the artificial damage was modeled as pseudo cracks in

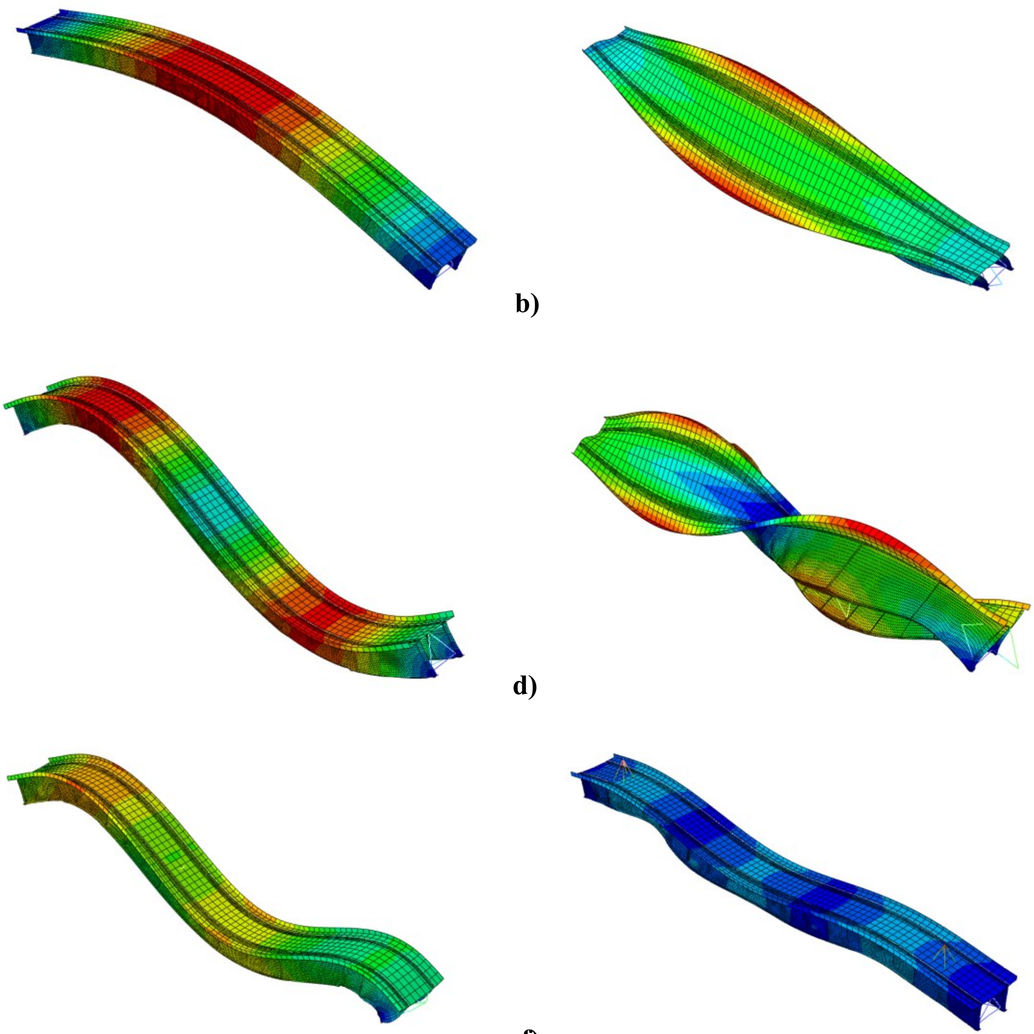

a) b) c) d) e) f)

Figure 7.5 Modal deformations identified in FE model for the INT scenario:

a) 1st bending (3.08 Hz); b) 1st torsional (5.08 Hz); c) 2nd bending (9.36 Hz);

d) 2nd torsional (10.84 Hz); e) Asymmetric bending (15.49 Hz); f) 3rd bending (21.57 Hz).

Table 7.1 Natural frequencies identified in the FE model (Hz).

Mode	INT	DMG1	DMG2
1st bending mode	3.08	3.08	3.07
1st torsional mode	5.08	5.02	4.69
2nd bending mode	9.36	9.33	9.27
2nd torsional mode	10.84	10.82	10.60
Asymmetric bending mode	15.49	15.02	13.47
3rd bending mode	21.57	21.37	20.63

the FE model. The crack was created by removing the connection of elements in the FE model (see Figure 7.4).

The eigenvalue analysis was conducted for each of the damage scenarios on the updated FE models. Observation from the identified mode shapes showed that the 1st, 2nd and 3rd modes were related to the bending and torsional modes respectively. Additionally, an asymmetry bending mode shape which is similar to the 2nd bending mode was also observed. That is possibly because the boundary condition in the FE model is not symmetric. Note that the boundary condition is modeled considering the asymmetric supports as shown in Figure 7.2. Figure 7.5 shows the modal deformations identified from eigenvalue analysis in the FE model for the INT scenario for instance. Table 7.1 summarizes the identified natural frequencies. These results show that the natural frequencies decrease as the fatigue crack propagates. This observation is reasonable since the global bending stiffness of the bridge girder will decrease as the moment of inertia decreases at the damaged location. For the 1st bending mode, the change in the natural frequency is smaller than the other modes. That is possibly because the modal deformation of the 1st bending mode cause less stress on the damaged part of the girder.

7.3 One Year Monitoring

7.3.1 Vibration monitoring

As mentioned in Section 7.2.1, the monitoring data are collected from the data loggers equipped nearby the bridge around every two weeks because of the limitation of the data storage of the loggers. Aiming at practical bridge management, remote monitoring is desired to realize continuous long-term health monitoring. However, in reality, it is almost impossible or not practical transmit the entire huge amount of the acquired time series of the monitored acceleration. On-site data processing such as data compression and transition is therefore impotent. That is, the signal processing to reduce the amount of data is to be operated in the field at first. This study aims to design an on-site data processing procedure. Since the proposed Bayes factor enables direct transformation from time series to the damage indicator, the main target of the on-site data processing is how to pre-process the acquired time series for damage detection. Aiming at general use for a plate girder bridge, this study merely utilizes strain gauges equipped on the lower flange at the middle of the span for detecting vehicle loading promptly. In the monitoring, the strain gauges installed at S5 and S6 in Figure 7.1b detect the vehicle loading.

For instance, Figure 7.6 shows 5 minutes time series measured by the strain gauges and the accelerometer. Therein, the time series of the strain are smoothed with low-pass filter of 1 Hz and averaged together for clarity. The peaks appear in the time series of the strain, which is marked as circles in Figure 7.6a as the vehicles pass on the bridge. Those peaks and their widths are easily detected by means of peak

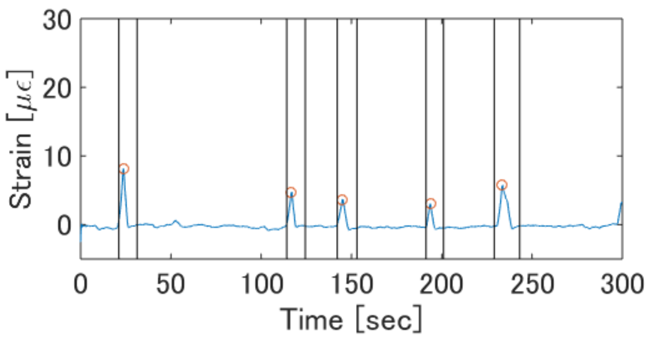

a)

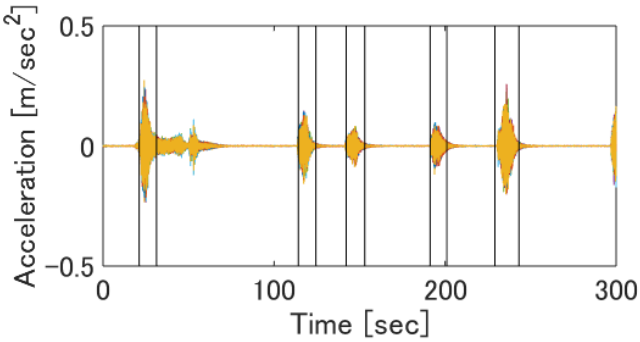

b)

Figure 7.6 Time series before pre-processing: a) Averaged strain; b) Acceleration.

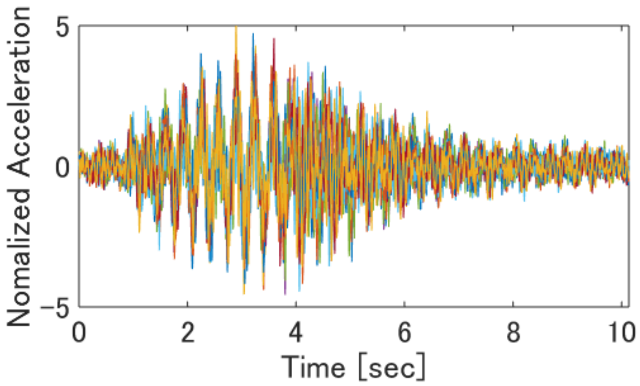

Figure 7.7 Example of time series of acceleration extracted from long-term monitoring data.

picking analysis. Accordingly, the moment at the entrance and exit of the vehicle can be roughly estimated from the peak width. This study experimentally obtains time series data for damage detection by following rules:

- The vehicle-induced vibrations between vehicle entrance and 5 seconds after vehicle exit are extracted from long term monitoring data.
- If the extracted areas coincide with each other, those time series are discarded.
- The extracted time series are normalized by dividing root mean square of the all acceleration data points contained in the time series.

The first rule roughly enables to choose vehicle-induced vibration. The second rule is experimentally adopted to extract vibration induced by a single vehicle. The third rule is adopted to realize white noise assumption approximately, i.e., the loading forces are roughly regarded to be steady. The vertical lines depicted in Figure 7.6 represent truncation window in the time series for instance. Figure 7.6b describes that the vehicle-induced vibrations are correctively identified from the raw time series data. Although the pre-processing sometimes fails to extract vehicle induced vibration data correctively, this study utilizes all of the extracted data aiming at an automatic on-site signal processing. Figure 7.7 shows the first time series of acceleration extracted from the acceleration time history shown in Figure 7.6b for instance. The extracted time series data are utilized for the Bayesian inference and damage detection proposed in Chapter 6.

Following discussions adopt time series obtained from September 1st to 3rd as a reference dataset for damage detection. The latter time series after September 3rd are regarded as a test data set. The model

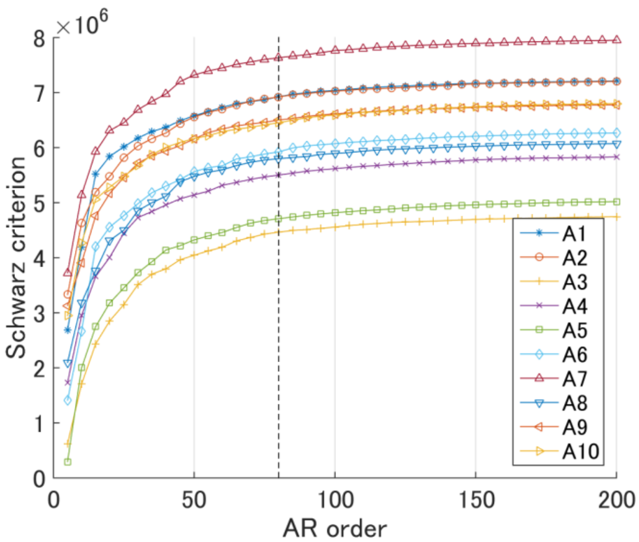

Figure 7.8 The Schwarz criteria with respect to the AR orders.

choice process and feature extraction process are operated following methodologies in Chapter 6. The procedures are summarized as follows: Firstly, sufficiently large AR order is adopted to the Bayesian inference. Secondly, Schwarz criterion, which is relevant to Bayesian information criterion, is examined to find a proper AR order. Thirdly, the hyperparameters of the posterior distribution are reproduced for the proper AR order. Fourthly, the damage sensitive feature is extracted by the singular value decomposition. The degree of the freedom of the damage sensitive feature is determined by examining a

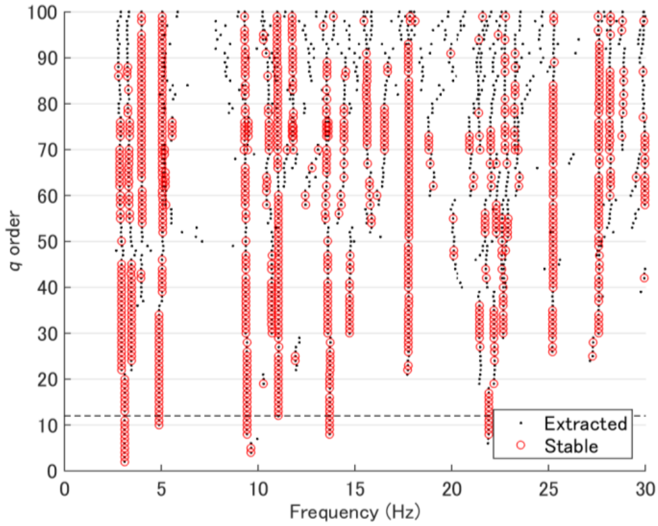

Figure 7.9 Stabilization diagram for the feature extraction process.

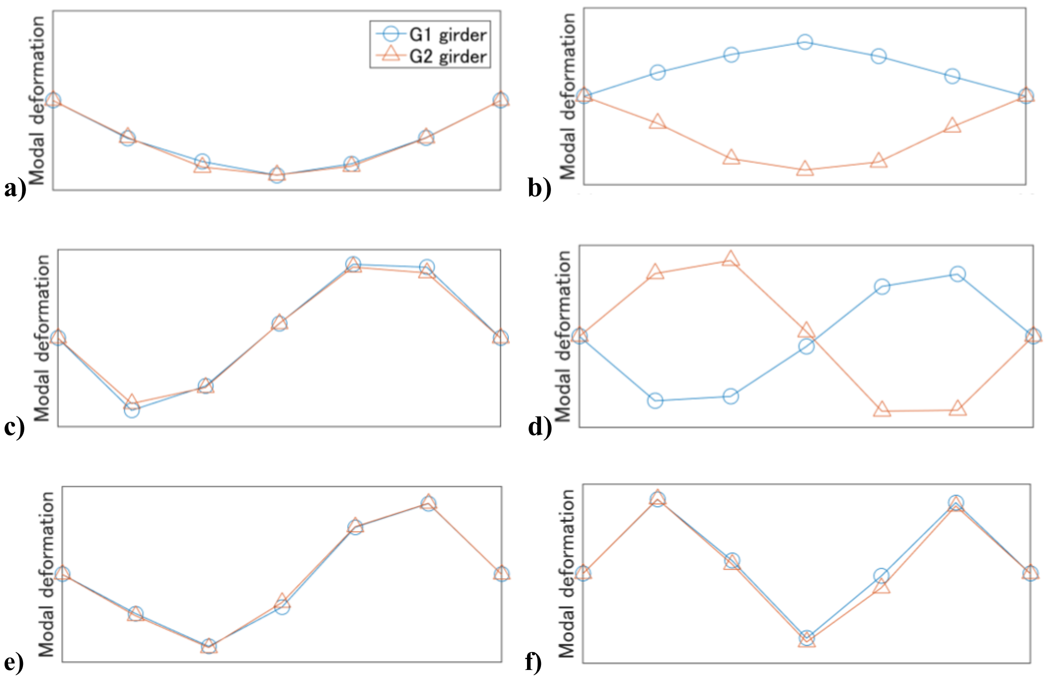

Figure 7.10 Mode shapes relevant to the damage sensitive feature:

a) 1st bending; b) 1st torsional; c) 2nd bending; d) 2nd torsional; e) Asymmetric bending; f) 3rd bending

stabilization diagram.

Figure 7.8 shows the Schwarz criteria with respect to the AR order. This study adopt the 80 order AR model as the dashed vertical line depicted in Figure 7.8. Figure 7.9 shows the stabilization diagram for the feature extraction process. The threshold to extract stabilized poles are same as the case study in Chapter 6, namely, $f_{th} = 0.005$ Hz, $\zeta_{th} = 0.005$, and $MAC_{th} = 0.99$ for Eqs. 6.61−6.63. This study adopts q=12, which is depicted as the horizontal dashed line in Figure 7.9, for the damage sensitive feature. The natural frequencies identified in Figure 7.9 is relevant to the frequencies appeared in the eigenvalue analysis as listed in Table 7.1. Figure 7.10 shows the six mode shapes identified from the state space model of 12 degree of freedom, which is relevant to the damage sensitive features. Apparently, those mode shapes are also comparable to the modal deformation obtained in the eigenvalue analysis produced in Figure 7.5. That is, the extracted damage sensitive features are relevant to the modal properties of the six modes listed in Figure 7.5 and Table 7.1. It is noteworthy that the asymmetry second mode is also identified in the field experiment. Thus, the Bayes factor discussed hereafter evaluates changes in modal properties of those six modes.

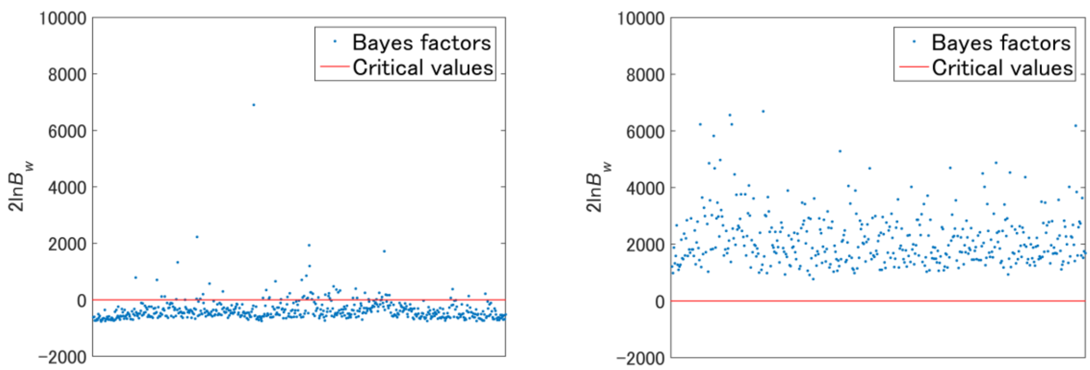

a) b)

Figure 7.11 Observed global Bayes factors measured in one day: a) On September; b) On January.

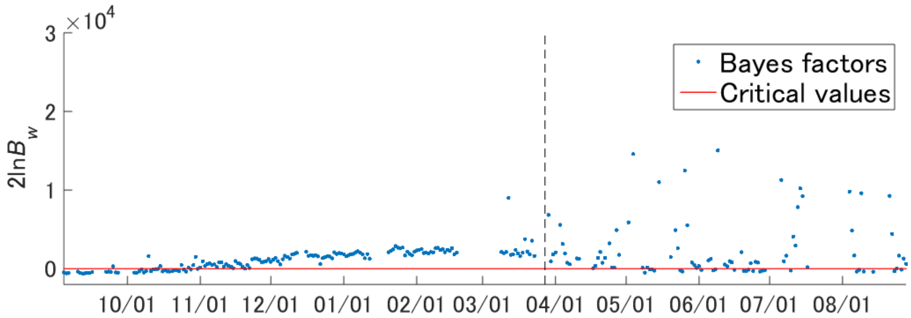

Figure 7.12 Global Bayes factors monitored through a year (Sep 2016- Aug 2017).

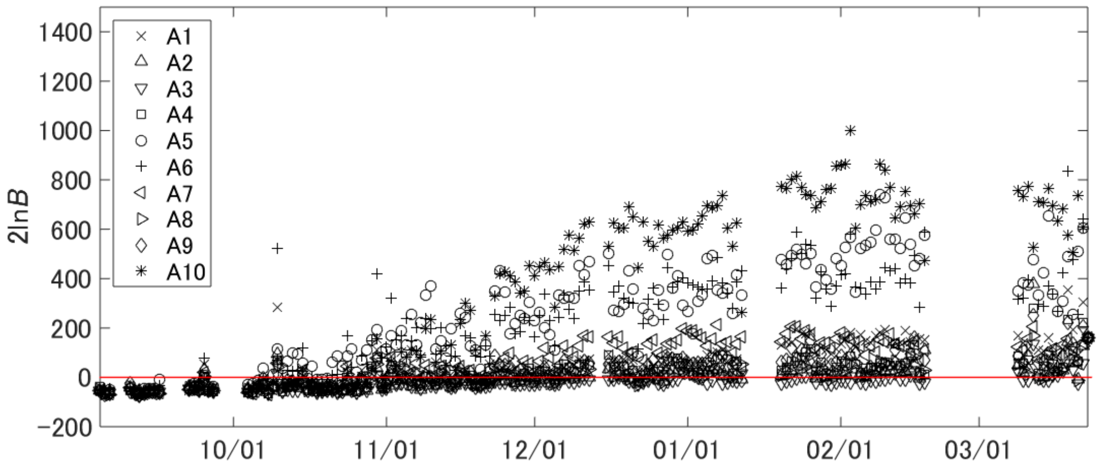

Figure 7.13 Local Bayes factors monitored before the traffic limitation (Sep 2016-Mar 2017).

Figure 7.11 shows the observed global Bayes factors respectively on September 4th and January 5th for instance. Each of the dots in the diagrams represents the Bayes factor calculated from each of the extracted time series as shown in Figure 7.7. The red horizontal lines are the critical values, i.e., $2\ln B_w = 0$. On September, most of the Bayes factor below the critical value except several outliers. This result shows that the modal properties are not altered just after starting monitoring. On the other hand, the Bayes factors on January are positively exceed the critical value even though no source of drastic change in structural integrity has been reported. That is, the modal properties are altered from the reference dataset. Note that the reference dataset is time series obtained from September 1st to 3rd. Those observations demonstrate that seasonal fluctuation of the modal properties are detected by the Bayes factors.

Figure 7.12 shows the global Bayes factors monitored through a year, where each of the dots depicted in the diagram is median of the Bayes factors monitored on each day. The vertical dashed line represents the date when the ordinary traffic was blocked. Note that after the traffic control, only the vehicles for the tunnel construction is permitted. Thus, the number of samples of time series is strictly limited and the traffic condition is quite different. The Bayes factors appearing in Figure 7.12 are therefore not reliable after the traffic control. The Bayes factors monitored before the traffic limitation gradually increase possibly because of the seasonal temperature change. For further investigations, the local Bayes factors observed before the traffic limitation are shown in Figure 7.13, which shows the local Bayes factors at A10 are mostly affected by the seasonal fluctuation. The ones at A5 and A6 are secondly affected. Details about these observations are discussed later.

7.3.2 Seasonal fluctuation of boundary condition

Figure 7.14 shows longitudinal displacements measured on both side of the bridge, namely, the records of the D1 and D2 transducers in Figure 7.1b. The horizontal axis in Figure 7.14b adopts the max value of the temperature measured at the four thermometers to avoid outliers. Note that displacement over 9 mm is truncated for D2 because of the capacity limitation of the transducer. Those results show that the cantilever-like supporting members on the Ab2 abutment allows the longitudinal deformation caused by thermal expansion. Note that the displacements are monitored in compression direction, and thus the positive deformation is relevant to the shrinkage of the bridge girder. Thus, it is reasonable that the displacement measured by D2 transducer has negative correlation with the temperature. This seasonal fluctuation appeared in displacement of the supports on the Ab2 abutment possibly alters the modal properties.

It is noteworthy that the local Bayes factors at A5 and A10, which are nearest to the Ab2 abutment, are simultaneously altered with the seasonal fluctuation as shown in Figure 7.13. The ones at A6 that is near to the Ab1 abutment is also altered together. That is possibly because the changes in the boundary conditions affect to the modal deformation nearby the abutment. According to those results, it is perhaps

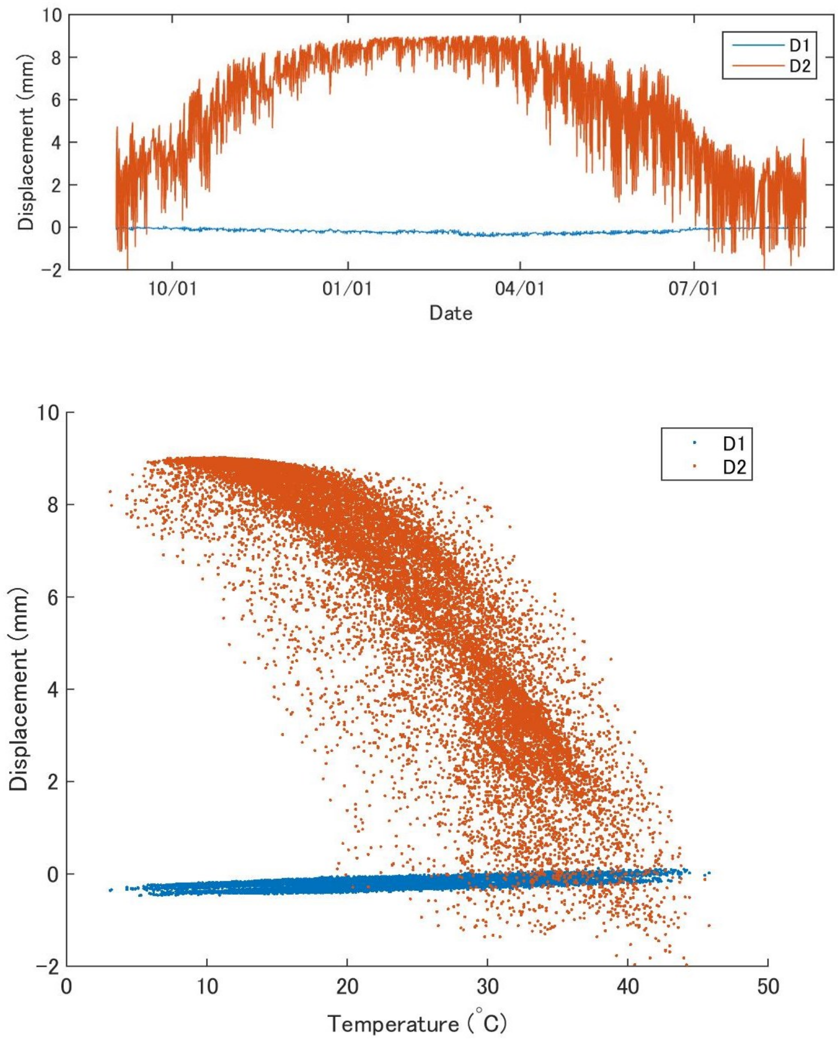

a)

b)

Figure 7.14 Deformation of the supports:

a) Time series (Sep 2016-Aug 2017); b) Scatter diagram with respect to the temperature.

possible to describe relationship between the damage sensitive features and the temperature through the local Bayes factors. Furthermore, advanced machine learning algorithms are feasible to search out this relationship automatically. Further fundamental investigations are also desired considering the seasonal fluctuation of boundary conditions through the experimental model updating in the FE model to realize a reliable damage detection method for long-term health monitoring.

7.4 Damage Experiment

7.4.1 Bayes factors

The Bayes factors are also examined for the damage experiment on the target bridge. Time series are extracted from the vehicle entrance to 5 seconds after the exit as the same way as mentioned in

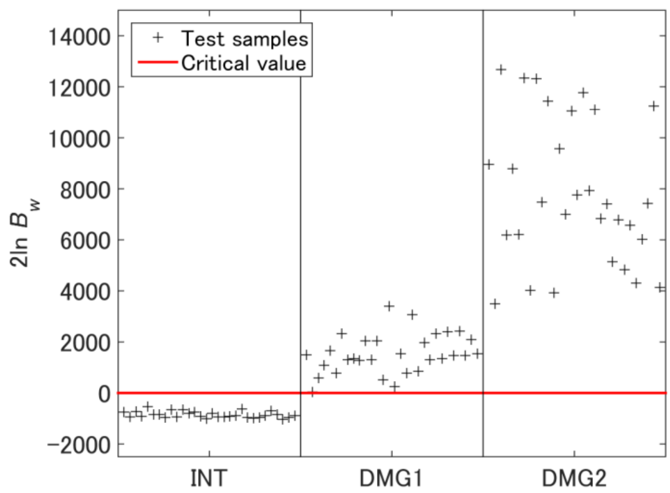

a)

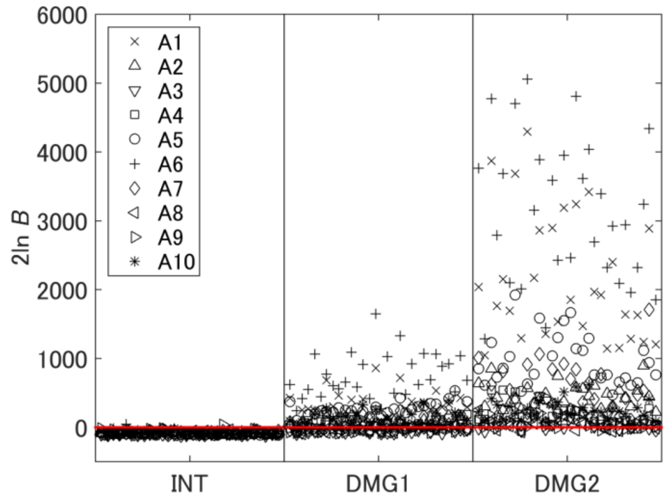

b)

Figure 7.15 Bayes factors for the damage experiment: a) Global Bayes factor; b) Local Bayes factor.

Section 7.3.1 for each of the vehicle loadings. The adopted AR order and the order for feature extraction are also same as discussed in Section 7.3.1, i.e., p=80 and q=12. The first 30 samples measured under the INT scenario are adopted as the reference dataset. The latter 30 samples are adopted as test samples for validation. Note that the cross variation method mentioned in Chapter 5 and Chapter 6 is not adopted in this experiment since sufficient amount of reference data is available. The time series measured under DMG1 and DMG2 scenarios are also adopted as the test samples.

Figure 7.15 shows the observed global and local Bayes factors. The global Bayes factors in Figure 7.15a promptly enable to detect changes in modal properties due to damage like the case study mentioned in Chapter 6. Furthermore, the severity of the damage is successfully quantified in the results. It is also noteworthy that the local Bayes factors at A1 and A6, which are nearest to the Ab1 abutment, are relatively higher than the others are as shown in Figure 7.15b. Although the precise location of the damage is not identified from those results since the local Bayes factors at A6 provides relatively higher values than A1 that is nearer to the damage location, rough estimation of the damage location is still possible. According to the discussion in Section 7.3.2, this result are probably not due to the daily temperature fluctuation since the local Bayes factors at A10 provide lower values than the others.

7.4.2 Natural frequencies

Hereafter the natural frequencies identified from the SSI are examined. The feature extraction for the torsional modes are more difficult than for the bending modes in this study. The 1st, 2nd and 3rd bending modes are thus examined for instance. Mean values of the identified frequencies for the 1st, 2nd and 3rd bending modes before damage experiment were 3.16Hz, 9.55Hz and 21.88Hz, respectively. The identified frequencies were slightly different from frequencies identified from the monitoring data before the damage experiment, as the identified frequencies from the damage experiment can be influenced by the protection devices on the bridge.

Histograms of the identified frequencies from the monitoring data in each bridge condition are shown in Figure 7.16 with normal distribution fits, where the bin width was chosen as 0.01Hz. The histogram was created utilizing 30 samples of the identified frequencies. The statistical distribution showed that frequency distributions for the 2nd and 3rd bending modes moved to lower frequency region as damage becomes severe, i.e. those distributions for the DMG1 and DMG2 scenarios moved to the lower frequency region from the distribution of the INT scenario. It demonstrates decrease of bending stiffness of the plate girder due to the artificial damage. Those results are comparable to the results of the eigenvalue analysis listed in Table 7.1. However, for the frequency distribution of the 1st bending mode moved toward higher frequency region. Aiming at detailed FE model-based inspection, further investigations are needed to establish reasonable FE models representing mechanical properties of actual bridges.

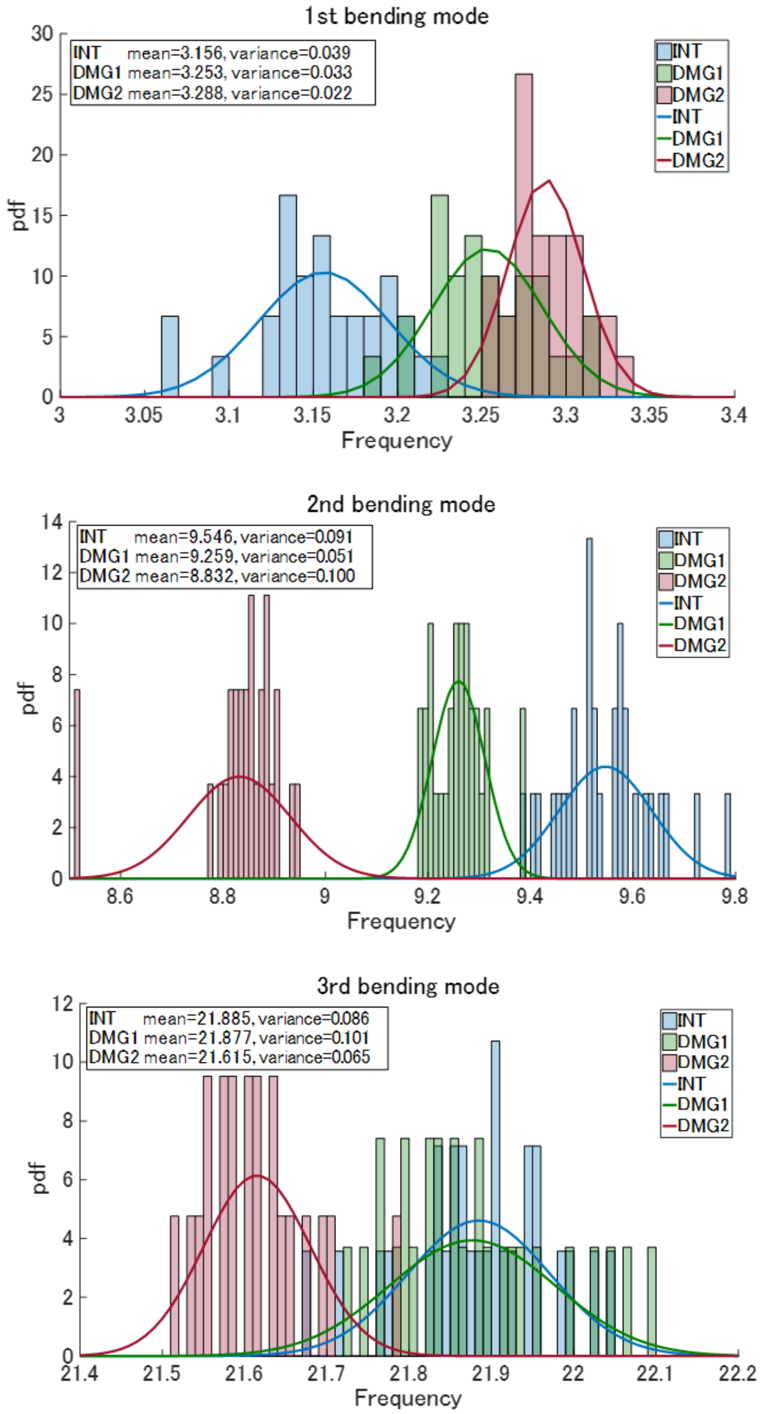

Figure 7.16 Histograms of the identified natural frequencies of the bending modes (Hz).

7.5 Summary

This chapter showed a case study utilizing one-year monitoring data on a plate girder bridge aiming at further investigations for practical long-term health monitoring. After the one-year monitoring, a damage experiment was conducted with artificial damages imitating fatigue crack at the girder end. Finite element model were firstly established through a model updating method using the experimental data. The modal properties for intact and damaged state were examined by eigenvalue analysis.

The Bayes factor proposed in Chapter 6 was applied throughout the one-year monitoring. On-site signal processing method was experimentally established to monitor the Bayes factors. The feature extraction procedure using the stabilization diagram ensued that the experimentally extracted features are actually relevant to the modal properties by comparing the extracted modal deformation to the eigenvalue analysis resulted from the FE model. The monitored Bayes factor clearly indicated seasonal fluctuation appeared in the modal properties. The local Bayes factor, which is calculated for each of the measurement locations, were especially sensitive to the seasonal fluctuation at specific locations. The displacement monitored at the both end of the girder suggested the seasonal fluctuation is possibly due to the deformation of its cantilever-like support.

Anomaly due to the artificial fatigue cracks were successfully detected by the proposed Bayes factor. The local Bayes factor roughly describe the damage location. Additionally, natural frequencies for the dominant bending modes are identified by SSI. The results were mostly comparable to the results of eigenvalue analysis. Further investigations are desired both from theoretical and experimental aspects. For instance, model updating of the FE model by the experimental data possibly enables to investigate relationship between the modal properties and the boundary condition. Those fundamental investigations will expectedly lead to the further studies to handle temperature effect and to establish a more practical long-term health monitoring strategy.

Chapter 8

Conclusion and Open Problems

8.1 Conclusions

Aiming at efficient inspection based on the vibration monitoring, this thesis investigated a damage indicator by unsupervised machine learning. The healthy condition of a bridge is learned at first from the vibration actually monitored on the healthy bridge. Newly observed data is secondly examined whether the bridge is healthy or not. Bayesian statistics enabled the machine learning with a suitable stochastic model to represent random bridge vibrations. Technically, the following two problems lay in the above damage detection procedure:

- How to describe random vibration of bridges
- How to distinguish damage from huge amount of data

This thesis focused to investigate damage detection method dealing with the above problems. The contents of this thesis briefly can be summarized as follows:

In Chapter 1, the background involved in the bridge health monitoring is introduced reviewing the former related studies. The objective of this research is settled to damage detection using vehicle-induced acceleration data measured on bridges. The proposed damage detection is investigated through unsupervised machine learning by means of Bayesian statistics. A target bridge for case studies is introduced in this chapter for the following discussion.

In Chapter 2, the mathematical framework for the Bayesian damage detection is provided. This chapter therefore establishes the foundation to make reliable decision for management of bridge safety based upon probability theory and modal analysis theory. The probability theory is introduced to describe the random phenomena. Bayesian and frequentist viewpoints are mutually introduced. Especially for a linear regressive model, which are essential for identification of modal properties, estimation and inference procedures are provided. This chapter also provides basic models of vibrating structures. A dynamical finite element (FE) model was assumed to describe vibrating structure. Form the FE model, time invariant state space model was transformed to. The state space model was approximated to simplified models, which is so-called autoregressive (AR) model. These models are essential to the modal analysis appearing in the following chapters.

Chapter 3 reviewed modal analysis methods for the following chapters. Brief case studies for the Yule-Walker (YW) method and the stochastic subspace identification (SSI) are provided. Information criteria, which is widely used for model selection, are examined for the regressive time domain models. Bayesian information criterion is suited for the model selection to determine an informative regressive model. The stabilization diagram provides prompt way for feature extraction to find physically meaningful poles. According to the case study of the truss bridge, for precise identification of higher modes, the SSI is more useful than the YW method. However, the YW method is still useful for identification of dominant modes in practice because of its prompt numerical procedure.

In Chapter 4, the uncertainty involved in mode identification was investigated through a case study on a multi-span cable-stayed bridge. SSI and Bayesian operational modal analysis (BAYOMA) were applied to identify modal properties. YW method was not suitable because of the high degree of freedom multiple measurement. Stabilization diagrams of given data were examined to extract stable modes for SSI. For BAYOMA, the posterior distribution of the modal properties were briefly investigated through their coefficient of variance. The stabilization diagrams of data measured under weak wind conditions showed widely scattered unstable poles in the frequency band below 0.23 Hz. The posterior distribution obtained by BAYOMA briefly provided relevant results to the above observations. This observation demonstrated feasibility of the Bayesian inference to quantify uncertainty involved in modal identification. Although BAYOMA enables to produce reliable results quantifying the uncertainty involved in the identified mode, it requires preliminaly analysis in frequency domain to choose proper frequency band to be analysed.

Chapter 5 provided a damage detection method using the novel damage indicator obtained from ambient vibrations of bridges. The damage indicator was derived from a multivariate AR model by evaluating the stochastic distance between a set of reference samples obtained from healthy bridge and unknown test samples using the Mahalanobis distance (MD). Statistical hypothesis testing based on a probability distribution of the damage sensitive features was applied for damage detection using Hotelling's T^2 statistics. The proposed damage detection method enabled to detect three damage patterns clearly. Especially using the free vibration data after the vehicle exits the bridge improved damage detection performance of the T^2 statistics. Note that the forced vibration data are still useful since data truncation is easier in practice than the free vibration data. Although the proposed method improved damage detection performance of the damage indicator compared to previous studies, the proposed method involve disadvantage in model selection. That is, the proposed method only enables to extract feature from roughly estimated mechanical model.

In Chapter 6, the Bayesian hypothesis testing is adopted to the damage detection. A time series of actually observed accelerations of a bridge provides a likelihood function of a multivariate AR model, which enabled Bayesian inference to find the probability distribution for the regressive parameters. The model selection for the AR order is statistically provided by the Schwarz criterion, which is relevant to the Bayesian information criterion. Feature extraction using a SSI-like procedure is also proposed. Bayesian hypothesis test for damage detection is conducted utilizing the Bayes factors, namely, generalized likelihood ratio from the viewpoint of Bayesian statistics. The proposed Bayes Factors detected three different damage levels successfully. The proposed Bayes factors appear to evaluate severity of the damage. For serious damage scenarios, where the truss members were thoroughly ruptured, the Bayes factors locally provide significant values at the measurement points closest to the damaged members. This result suggests possibility of damage localization for severely damaged members. Compared to the previously examined damage indicator in Chapter 5, the proposed methods shows several advantages in practical use. Especially, the proposed feature extraction method enables to reduce the unexpected noise effect.

Chapter 7 showed a case study utilizing one-year monitoring data on a plate girder bridge aiming at further investigations for practical long-term health monitoring. The Bayes factor proposed in Chapter 6 was applied throughout the one-year monitoring. On-site signal processing method was experimentally established to monitor the Bayes factors. The feature extraction procedure ensued that the experimentally extracted features are actually relevant to the modal properties by comparing to a FE model. The monitored Bayes factor clearly indicated seasonal fluctuation appeared in the modal properties. The local Bayes factors at specific locations were especially sensitive to the seasonal fluctuation. After the one-year monitoring, a damage experiment was conducted with artificial damages imitating fatigue crack at the girder end. Anomaly due to the artificial fatigue cracks were successfully detected by the Bayes factor. The local Bayes factor roughly describe the damage location. This observation suggests possibility to distinguish whether the changes in the modal properties are due to damage or fluctuation of temperature.

From the above discussions, the following outcomes are provided concerning damage detection:

- The proposed Bayes factor can be a feasible damage indicator at least for simply supported truss bridges and plate girder bridges with multiple measurement of accelerations on their bridge decks. Ruptures on truss members and fatigue cracks on a main girder are successfully detected.

- Feature extraction method mentioned in Chapter 6 is possibly competitive with SSI since the stabilization diagram enables prompt modal identification.
- The proposed Bayesian inference provides the probability distribution of the AR coefficients. This distribution quantify the uncertainty involved in the parameters as well as BAYOMA.
- Quantification of damage level for the rupture and fatigue cracks is probably realized by the global Bayes factor.
- Damage localization appears sometimes possible by examining the local Bayes factors. For truss bridges, when one of the member is completely ruptured, the localization will be available. For girder bridges, fatigue cracks on their main girder may roughly localized.

Additionally, observations about modal identification in this thesis are summarized as follows:

- The YW method, which is one of the simplest time domain operational modal analysis, is suited for a brief identification of dominant modes. For higher modes, identified results tend to be unstable because of the spurious poles that obstruct feature extraction for physically meaningful poles. The YW method is not suited for higher degree of freedom multiple measurement either because of the spurious poles.
- The SSI provides reliable results for higher order modes since its model reduction procedure by singular value decomposition enables to provide stable feature extraction. The information criteria such as Akaike information criterion and Bayesian information criterion for the autoregressive moving average model are possibly helpful to find proper size of the Henkel matrix before the model reduction.
- The BAYOMA also provides reliable results except damping ratios. Furthermore, the BAYOMA enables to quantify uncertainty of the identified results through the probability density. Since the optimization algorithm operated on a extracted frequency band, it is expected that the identified results are less affected by the signal coming from the other frequency bands. This characteristic however requires preliminary analysis to find proper frequency band. Singular value spectrum is recommended for the multiple measurement to grasp the proper frequency band.

8.2 Open Problems

Although this thesis provides a statistical framework to find changes in modal properties, there remained several tasks for practical use. The open problems are summarized as follows:

Scope of application

This thesis shows the proposed damage detection is suitable for short span bridges with simple geometry such as single-span plate girder bridges and Warren truss bridges. However, structures with more complicated geometry producing complicated modal response may involve difficulty for application. Further investigations for various kinds of bridges are thus desirable to settle scope of application. The optimization of the sensor location is one related problem. Although multipoint measurement is better for damage detection, the number of available sensor may be limited in practice. Further discussions are needed to determine how to optimize the sensor location according to the geometry of the structure.

Fluctuations in long term monitoring

As mentioned in Chapter 7, seasonal fluctuation can considerably alter the modal properties. Furthermore, as mentioned in Chapter 4, large scale structures sometimes show complicated behavior relying on the ambient excitation. These fluctuations should be handled in long term monitoring to support decision making for bridge management. The discussion in Chapter 7 suggested possibility to distinguish whether the changes in the modal properties are due to damage or merely the fluctuation. However to make reasonable decision rule for damage detection in long term monitoring, further investigations are necessary both from theoretical and experimental aspects. Model updating of the FE model by the experimental data possibly enables to investigate relationship between the modal properties and the boundary condition.

Further investigation for modal analysis

The proposed Bayesian inference provides the probability distribution of the AR coefficients. The probability densities of the modal properties also can be obtained since they are transformed from the AR coefficients. Furthermore, the modal properties are promptly observed by the proposed feature extraction using stabilization diagrams. These outcomes suggest that the probability densities of the modal properties enable to quantify the uncertainty of the properties as well as BAYOMA. Furthermore, the regressive models are possibly expanded to autoregressive moving average model, which is relevant to SSI. Thus, the proposed Bayesian inference may possibly provide a novel framework competitive with SSI and BAYOMA for modal analysis.

References

[1] National Transportation Safety Board, *Collapse of I-35W Highway Bridge Minneapolis, Minnesota August 1, 2007*. Washington DC.: Highway Accident Report NTSB/HAR-08/03, 2008.

[2] K. Yamada, "An advice from rupture into a diagonal member of Kisogawa bridge," *JSCE Mag Civ Eng.*, vol. 93, no. 1, pp. 29–30, 2008. (In Japanese)

[3] Ministry of Land Infrastructure Transport and Tourism in Japan, *White Paper on Land, Infrastructure, Transport and Tourism in Japan, 2015*. 2016.

[4] Ministry of Land Infrastructure Transport and Tourism, *Anual Report on Road Maintenace*. 2016. (In Japanese)

[5] *The Bridge Management System -Practice and Methodology -*. Shinjuku: Japan Society of Civil Engineers, 2016. (In Japanese)

[6] G. W. Housner *et al.*, "Structural Control : Past, Present, and Future," *J. Eng. Mech.*, vol. 123, no. 9, pp. 897–971, 1997.

[7] S. W. S. Doebling, C. R. C. Farrar, M. B. M. Prime, and D. W. D. Shevitz, *Damage identification and health monitoring of structural and mechanical systems from changes in their vibration characteristics: a literature review*. Los Alamos National Laboratory Report LA-13070-MS, 1996.

[8] O. S. Salawu, "Detection of structural damage through changes in frequency: a review," *Eng. Struct.*, vol. 19, no. 9, pp. 718–723, 1997.

[9] B. Peeters, "System identification and damage detection in civil engineering - PhD Thesis," 2000.

[10] P. Gudmundson, "Eigenfrequency changes of structures due to cracks, notches or other geometrical changes," *J. Mech. Phys. Solids*, vol. 30, no. 5, pp. 339–353, 1982.

[11] A. K. Pandey, M. Biswas, and M. M. Samman, "Damage detection from changes in curvature mode shapes," *J. Sound Vib.*, vol. 145, no. 2, pp. 321–332, 1991.

[12] A. K. Pandey and M. Biswas, "Damage detection in structures using changes in flexibility," *Journal of Sound and Vibration*, vol. 169, no. 1. pp. 3–17, 1994.

[13] R. J. Savage and P. C. Hewlett, "A new ndt method for structural integrity assessment," *NDT Int.*, vol. 11, no. 2, pp. 61–67, 1978.

[14] B. M. Kato and S. Shimada, "Vibration of PC bridge during failure process," *J. Struct. Eng.*, vol. 112, no. 7, pp. 1692–1703, 1986.

[15] D. F. Mazurek and J. T. DeWolf, “Experimental study of bridge monitoring technique,” *J. Struct. Eng.*, vol. 116, no. 9, pp. 2532–2549, 1990.

[16] V. G. Idichandy and C. Ganapathy, “Modal parameters for structural integrity monitoring of fixed offshore platforms,” *Exp. Mech.*, vol. 30, no. 4, pp. 382–391, 1990.

[17] M. Shinozuka and R. Ghanem, “Structural system identification. II: Experimental verification,” *J. Eng. Mech.*, vol. 121, no. 2, pp. 265–273, 1995.

[18] W. X. Ren and G. De Roeck, “Structural damage identification using modal data. II: Test verification,” *J. Struct. Eng.*, vol. 128, no. 1, pp. 96–104, 2002.

[19] A. Deraemaeker, E. Reynders, G. De Roeck, and J. Kullaa, “Vibration-based structural health monitoring using output-only measurements under changing environment,” *Mech. Syst. Signal Process.*, vol. 22, no. 1, pp. 34–56, 2008.

[20] R. O. Curadelli, J. D. Riera, D. Ambrosini, and M. G. Amani, “Damage detection by means of structural damping identification,” *Eng. Struct.*, vol. 30, no. 12, pp. 3497–3504, 2008.

[21] Y. L. Zhou, N. M. M. Maia, R. P. C. Sampaio, and M. A. Wahab, “Structural damage detection using transmissibility together with hierarchical clustering analysis and similarity measure,” *Struct. Heal. Monit.*, vol. 16, no. 6, pp. 771–731, 2017.

[22] Q. W. Zhang, “Statistical damage identification for bridges using ambient vibration data,” *Comput. Struct.*, vol. 85, no. 7–8, pp. 476–485, 2007.

[23] M. Gul and F. Necati Catbas, “Statistical pattern recognition for Structural Health Monitoring using time series modeling: Theory and experimental verifications,” *Mech. Syst. Signal Process.*, vol. 23, no. 7, pp. 2192–2204, 2009.

[24] G. Comanducci, F. Magalhães, F. Ubertini, and Á. Cunha, “On vibration-based damage detection by multivariate statistical techniques: Application to a long-span arch bridge,” *Struct. Heal. Monit.*, vol. 15, no. 5, 2016.

[25] X. Jiang and S. Mahadevan, “Bayesian wavelet methodology for structural damage detection,” *Struct. Control Heal. Monit.*, vol. 15, no. 7, pp. 974–991, 2008.

[26] X. D. Sun, X. Y. Sun, J. He, and G. L. Hou, “Bayesian-based structural damage detection on the integration of global and local information,” *Adv. Struct. Eng.*, vol. 18, no. 4, pp. 543–553, 2015.

[27] Z. Dzunic, J. G. Chen, H. Mobahi, O. Büyüköztürk, and J. W. Fisher, “A Bayesian state-space approach for damage detection and classification,” *Mech. Syst. Signal Process.*, vol. 96, pp. 239–259, 2017.

[28] H. Sohn, C. R. Farrar, F. Hemez, and J. Czarnecki, “A review of structural health monitoring literature 1996 – 2001,” in *Third World Conference on Structural Control*, pp. 1–7, 2002.

[29] M. Döhler, X. B. Lam, and L. Mevel, “Uncertainty quantification for modal parameters from

stochastic subspace identification on multi-setup measurements," *Mech. Syst. Signal Process.*, vol. 36, no. 2, pp. 562–581, 2013.

[30] E. Figueiredo, L. Radu, K. Worden, and C. R. Farrar, "A Bayesian approach based on a Markov-chain Monte Carlo method for damage detection under unknown sources of variability," *Eng. Struct.*, vol. 80, pp. 1–10, 2014.

[31] R. Ghiasi, P. Torkzadeh, and M. Noori, "A machine-learning approach for structural damage detection using least square support vector machine based on a new combinational kernel function," *Struct. Heal. Monit.*, vol. 15, no. 3, pp. 302–316, 2016.

[32] K. Worden and P. L. Green, "A machine learning approach to nonlinear modal analysis," *Mech. Syst. Signal Process.*, vol. 84, pp. 34–53, 2017.

[33] W. Gersch, N. N. Nielsen, and H. Akaike, "Maximum likelihood estimation of structural parameters from random vibration data," *J. Sound Vib.*, vol. 31, no. 3, pp. 295–308, 1973.

[34] M. Hoshiya and E. Saito, "Structural identification by extended Kalman filter," *J. Eng. Mech.*, vol. 110, no. 12, pp. 1757–1770, 1984.

[35] W. Heylen, S. Lammens, and P. Sas, *Modal Analysis Theory and Testing*. Leuven: KU Leuven, 1997.

[36] X. He and G. De Roeck, "System identification of mechanical structures by a high-order multivariate autoregressive model," *Comput. Struct.*, vol. 64, no. 1, pp. 341–351, 1997.

[37] B. Peeters and G. De Roeck, "Reference-based stochastic subspace identification for output-only modal analysis," *Mech. Syst. Signal Process.*, vol. 13, no. 6, pp. 855–878, 1999.

[38] R. Brincker and et al., "Modal identification of output-only systems using frequency domain decomposition," *Smart Mater. Struct.*, vol. 10, no. 3, p. 441, 2001.

[39] B. Peeters, G. Patrick, V. D. A. Herman, C. Bart, V. Peter, and L. Jan, "Automotive and aerospace applications of the PolyMAX modal parameter estimation method," *Proc. IMAC*, vol. 22, no. 1, 2004.

[40] B. Peeters, H. Van Der Auweraer, P. Guillaume, and J. Leuridan, "The PolyMAX frequency-domain method : a new standard for modal parameter estimation?," *Shock Vib.*, vol. 11, pp. 395–409, 2004.

[41] B. Peeters, F. Dammekens, F. Magalhães, H. Auweraer, E. Caetano, and Á. Cunha, "Multi-run operational modal analysis of the Guadiana cable-stayed bridge," *IMAC XXIV - A Conf. Expo. Struct. Dyn.*, no. 1, pp. 165–177, 2006.

[42] K. Yuen and L. S. Katafygiotis, "Bayesian time-domain approach for modal updating using ambient data," *Probabilistic Eng. Mech.*, vol. 16, 2001.

[43] K. Yuen and L. Katafygiotis, "Bayesian fast Fourier transform approach for modal updating using ambient data," *Adv. Struct. Eng.*, vol. 6, no. 2, pp. 81–95, 2003.

[44] S. K. Au, “Fast Bayesian ambient modal identification in the frequency domain, Part I: Posterior most probable value,” *Mech. Syst. Signal Process.*, vol. 26, no. 1, pp. 60–75, 2012.

[45] S. K. Au, “Fast Bayesian ambient modal identification in the frequency domain, Part II: Posterior uncertainty,” *Mech. Syst. Signal Process.*, vol. 26, no. 1, pp. 76–90, 2012.

[46] S. K. Au, F. L. Zhang, and Y. C. Ni, “Bayesian operational modal analysis: Theory, computation, practice,” *Comput. Struct.*, vol. 126, pp. 3–14, 2013.

[47] P. van Overschee and B. De Moor, *Subspace identification for linear systems*. Norwell: Kluwer Academic Publishers, 1996.

[48] C. S. Huang, “Structural identification from ambient vibration measurement using the multivariate AR model,” *J. Sound Vib.*, vol. 241, no. 3, pp. 337–359, 2001.

[49] Y. Goi and C. W. Kim, “Mode identifiability of a multi-span cable-stayed bridge utilizing stabilization diagram and singular values,” *Smart Struct. Syst.*, vol. 17, no. 3, pp. 391–411, Mar. 2016.

[50] K. C. Chang and C. W. Kim, “Modal-parameter identification and vibration-based damage detection of a damaged steel truss bridge,” *Eng. Struct.*, vol. 122, pp. 156–173, 2016.

[51] C. W. Kim, K. C. Chang, S. Kitauchi, and P. J. McGetrick, “A field experiment on a steel Gerber-truss bridge for damage detection utilizing vehicle-induced vibrations,” *Struct. Heal. Monit.*, vol. 15, no. 2, pp. 174–192, 2016.

[52] B. Peeters and G. De Roeck, “One-year monitoring of the Z 24-Bridge: environmental effects versus damage events,” *Earthq. Eng. Struct. Dyn.*, vol. 30, no. 2, pp. 149–171, 2001.

[53] Y. Q. Ni, Y. W. Wang, and Y. X. Xia, “Investigation of mode identifiability of a cable-stayed bridge: comparison from ambient vibration responses and from typhoon-induced dynamic responses,” *Smart Struct. Syst.*, vol. 15, no. 2, pp. 447–468, 2015.

[54] C. W. Kim, M. Kawatani, and J. Hao, “Modal parameter identification of short span bridges under a moving vehicle by means of multivariate AR model,” *Struct. Infrastruct. Eng.*, vol. 8, no. 5, pp. 459–472, 2012.

[55] K. K. Nair, A. S. Kiremidjian, and K. H. Law, “Time series-based damage detection and localization algorithm with application to the ASCE benchmark structure,” *J. Sound Vib.*, vol. 291, no. 1–2, pp. 349–368, 2006.

[56] C. W. Kim, R. Isemoto, K. Sugiura, and M. Kawatani, “Structural fault detection of bridges based on linear system parameter and MTS method,” *J. JSCE*, vol. 1, no. 1, pp. 32–43, 2013.

[57] C. M. Bishop, *Pattern Recognition and Machine Learning*. New York: Springer, 2006.

[58] P. D. Welch, “The use of fast Fourier transform for the estimation of power spectra a method based on time averaging over short, modified periodograms,” *IEEE Trans. Audio Electroacoust.*, vol. 15,

no. 2, pp. 70–73, 1967.

[59] A. N. Kolmogorov, *Foundations of the Theory of Probability*, 2nd ed. Mansfield: Martino, 1956.

[60] H. Jeffreys, “An invariant form for the prior probability in estimation problems,” in *Proceedings of the Royal Society of London*, vol. 186, pp. 453–461, 1946.

[61] J. M. Bernardo and A. F. M. Smish, *Bayesian Theory*. Hoboken: Wiley, 1994.

[62] J. N. Juang, *Applied System Identification*. Upper Saddle River: Prentice Hall PTR, 1994.

[63] A. V. Oppendeim, A. S. Willsky, and S. H. Nawab, *Signals & Systems*, 2nd ed. Upper Saddle River: Pearson Education, 1997.

[64] H. Akaike, “Markovian representation of stochastic processes and its application to the analysis of autoregressive moving average processes,” *Ann. Inst. Stat. Math.*, vol. 26, no. 1, pp. 363–387, 1974.

[65] T. Okabayashi, T. Naka, T. Okumatsu, and H. Jiexin, “Estimation of structural dynamic properties by a multivariate autoregressive process with ambient vibration data,” *J. JSCE series A*, vol. 64, no. 2, pp. 474–487, 2008 (In Japanese).

[66] K. S. Arun and S. Y. Kung, “Balanced approximation of stochastic systems,” *SIAM J. Matrix Anal. Appl.*, vol. 11, no. 1, pp. 42–68, 1990.

[67] L. S. Katafygiotis and K. V. Yuen, “Bayesian spectral density approach for modal updating using ambient data,” *Earthq. Eng. Struct. Dyn.*, vol. 30, no. 8, pp. 1103–1123, 2001.

[68] Y. GOI, C. W. KIM, and S. K. AU, “Investigation of operational modal identification of a cable-stayed bridge based on Bayesian estimation considering stochastic uncertainty,” *J. JSCE series A2*, vol. 72, no. 2, p. I_751-I_762, 2016. (In Japanese)

[69] H. Akaike, “A new look at the statistical model identification,” *IEEE Trans. Automat. Contr.*, vol. 19, no. 6, pp. 716–723, 1974.

[70] R. Bergermann and M. Schlaich, “Ting Kau Bridge, Hong Kong,” *Struct. Eng. Int.*, vol. 6, no. 3, pp. 152–154, 1996.

[71] J. M. Ko and Y. Q. Ni, “Technology developments in structural health monitoring of large-scale bridges,” *Eng. Struct.*, vol. 27, pp. 1715–1725, 2005.

[72] K. Y. Wong, “Instrumentation and health monitoring of cable-supported bridges,” *Struct. Control Heal. Monit.*, vol. 11, pp. 91–124, 2004.

[73] K. Y. Wong and Y. Q. Ni, “Modular architecture of SHM system for cable-supported bridges,” in *Encyclopedia of Structural Health Monitoring*. New York: Wiley, 2009.

[74] Y. Q. Ni, K. Y. Wong, and Y. Xia, “Health checks through landmark bridges to sky-high Structures,” *Adv. Struct. Eng.*, vol. 14, no. 1, pp. 103–119, 2011.

[75] *Digital Signal Processing Committee of the IEEE Acoustics, Speech, and Signal Processing Society*.

New York: IEEE Press, 1979.

[76] R. W. Daniels, *Approximation Methods for Electronic Filter Design*. New York: McGraw-Hill, 1974.

[77] R. Brincker, L. Zhang, and P. Andersen, “Modal identification from ambient responses using frequency domain decomposition,” in *Proceedings of SPIE - The International Society for Optical Engineering*, vol. 4062, 2000.

[78] S. K. Au and I. Yoshida, “Theory and practice of Bayesian modal identification using ambient data,” *J. JSCE A2*, vol. 68, no. 2, pp. 59–67, 2012.

[79] P. C. Mahalanobis, “On the generalised distance in statistics,” in *Proceedings of the National Institute of Sciences of India*, pp. 49–55, 1936.

[80] G. Taguchi and J. Rajesh, “New trends in multivariate diagnosis,” *Indian J. Stat.*, vol. 62, no. B2, pp. 233–248, 2000.

[81] I. T. Jolliffe, *Principal component analysis*. New York: Springer, 2002.

[82] C. Kim, S. Kitauchi, K. Sugiura, and M. Kawatani, “Utilizing reproduced autoregressive model for damage detection of real truss bridges,” in *4th International Symposium on Life-Cycle Civil Engineering*, 2014, pp. 369–376.

[83] H. Hotelling, “The generalization of student’s ratio,” *Ann. Math. Stat.*, vol. 2, no. 3, pp. 360–378, 1931.

[84] R. J. Muirhead, *Aspects of Multivariate Statistical Theory*, 2nd ed. Hoboken: Wiley, 2005.

[85] Y. Goi and C. W. Kim, “Damage detection of a truss bridge utilizing a damage indicator from multivariate autoregressive model,” *J. Civ. Struct. Heal. Monit.*, vol. 7, no. 2, pp. 153–162, 2017.

[86] R. Kass and A. Raftery, “Bayes Factors,” *Journal of the American Statistical Association*, vol. 90, no. 430. pp. 773–795, 1995.

[87] R. E. Kass and L. Wasserman, “A reference Bayesian test for nested hypotheses and its relationship to the Schwarz criterion,” *Journal of the American Statistical Association*, vol. 90, no. 431. pp. 773–795, 1995.

[88] G. Schwarz, “Estimating the dimension of a model,” *Ann. Stat.*, vol. 6, no. 2, pp. 461–464, 1978.

[89] B. W. J. Cody and K. E. Hillstrom, “Chebyshev approximations for the natural logarithm of the gamma gunction,” *Math. Comp.*, vol. 21, pp. 198–203, 1967.

[90] S. S. Wilks, “The large-sample distribution of the likelihood ratio for testing composite hypotheses,” *Ann. Math. Stat.*, vol. 9, no. 1, pp. 60–62, 1938.

[91] C. Kim, T. Morita, Y. Oshima, and K. Sugiura, “A Bayesian approach for vibration-based long-term bridge monitoring to consider environmental and operational changes,” *Smart Structures and Systems*, Vol. 15, No. 2, pp. 395–408, 2015.

[92] P. J. McGetrick, C. W. Kim, A. González, and E. J. O. Brien, “Experimental validation of a drive-by stiffness identification method for bridge monitoring,” *Struct. Heal. Monit.*, vol. 14, no. 4, pp. 317–331, 2015.

Appendix

Noninformative prior

According to Eq. 2.29, the log likelihood function of linear regressive models for univariate target variable $t \in \mathbb{R}$ and input variables $\boldsymbol{x} \in \mathbb{R}^{D\times 1}$ is given as follows.

$$\ln p(t|\boldsymbol{w},\beta) = \frac{1}{2}\ln\beta - \frac{1}{2}\ln(2\pi) - \frac{\beta}{2}(t - \boldsymbol{w}^{\mathrm{T}}\boldsymbol{x})^2 \tag{A1}$$

Letting $p(\boldsymbol{x})$ represent the PDF for $\boldsymbol{x}$, the joint PDF for t and $\boldsymbol{x}$ is given as

$$p(t,\boldsymbol{x}|\boldsymbol{w},\beta) = p(t|\boldsymbol{x},\boldsymbol{w},\beta)p(\boldsymbol{x}) \tag{A2}$$

Note that $\boldsymbol{x}$ is independent from $\boldsymbol{w}$ and β. Thus, log function of the joint PDF is given as follows.

$$\ln p(t,\boldsymbol{x}|\boldsymbol{w},\beta) = \frac{1}{2}\ln\beta - \frac{1}{2}\ln(2\pi) - \frac{\beta}{2}(t - \boldsymbol{w}^{\mathrm{T}}\boldsymbol{x})^2 + \ln p(\boldsymbol{x}) \tag{A3}$$

Accordingly, the Fisher's information matrix is given as

$$\boldsymbol{H}(\boldsymbol{w},\beta) = \begin{bmatrix} \boldsymbol{H}_{11}(\boldsymbol{w},\beta) & \boldsymbol{H}_{12}(\boldsymbol{w},\beta) \\ \boldsymbol{H}_{12}(\boldsymbol{w},\beta)^{\mathrm{T}} & \boldsymbol{H}_{22}(\boldsymbol{w},\beta) \end{bmatrix} \tag{A4}$$

where,

$$[\boldsymbol{H}_{11}(\boldsymbol{w},\beta)]_{ij} = -\mathbb{E}_{t,\boldsymbol{x}}\left[\frac{\partial^2}{\partial w_i \partial w_j} \ln p(t|\boldsymbol{w},\beta) \middle| \boldsymbol{w},\beta\right], (i,j = 1,\dots,D), \tag{A5}$$

$$[\boldsymbol{H}_{12}(\boldsymbol{w},\beta)]_{i} = -\mathbb{E}_{t,\boldsymbol{x}}\left[\frac{\partial^2}{\partial w_i \partial \beta} \ln p(t|\boldsymbol{w},\beta) \middle| \boldsymbol{w},\beta\right], (i = 1,\dots,D), \tag{A6}$$

$$\boldsymbol{H}_{22}(\boldsymbol{w},\beta) = -\mathbb{E}_{t,\boldsymbol{x}}\left[\frac{\partial^2}{\partial \beta^2} \ln p(t|\boldsymbol{w},\beta) \middle| \boldsymbol{w},\beta\right]. \tag{A7}$$

The first order partial derivatives of $\ln p(t|\boldsymbol{w},\beta)$ with respect to $\boldsymbol{w}$ is given as

$$\frac{\partial}{\partial w_i}\ln p(t,\boldsymbol{x}|\boldsymbol{w},\beta) = -\frac{\beta}{2}\frac{\partial}{\partial w_i}(t - \boldsymbol{w}^{\mathrm{T}}\boldsymbol{x})^2 = \beta(t - \boldsymbol{w}^{\mathrm{T}}\boldsymbol{x})x_i. \tag{A8}$$

Thus, the second order partial derivatives are given as follows.

$$\frac{\partial^2}{\partial w_i \partial w_j} \ln p(t, \boldsymbol{x}|\boldsymbol{w}, \beta) = \beta x_i \frac{\partial}{\partial w_j}(t - \boldsymbol{w}^{\mathrm{T}}\boldsymbol{x}) = -\beta x_i x_j, \tag{A9}$$

$$\frac{\partial^2}{\partial w_i \partial \beta} \ \ln p(t|\boldsymbol{w}, \beta) = (t - \boldsymbol{w}^{\mathrm{T}}\boldsymbol{x})x_i \tag{A10}$$

$$\frac{\partial^2}{\partial \beta^2} \ \ln p(t|\boldsymbol{w}, \beta) = \frac{1}{2}\frac{\partial^2}{\partial \beta^2} \ln \beta = -\frac{1}{2}\beta^{-2} \tag{A11}$$

Noting that the expectation of t is $\boldsymbol{w}^{\mathrm{T}}\boldsymbol{x}$, following relationship is obtained.

$$[\boldsymbol{H}_{11}(\boldsymbol{w}, \beta)]_{ij} = -\mathbb{E}_{t,x}\left[-\beta x_i x_j \middle| \boldsymbol{w}, \beta\right] = \beta \mathbb{E}_{\boldsymbol{x}}[x_i x_j], \tag{A12}$$

$$[\boldsymbol{H}_{12}(\boldsymbol{w}, \beta)]_i = -\mathbb{E}_{t,x}[(t - \boldsymbol{w}^{\mathrm{T}}\boldsymbol{x})x_i \middle| \boldsymbol{w}, \beta] = 0, \tag{A13}$$

$$\boldsymbol{H}_{22}(\boldsymbol{w}, \beta) = -\mathbb{E}_{t,x}\left[-\frac{1}{2}\beta^{-2} \middle| \boldsymbol{w}, \beta\right] = \frac{1}{2}\beta^{-2}. \tag{A14}$$

Therefore, the Fisher's information matrix is obtained as

$$\boldsymbol{H}(\boldsymbol{w}, \beta) = \begin{bmatrix} \beta \mathbb{E}_{\boldsymbol{x}}[\boldsymbol{x}^{\mathrm{T}}\boldsymbol{x}] & 0 \\ 0 & \frac{1}{2}\beta^{-2} \end{bmatrix}. \tag{A15}$$

Accordingly, the Jeffreys prior satisfies following condition.

$$\pi(\boldsymbol{w}, \beta) \propto |\boldsymbol{H}(\boldsymbol{w}, \beta)|^{\frac{1}{2}} = \left|\beta \mathbb{E}_{\mathbf{x}}(\boldsymbol{x}^{\mathrm{T}}\boldsymbol{x})\right|^{\frac{1}{2}} \left(\frac{1}{2}\beta^{-2}\right)^{\frac{1}{2}} \propto \beta^{\frac{D}{2}-1} \tag{A16}$$

The likelihood function for the data set of input variables $\boldsymbol{X} = [\boldsymbol{x}_1, \boldsymbol{x}_2, \ldots, \boldsymbol{x}_N]^{\mathrm{T}} \in \mathbb{R}^{N \times D}$ and target variables $\boldsymbol{t} = [t_1, t_2, \ldots, t_N]^{\mathrm{T}} \in \mathbb{R}^{N \times 1}$ is given as Eq. 2.31 and Eq. 2.32, which are reproduced as follows.

$$p(\boldsymbol{t}|\boldsymbol{w}, \beta) = \left(\frac{\beta}{2\pi}\right)^{\frac{N}{2}} \exp\left(-\frac{1}{2}\beta E(\boldsymbol{w})\right) \tag{A17}$$

$$E(\boldsymbol{w}) = \|\boldsymbol{t} - \boldsymbol{X}\boldsymbol{w}\|^2 \tag{A18}$$

Thus, the Bayes theorem produces the posterior distribution with respect to the Jeffreys prior satisfying the following condition.

$$p(\boldsymbol{w}, \beta|\boldsymbol{t}) \propto p(\boldsymbol{t}|\boldsymbol{w}, \beta)\pi(\boldsymbol{w}, \beta) \propto \beta^{\frac{N+D}{2}-1} \exp\left(-\frac{1}{2}\beta E(\boldsymbol{W})\right) \tag{A19}$$

According to Eq. 2.33, the term $\boldsymbol{X}^{\mathrm{T}}\boldsymbol{t}$ satisfies following relationship with most likelihood of $\mathbf{w}$.

$$\boldsymbol{X}^{\mathrm{T}}\boldsymbol{t} = \boldsymbol{X}^{\mathrm{T}}\boldsymbol{X}\widehat{\boldsymbol{w}}. \tag{A20}$$

Thus, Eq. 2.32 leads following relationship.

$$E(\boldsymbol{w}) - E(\widehat{\boldsymbol{w}}) = -2\boldsymbol{t}^{\mathrm{T}}\boldsymbol{X}(\boldsymbol{w} - \widehat{\boldsymbol{w}}) + \boldsymbol{w}^{\mathrm{T}}\boldsymbol{X}^{\mathrm{T}}\boldsymbol{X}\boldsymbol{w} - \widehat{\boldsymbol{w}}^{\mathrm{T}}\boldsymbol{X}^{\mathrm{T}}\boldsymbol{X}\widehat{\boldsymbol{w}}$$

$$= -2\boldsymbol{w}^{\mathrm{T}}\boldsymbol{X}^{\mathrm{T}}\boldsymbol{X}\widehat{\boldsymbol{w}} + \mathbf{w}^{\mathrm{T}}\boldsymbol{X}^{\mathrm{T}}\boldsymbol{X}\boldsymbol{w} + \widehat{\boldsymbol{w}}^{\mathrm{T}}\boldsymbol{X}^{\mathrm{T}}\boldsymbol{X}\widehat{\boldsymbol{w}}$$
$$= (\boldsymbol{w} - \widehat{\boldsymbol{w}})^{\mathrm{T}}\boldsymbol{X}^{\mathrm{T}}\boldsymbol{X}(\boldsymbol{w} - \widehat{\boldsymbol{w}}). \tag{A21}$$

Assuming $N \gg D$, then $\mathrm{rank}(\boldsymbol{X}) = D$ and $E(\widehat{\boldsymbol{W}}) > 0$ are presumably satisfied. Therefore, the posterior distribution satisfies following relationship.

$$p(\boldsymbol{w}, \beta|\boldsymbol{t}) \propto \beta^{\frac{N+D}{2}-1} \exp\left(-\frac{\beta}{2}\left(E(\widehat{\boldsymbol{w}}) + (\boldsymbol{w} - \widehat{\boldsymbol{w}})^{\mathrm{T}}\boldsymbol{X}^{\mathrm{T}}\boldsymbol{X}(\boldsymbol{w} - \widehat{\boldsymbol{w}})\right)\right)$$
$$\propto N(\boldsymbol{w}|\widehat{\boldsymbol{w}}, (\beta\boldsymbol{X}^{\mathrm{T}}\boldsymbol{X})^{-1})Gam\left(\beta\middle|\frac{N}{2}, \frac{1}{2}E(\widehat{\boldsymbol{w}})\right). \tag{A22}$$

Accordingly,

$$p(\boldsymbol{w}, \beta|\boldsymbol{t}) = N(\boldsymbol{w}|\widehat{\boldsymbol{w}}, (\beta\boldsymbol{X}^{\mathrm{T}}\boldsymbol{X})^{-1})Gam\left(\beta\middle|\frac{N}{2}, \frac{1}{2}E(\widehat{\boldsymbol{w}})\right). \tag{A23}$$

Although the noninformative prior cannot be correctly normalized as mentioned in Section 2.2.3, the posterior PDF given as Eq. A22 can be properly normalized when $\mathrm{rank}(\boldsymbol{X}) = D$ and $E(\widehat{\boldsymbol{w}}) > 0$ are satisfied.

Conjugate priors and marginal likelihood

Conjugate priors produce posterior distributions whose functional forms are same as the priors [57]. This part provides the proof that the conjugate prior for model parameters in AR models has functional form given as Eq. 2.44. The PDF can be expanded as

$$\mathrm{p}(\boldsymbol{w}, \beta) = \mathcal{N}(\boldsymbol{w}|\boldsymbol{m}, (\beta\boldsymbol{L})^{-1})Gam(\beta|a, b) \tag{A24}$$
$$= C(\boldsymbol{L}, a, b)\beta^{a+mp/2-1} \exp\left(-\frac{\beta}{2}((\boldsymbol{w} - \boldsymbol{m})^{\mathrm{T}}\boldsymbol{L}(\boldsymbol{w} - \boldsymbol{m}) + 2b)\right)$$

where $C(\cdot)$ represents the following constant to normalize the PDF, which is referred as normalization factor.

$$C(\boldsymbol{L}, a, b) = (2\pi)^{-mp/2}|\boldsymbol{L}|^{1/2}b^{a}/\Gamma(a) \tag{A25}$$

Thus, Eq. 2.35 and Eq. A17 provides following relationship

$$\mathrm{p}(\boldsymbol{w}, \beta|\boldsymbol{t}) = (2\pi)^{-n/2}C(\boldsymbol{L}, a, b)\mathrm{p}(\boldsymbol{t})^{-1}\beta^{a'+mp/2-1} \tag{A26}$$
$$\times \exp\left(-\frac{\beta}{2}(E(\boldsymbol{w}) + (\boldsymbol{w} - \boldsymbol{m})^{\mathrm{T}}\boldsymbol{L}(\boldsymbol{w} - \boldsymbol{m}) + 2b)\right)$$

where a' and $E(\boldsymbol{w})$ are respectively given as Eq. 2.48 and Eq. A18. Eqs. 2.46 and 2.47 produce following relationship.

$$E(\boldsymbol{w}) + (\boldsymbol{w}-\boldsymbol{m})^{\mathrm{T}}\boldsymbol{L}(\boldsymbol{w}-\boldsymbol{m}) = \boldsymbol{t}^{\mathrm{T}}\boldsymbol{t} - 2\boldsymbol{w}^{\mathrm{T}}(\boldsymbol{X}^{\mathrm{T}}\boldsymbol{t}+\boldsymbol{L}\boldsymbol{m}) + \boldsymbol{w}^{\mathrm{T}}(\boldsymbol{X}^{\mathrm{T}}\boldsymbol{X}+\boldsymbol{L})\boldsymbol{w} + \boldsymbol{m}^{\mathrm{T}}\boldsymbol{L}\boldsymbol{m} \quad \text{(A27)}$$
$$= \boldsymbol{t}^{\mathrm{T}}\boldsymbol{t} - 2\boldsymbol{w}^{\mathrm{T}}\boldsymbol{L}'\boldsymbol{m}' + \boldsymbol{w}^{\mathrm{T}}\boldsymbol{L}'\boldsymbol{w} + \boldsymbol{m}^{\mathrm{T}}\boldsymbol{L}\boldsymbol{m}$$
$$= \boldsymbol{t}^{\mathrm{T}}\boldsymbol{t} + (\boldsymbol{w}-\boldsymbol{m}')^{\mathrm{T}}\boldsymbol{L}'(\boldsymbol{w}-\boldsymbol{m}') - \boldsymbol{m}'^{\mathrm{T}}\boldsymbol{L}'\boldsymbol{m}' + \boldsymbol{m}^{\mathrm{T}}\boldsymbol{L}\boldsymbol{m}$$

Eq. 2.49 produces following relationship.

$$2(b_1-b_0) = E(\boldsymbol{m}') + (\boldsymbol{m}'-\boldsymbol{m})^{\mathrm{T}}\boldsymbol{L}(\boldsymbol{m}'-\boldsymbol{m}) \quad \text{(A28)}$$
$$= \boldsymbol{t}^{\mathrm{T}}\boldsymbol{t} - 2\boldsymbol{m}'^{\mathrm{T}}(\boldsymbol{X}^{\mathrm{T}}\boldsymbol{t}+\boldsymbol{L}\boldsymbol{m}) + \boldsymbol{m}'^{\mathrm{T}}(\boldsymbol{X}^{\mathrm{T}}\boldsymbol{X}+\boldsymbol{L})\boldsymbol{m}' + \boldsymbol{m}^{\mathrm{T}}\boldsymbol{L}\boldsymbol{m}$$
$$= \boldsymbol{t}^{\mathrm{T}}\boldsymbol{t} - \boldsymbol{m}'^{\mathrm{T}}\boldsymbol{L}'\boldsymbol{m}' + \boldsymbol{m}^{\mathrm{T}}\boldsymbol{L}\boldsymbol{m}$$

Therefore, Eqs. A26-A28 provide the posterior distribution satisfying following relationship.

$$\mathrm{p}(\boldsymbol{w},\beta|\boldsymbol{t}) \propto \beta^{a'+mp/2-1}\exp\left(-\frac{\beta}{2}\left((\boldsymbol{w}-\boldsymbol{m}')^{\mathrm{T}}\boldsymbol{L}'(\boldsymbol{w}-\boldsymbol{m}')+2b'\right)\right) \quad \text{(A29)}$$

Note that the left hand side in Eq. A29 has same functional form as left hand side in Eq. A24 except the normalization factor. Since the $\mathrm{p}(\boldsymbol{w},\beta|\boldsymbol{t})$ is PDF, it should normalized properly, i.e. the integral over whole domain for $\boldsymbol{w}$ and β should be 1. The normalization factor is thus given as similar way as the prior PDF, namely, the following posterior PDF is given.

$$\mathrm{p}(\boldsymbol{w},\beta|\boldsymbol{t}) = C(\boldsymbol{L}',a',b')\beta^{a'+mp/2-1}\exp\left(-\frac{\beta}{2}\left((\boldsymbol{w}-\boldsymbol{m}')^{\mathrm{T}}\boldsymbol{L}'(\boldsymbol{w}-\boldsymbol{m}')+2b'\right)\right) \quad \text{(A30)}$$

Accordingly, Eq. A26 provides the constant $\mathrm{p}(\boldsymbol{t})$ as follows.

$$\mathrm{p}(\boldsymbol{t}) = \frac{(2\pi)^{-n/2}C(\boldsymbol{L},a,b)}{C(\boldsymbol{L}',a',b')} = (2\pi)^{-n/2}\left(\frac{|\boldsymbol{L}|}{|\boldsymbol{L}'|}\right)^{1/2}\frac{b^{a}}{b'^{a'}}\frac{\Gamma(a')}{\Gamma(a)} \quad \text{(A31)}$$

Thus, in log scale,

$$\ln \mathrm{p}(\boldsymbol{t}) = \frac{1}{2}\ln\frac{|\boldsymbol{L}|}{|\boldsymbol{L}'|} + a\ln b - a'\ln b' + \ln\frac{\Gamma(a')}{\Gamma(a)} - \frac{n}{2}\ln 2\pi \quad \text{(A32)}$$

According to the definition of PDFs, the constant given as Eq. A31 is equivalent to the marginal likelihood as follows.

$$\mathrm{p}(\boldsymbol{t}) = \iint \mathrm{p}(\boldsymbol{t}|\boldsymbol{w},\beta)\mathrm{p}(\boldsymbol{w},\beta)\mathrm{d}\boldsymbol{w}\mathrm{d}\beta \quad \text{(A33)}$$